7-20-2012

Influence of Fluid-Structure Interaction on Wall Shear Stress in a Stented Coronary Artery Model

Sirisha Devi Govindaraju

INFLUENCE OF FLUID-STRUCTURE INTERACTION ON WALL SHEAR STRESS IN A STENTED CORONARY ARTERY MODEL

by

Sirisha Devi Govindaraju

A Dissertation

Submitted in Partial Fulfillment of the

Requirements for the Degree of

Doctor of Philosophy

Major: Engineering

The University of Memphis

August 2012

To

My husband and son

Acknowledgements

First, I thank my advisor, Dr. John Hochstein, who has been an excellent mentor and supervisor through my study at The University of Memphis. His support, encouragement, ideas, and flexibility were crucial to the completion of my research and dissertation. I also express my gratitude towards other members of my committee: Dr. Marchetta, Dr. Mo, Dr. Lewis, Dr. Hagen, and Dr. Jennings. In particular, I thank Dr. Hagen for helping me to understand the mathematics involved in deriving the Womersley boundary conditions; I thank Dr. Lewis for ensuring that I was current with the literature and periodically sending me papers that were related to my research; I thank Dr. Marchetta for suggesting different ideas for meshing that helped in modeling the problem; and I thank Dr. Jennings and Dr. Mo for being a part of my committee and for their useful suggestions.

I thank Dr. Ramirez (Alf) for troubleshooting COMSOL, keeping the license server up and running, and ensuring that I had the computing resources to complete my work. I also acknowledge Mr. Koshland and Mr. Souki of the University High Performance Computing Center, who helped me with using the parallel processing resources. I am grateful to Dr. Roan for helping me analyze model convergence issues, and to Dr. Torii, whose papers helped me understand the boundary conditions.

I thank my husband, Bala, for his support, and my son, Sanjeev, for his understanding and cooperation which were instrumental in the completion of my research. Finally, I thank my parents, for the determination they instilled in me to finish against all odds; my parents-in-law, for their encouragement; and to my family and friends, for their support.

ABSTRACT

Govindaraju, Sirisha Devi. Ph.D. The University of Memphis. August 2012. Influence of Fluid-Structure Interaction on Wall Shear Stress in a Stented Coronary Artery Model. Major Professor: John I. Hochstein

Previous studies indicate that the likelihood of rate of restenosis following installation of a bare metal stent to treat coronary artery disease is related to the magnitude of the wall shear stress in the artery. The current study seeks to understand if including fluid-structure interaction (FSI) in a computational model of a stented coronary artery significantly influences the predicted wall shear stress on exposed patches of the artery. As a secondary result, it also determines influence of FSI on the magnitude of WSS on the surface of the stent. COMSOL Multiphysics was the computational tool selected for this study. It was carried out using rigid (no-FSI) and compliant wall (FSI) models comprising of a straight user-defined coronary artery, blood domain and a realistic stent. The arterial wall and stent were modeled as linear elastic materials while the blood was represented by an incompressible Newtonian fluid. Blood flow was assumed to be laminar and its boundary conditions were derived from published physiological waveforms. A periodic Womersley velocity profile was prescribed as the inflow boundary condition and a periodic pressure was prescribed as the outflow condition. Quasi-stationary analyses were carried out on both the rigid and compliant-wall models at different times. A mesh convergence study led to a mesh-independent model. On comparing the FSI and no-FSI models, it was concluded that the influence of FSI was prominent on the stent surface and in the distal region of the geometric model. Although differences between model predictions of wall shear stress varied throughout the period of the waveform, the ranges of difference depend on the axial location along

the artery: 10-20% in the proximal region, 17-55% in the distal region, 10-35% within the stent openings, and 16-58% on the stent surfaces.

TABLE OF CONTENTS

LIST OF TABLES

LIST OF FIGURES

1. BACKGROUND AND MOTIVATION

The human circulatory system consists of three main components viz., blood, blood vessels and the heart.

1.1 Blood: its properties and assumptions for computational modeling

Blood is a suspension of cells in a liquid known as plasma. Plasma is made up of 90 wt. % water , 7 wt. % plasma protein, 1 wt. % inorganic substances and 1wt. % other organic substances. See Figure (1.1). Suspended in the plasma are erythrocytes or red cells, white cells of various categories (neutrophils, basophils, eosinophil, lymphocyte, monocyte etc.), and platelets [21]. Erythrocytes occupy about 50% of the blood volume and their normal count is about 5 million per mm^3. They are small, disk-shaped, about 7 μm in diameter and 2.8 μm in thickness. White cells occupy less than 0.17% of total cellular volume and they range in number from ~5000 to ~8000 per mm^3. Platelets occupy less than 0.125% of cellular volume and are about 250000 – 300000 in number per cubic mm. Platelets are much smaller than white cells and are about 2.5 μm in diameter [21].

Two of the most important fluid properties used in the computational modeling of blood flow are density and viscosity. The density of blood is 1050 to 1055 kg/m^3 [71]. For shear rates (gradient of velocity vector) > 100 s^{-1}, the viscosity of human blood ranges from 0.003 Pa-s to 0.004 Pa-s at 37°C [67]. Blood viscosity is lower for tubes with diameter less than 1mm [67], [74]. Viscosity values for shear rates < 100 s^{-1} increase tremendously and range anywhere between 0.01 Pa-s to 0.15 Pa-s [21]. At extremely low shear rates, the viscosity values are much larger than 0.15 Pa-s. As the temperature decreases, viscosity increases

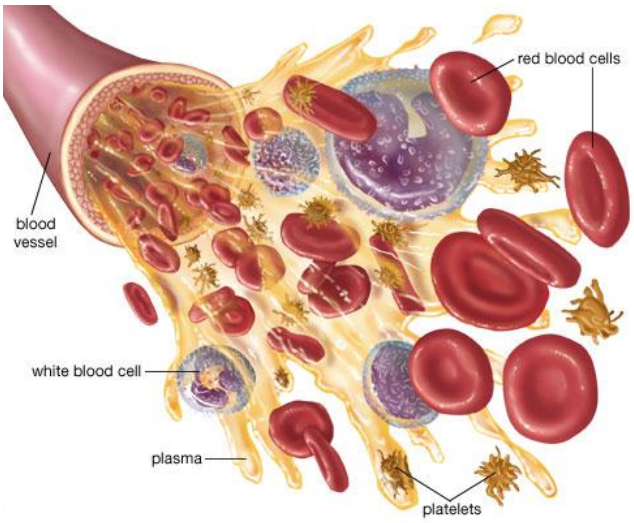

Figure 1.1: Plasma, red blood cells, platelets, and a form of white blood cells that flow in a blood vessel [34]

At high shear rates (>100 sec^{-1}), blood behaves as a Newtonian fluid [21]; that is, shear stress,τ, is directly proportional to the shear rate, $\dot{\gamma}$, with the proportionality constant being the coefficient of viscosity,μ. At shear rates < 100 s^{-1}, blood behaves like a non-Newtonian fluid [21], [67], [74]. Hematocrit, which is the ratio of red cells to the total volume of blood [67], also influences the relationship between shear stress and shear rate. Higher hematocrit levels are associated with higher viscosity and departure from Newtonian behavior.

When the diameter of the blood vessel is large compared to the size of the red blood cells, it is considered a large blood vessel. Coronary arteries are considered large blood vessels. When analyzing blood flow in large blood vessels, blood is considered as a homogeneous fluid [71], [21]. For such analyses, hematocrit and its influence on the Newtonian/non-Newtonian behavior of blood are not relevant. When analyzing capillary blood vessels, which are about the same size as red blood cells, ranging from 4 to 10 μm,

blood can be considered as a non-homogenous fluid and the flow can be considered as the flow of blood in micro-vessels [21].Under physiological conditions, blood may be considered as an incompressible fluid [21]. Also, blood flow is laminar in all blood vessels except the ascending aorta, pulmonary artery, and terminal great veins [43], [67]. Before discovering the unsteady nature of arterial blood flow, the physical law that governs the flow was approximated by considering a simple model of a straight, rigid, and cylindrical pipe with steady, incompressible, laminar flow through it. Such a model is described by Poiseuille's law [67], [71]. The velocity profile describing a Poiseuille flow can be derived as shown below. Let the radius of a pipe described above be R whose x-axis (in cylindrical coordinates) coincides with the axis of the cylinder. If p_1 and p_2 are the pressures at the inlet and outlet of the pipe, l is the length of the pipe, then, the pressure gradient driving the fluid is given by $\frac{p_1 - p_2}{l} = -\frac{dp}{dx}$.

The laws governing the steady, incompressible, laminar flow are given by the continuity and the Navier-Stokes equations as shown below (in cylindrical coordinates):

$$\frac{1}{r}\frac{\partial(rv)}{\partial r} + \frac{1}{r}\frac{\partial w}{\partial \theta} + \frac{\partial u}{\partial x} = 0 \tag{1.1}$$

$$\rho\frac{\partial u}{\partial t} + \rho\left(u\frac{\partial u}{\partial x} + v\frac{\partial u}{\partial r} + \frac{w}{r}\frac{\partial u}{\partial \theta}\right) = \rho f_x - \frac{\partial p}{\partial x} + \mu\left(\frac{\partial^2 u}{\partial x^2} + \frac{\partial^2 u}{\partial r^2} + \frac{1}{r}\frac{\partial u}{\partial r} + \frac{1}{r^2}\frac{\partial^2 u}{\partial \theta^2}\right) \tag{1.2}$$

$$\rho\frac{\partial v}{\partial t}+\rho\left(u\frac{\partial v}{\partial x}+v\frac{\partial v}{\partial r}+\frac{w}{r}\frac{\partial v}{\partial \theta}-\frac{w^2}{r}\right)=$$
$$\rho f_r-\frac{\partial p}{\partial r}+\mu\left(\frac{\partial^2 v}{\partial x^2}+\frac{\partial^2 v}{\partial r^2}+\frac{1}{r}\frac{\partial v}{\partial r}+\frac{1}{r^2}\frac{\partial^2 v}{\partial \theta^2}-\frac{v}{r^2}-\frac{2}{r^2}\frac{\partial w}{\partial \theta}\right) \quad (1.3)$$

In the above equations, u, v, and w are the velocities along the x, r and θ directions, respectively. Also, u, v, and w are functions of x, r, t. f_x and f_r are the body forces (gravitational forces) in the x and r-directions. $\partial p/\partial x$ and $\partial p/\partial r$ are the components of the pressure gradient in the x- and r-directions respectively.

Assuming:

- Steady flow i.e., $\frac{\partial}{\partial t}(\ )=0$
- No external forces are acting on the pipe ($f_x=0$ and $f_r=0$)
- Flow is fully developed (no velocity changes in axial direction, $\frac{\partial u}{\partial x}=0\Rightarrow u(r)$)
- Flow is axisymmetric i.e., $\frac{\partial u}{\partial \theta}=0$
- No swirling of flow $(w=0)$

From the above assumptions, Equation(1.1), which is the continuity equation, reduces to

$$\frac{\partial(rv)}{\partial r}=0 \text{ or } v=0 \quad (1.4)$$

Equation (1.4) and the assumptions reduce Equation (1.3) to

$$-\frac{\partial p}{\partial r}=0 \tag{1.5}$$

This shows that pressure is constant across a section of the pipe. Hence pressure varies only with the x-direction and time.

Using all of the above assumptions, Equation (1.2) results in

$$-\frac{1}{\rho}\frac{\partial p}{\partial x}+\frac{\mu}{\rho}\left(\frac{\partial^2 u}{\partial r^2}+\frac{1}{r}\frac{\partial u}{\partial r}\right)=0 \tag{1.6}$$

$$\frac{\mu}{\rho}\left(\frac{\partial^2 u}{\partial r^2}+\frac{1}{r}\frac{\partial u}{\partial r}\right)=\frac{1}{\rho}\frac{\partial p}{\partial x}=-\frac{p_1-p_2}{\rho l}$$

$$\frac{\partial^2 u}{\partial r^2}+\frac{1}{r}\frac{\partial u}{\partial r}=-\frac{p_1-p_2}{\mu l}$$

$$\frac{1}{r}\frac{\partial}{\partial r}\left(r\frac{\partial u}{\partial r}\right)=-\frac{p_1-p_2}{\mu l}$$

$$\frac{\partial}{\partial r}\left(r\frac{\partial u}{\partial r}\right)=-\frac{p_1-p_2}{\mu l}r$$

Integrating twice with respect to (w.r.t) r gives $u(r)=-\frac{p_1-p_2}{\mu l}\frac{r^2}{4}+c_1\ln r+c_2,$ (1.7)

where c_1 and c_2 are constants of integration evaluated by the boundary conditions

$u(R)=0$ and $u(0)=$ *finite*

As $r\to 0, \ln(r)\to\infty$. Hence if $u(0)=$ *finite* $\Rightarrow c_1=0$

$$u(R) = 0 \Rightarrow c_2 = \frac{p_1 - p_2}{\mu l} \frac{R^2}{4}$$

Hence, Equation (1.7) becomes $u(r) = \frac{p_1 - p_2}{4\mu l} R^2 \left(1 - \left(\frac{r}{R}\right)^2\right)$ (1.8)

However, blood flow in arteries is unsteady [71]. Since Poiseuille's law is only applicable to an incompressible, laminar and steady flow through a straight, rigid, and cylindrical pipe, it should not be applied to the unsteady blood flow. See Chapter 1, Section 1.3 for more details on how to model the unsteady blood flow.

1.2 Blood vessels: types and assumptions for computational modeling of arterial wall

Blood vessels are the conduits through which blood flows. Arteries, arterioles, capillaries, venules, and veins constitute the different types of blood vessels [103]. See Figure (1.2) Arteries are blood vessels that carry blood away from the heart. The aorta is the largest artery in the body and it branches into smaller arteries [116]. The right coronary artery (RCA) and the left coronary artery (LCA) are two of the major blood vessels that branch off from the aorta. They carry blood that supplies oxygen and nutrients to the heart. See Figure (1.3).

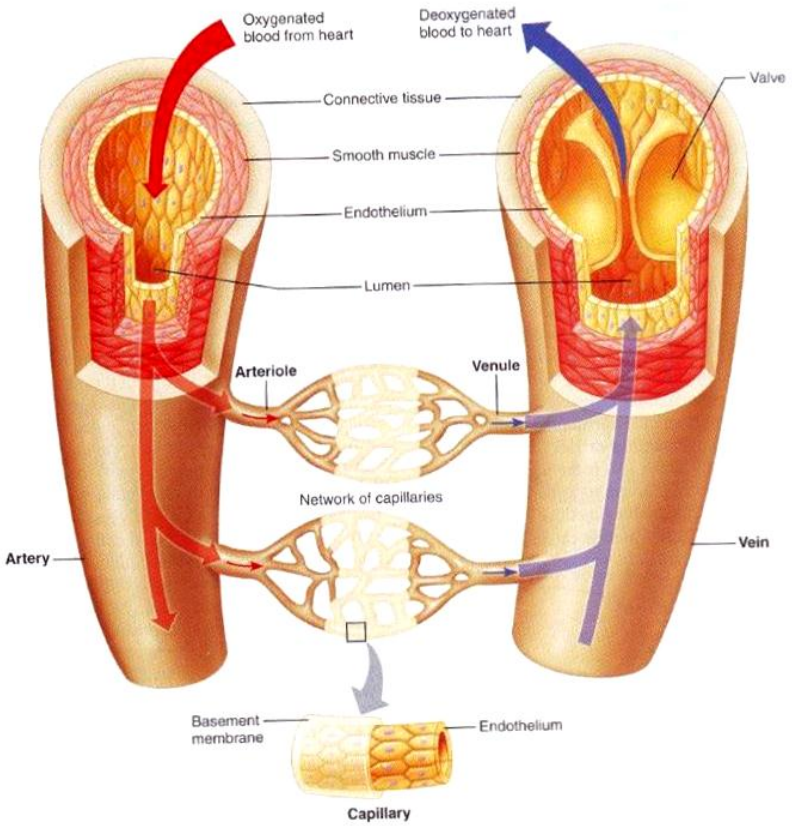

Figure 1.2: Structure of blood vessel [26]

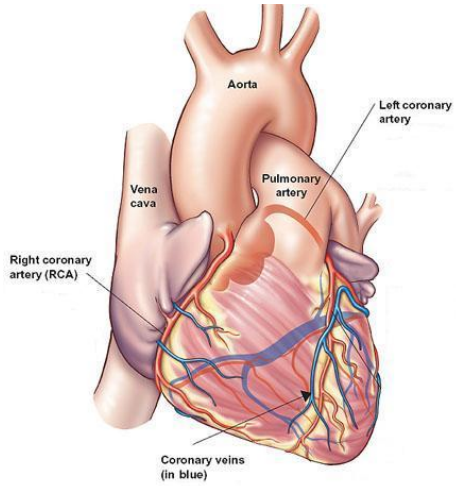

Figure 1.3: Aorta and coronary arteries [35]

The aorta has an internal diameter of about 25 mm and a wall of 2 mm thickness [74]. The smaller arteries coming off of the aorta have internal diameters ranging from 2 mm to 6 mm [26]. In vivo studies on arterial wall thickness show that the arterial wall thickness is about 8% of the luminal diameter [45], [71]. In adults, at its origin, the luminal diameter of the main stem of the LCA and the RCA are in the range of 1.5-5.5 mm, with a mean of 4.0 mm and 3.2 mm, respectively. Before the LCA bifurcates, anatomically it has been found to be about 1 to 26 mm long (average 13.5 mm) but, angiographically, it has been found to be 7.5 mm to 20.5 mm long (average of 12.8 mm).The dominant RCA is about 12-14 cm long [57].

The arterial wall consists of three layers; the intima, the media and the adventitia [74]. See Figure (1.4). The outermost layer is the tunica externa or the tunica adventitia, and is composed of connective tissue. The middle layer is the tunica media, or media and is made up of smooth muscle cells and elastic tissue. Tunica intima or intima is the innermost layer. The interior of this layer is lined up by endothelial cells. This thin layer of endothelial cells that forms an interface between the blood and the intima is known as the endothelium [108].

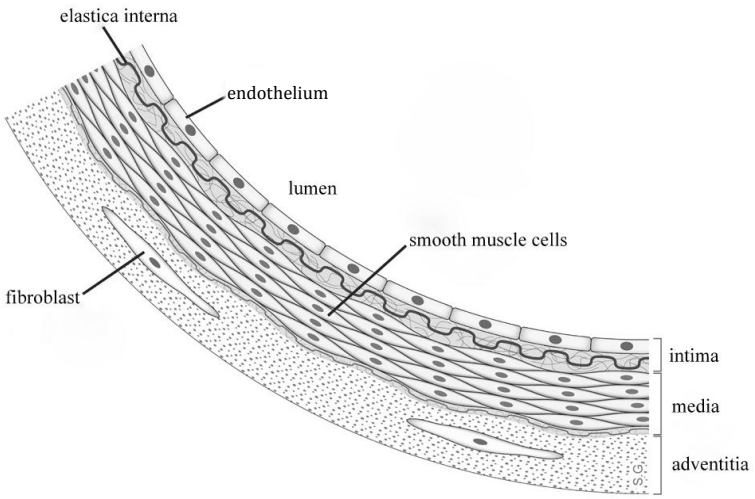

Figure 1.4 Anatomy of the arterial wall [99]

Arterioles are blood vessels that transfer blood from small arteries to the capillaries. Their wall thickness is about 6 μm and the average inner diameter is 30 μm. Arterioles, along with capillaries and venules, make up the microcirculation system of the body. Capillaries, which are the smallest blood vessels in the body, permit the exchange of materials (oxygen, carbon dioxide, sugars, etc) between cells in the tissues and the blood. They range from 5 μm to 10 μm in diameter and are about 10 billion in number. Their walls are about 0.5 μm thick. Venules which are slightly smaller than arterioles, function in the exchange of materials and they transfer blood from capillaries to veins. Their average diameter is about 20 μm and they are about one-sixth as thick as the arterioles [26]

Veins carry deoxygenated blood from the body into the heart. The diameter of veins is about the same as that of arteries but their wall thickness is half that of arteries. Veins are about 0.5 mm thick and their inner diameter is about 5 mm. Venae cavae are the

largest veins, with a diameter bigger than that of the aorta. They are about 30 mm in diameter and are 1.5 mm thick. The anatomy of veins is similar to that of the arteries [26].

A material that resists measurable volume changes when subjected to tensile or compressive load is known as an incompressible material [2]. Under physiological loads, arterial wall resists measureable volume changes [74]. Hence, in computational models, it is treated as an incompressible [7], [23], [53], [74] and homogenized solid (within each layer) [23]. Hooke's law is not a good representation of the stress-strain relationship for an arterial wall [21]. The mechanical properties of arteries depend on the properties of the individual constituents (collagen, elastic, and smooth muscle fibers), their geometric configuration (structure), and interaction [23], [74]. The way the arterial wall constituents are arranged varies along the arterial tree [21]. Arterial wall is anisotropic [38], [40].

The articles published by Kalita and Schaefar [40] and Holzapfel et al. [31] provide a history of arterial wall modeling, and the several constitutive equations used to model the arterial wall. Prendergast et al [79] and Holzapfel et al [32] describe an isotropic hyperelastic material model and a layer-specific, heterogenous arterial material model, respectively. A hyperelastic material model that is suited for representing the anisotropic elastic properties of the advential and intimal layers of the arterial walls is described by Gasser et al. [23]. With the help of the data published by Holzapfel et al [32], Zahedmanesh and Lally [124] define a third-order Ogden hyperelastic material model to represent the artery.

In the geometric models of artery, the applicability of shell models to arteries is discussed in Kalita [41].

1.3 The heart and the cardiac cycle

The heart is a muscular organ that pumps blood through the blood vessels. It is enclosed within a membranous sac called the pericardium and is centrally located in the chest cavity. It is about the size of a fist, with a mass of ~300-350 grams (in males) and 250-300 grams (in females) [26].

The cardiac cycle refers to the sequence of events that occurs between two consecutive heartbeats [104], [1]. In this cycle, the diastole phase is when the heart fills with blood and the systole phase is when the heart pumps out blood. The rhythmic contraction and expansion of the artery at each heartbeat is known as a pulse [16]. Since a pulse is periodic, the pressure gradient, velocity, and flow rate associated with the blood flow are periodic in nature [121]. The blood pressure varies throughout the cardiac cycle and is pulsatile in most arteries [48]. Hence, blood flow is unsteady, periodic, and pulsatile. It can be seen from Figure (1.5) that the pressure and velocity waveforms in different human arteries have different pulsatile waveforms. Mills et al [66] states that these waveforms were recorded from a patient with ischaemic heart disease, with the exception of traces from the right renal and the right common iliac artery.

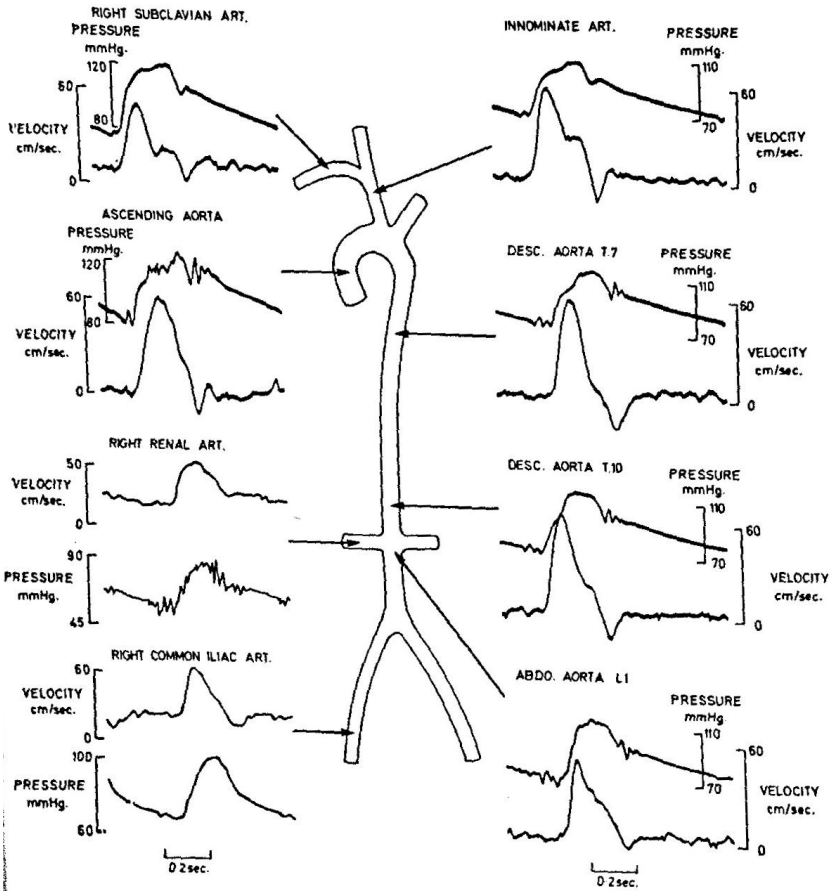

Figure 1.5: Pressure and velocity waveforms in different human arteries [66]

The influence of pulsatile pressure on arterial flow has been described in several studies. The study performed by McDonald [60] in the femoral artery of a dog concludes that the arterial flow oscillates in the same way as the pulsatile pressure but with a phase lag that varies throughout the flow cycle. The physical law governing the unsteady, pulsatile blood flow can be derived by modeling laminar blood flow through a straight, rigid, and cylindrical pipe. Blood is assumed to behave as a Newtonian, viscous and incompressible fluid. The details of this derivation are given in Appendix C. Since this derivation was first described by Womersley [121], the velocity expression obtained is

known as the Womersley velocity profile and is given by (See Appendix C, Equation C.20)

$$u(r,t)=\frac{\psi_0}{4\mu}R^2\left(1-h^2\right)+\sum_{\substack{n=-M\\ n\neq 0}}^{M}\frac{\psi_n(x)}{in\omega\rho}\left(1-\frac{J_0(\lambda_n r)}{J_0(\lambda_n R)}\right)e^{in\omega t}, \tag{1.9}$$

where, $u(r,t)$ is the time-dependent velocity of the flow,

r is the coordinate in the radial direction,

R is the radius of the rigid, straight cylinder,

$$h=r/R \tag{1.10}$$

$$\psi_n(x)=a_{\psi n}(x)-ib_{\psi n}(x) \tag{1.11}$$

The periodic pulsatile pressure gradient across the pipe is represented by a Fourier series and $\psi_n(x)$ is the Fourier coefficient used in this series.

$$\lambda_n^2=\frac{i^3 n\omega}{\nu}=i^3\frac{\alpha_n^2}{R^2}\Leftrightarrow\alpha_n=R\sqrt{\frac{n\omega}{\nu}} \tag{1.12}$$

M=N/2, (See Appendix B)

$$\omega=\frac{2\pi}{T} \tag{1.13}$$

T is the time period of the flow, ω is the angular frequency (pulse frequency) of the flow, and ν is the kinematic viscosity of the fluid.

If the periodic pressure gradient across the pipe is not known, then Equation (1.9) cannot be used. If, however, the velocity waveform at the inlet to the artery is known from in

vivo measurements, then the velocity profile of the flow can be calculated using Equation(1.14). More details on this are given in Appendix C.

$$\Rightarrow u(r,t)=\frac{2q_0}{\pi R^2}\left(1-h^2\right)+\sum_{\substack{n=-M\\ n\neq 0}}^{M}\left[\frac{q_n(r)}{\pi R^2}\frac{\left(1-\frac{J_0(\lambda_n r)}{J_0(\lambda_n R)}\right)}{\left(1-\frac{2J_1(\lambda_n R)}{R\lambda_n J_0(\lambda_n R)}\right)}\right]e^{in\omega t}, \tag{1.14}$$

where $u(r,t)$, r, R, h, λ_n, n, M, T, ω, ν are as defined earlier, and $q_n(r)$ and q_0 are Fourier coefficients of the flow rate expression computed using the in vivo inlet velocity waveform.

The arterial radius, R, and the pulse frequency, ω, are be related to each other by a non-dimensional parameter known as the Womersley parameter, α [27]. From Equation(1.12), when n = 1, α is given by $R\sqrt{\frac{\omega}{\nu}}$.α may be interpreted as the ratio of oscillatory inertial forces to viscous forces [48], [121]. When $\alpha \leq 1$, the frequency of pulse is low and viscous forces dominate, enabling the flow to develop [48], [119]. Hence, velocity profiles are parabolic in shape and the change in flow oscillates almost in phase with the change in pressure. Such a flow can be approximated by Poiseuille's law [125], which is applicable only to steady flows. When $\alpha \geq 10$, the pulse frequency is large. Hence, the inertial forces dominate, leading to a velocity profile that is flat or plug-like. In this case, the mean flow lags the pressure gradient by 90° and Poiseuille's law is not valid [48], [119].

The Womersley velocity profile is derived assuming that the arterial wall is rigid. However, several studies with compliant walls (like those by Torii et al. [91] and Zeng et al. [128]) use the Womersley assumption for their analysis. Womersley also assumes that the pulse wave velocity is negligible. This approximation holds as long as the maximum velocity of the blood is a small fraction of the wave velocity [121].

1.4 Diseases of the heart: atheromatous plaques, atherosclerosis, and stenosis

The most common heart diseases are coronary heart disease, cardiomyopathy, cardiovascular disease, ischaemic heart disease, congestive heart failure, hypertensive heart disease, inflammatory heart disease, and valvular heart disease [112]. Coronary heart disease refers to narrowing of coronary arteries, thus preventing adequate blood supply to the cardiac muscle and tissues [112], [61]. Even though coronary heart disease can occur due to a spasm in the coronary blood vessels leading to its constriction, it is most commonly equated with coronary artery disease (CAD) [55], [112]. CAD also leads to failure of circulation in the coronary arteries. It occurs due to atherosclerosis within the walls of coronary arteries.

An atheroma (plural: atheromata) is an accumulation and swelling in the walls of the arteries. In the context of heart or arteries, atheromata are commonly referred to as atheromatous plaques or, simply plaques [100]. Plaque is made up of cholesterol-rich foam cells covered by a fibrous cap made of connective tissue which is thicker and less cellular than the intima. Plaques can be classified into stable and unstable types [15], [109]. Stable plaques have a firm fibrous cap. They usually progress in size and results in thickening of arteries, leading to a condition known as atherosclerosis. Unstable plaques have a thin fibrous cap with a soft lipid pool underlying the cap and they are prone to

ruptures [118]. When an unstable plaque ruptures, it induces a clotting reaction or thrombus (blood clot) formation [15], [101]. Once formed, the blood clot and the contents of the ruptured plaque will either occlude the arteries immediately or they will eventually flow downstream and occlude the smaller arteries, leading to thromboembolism. Thromboembolism is the event of thrombus formation in the artery and it leads to clogging of the capillaries that are far from the site of thrombus formation [107], [117]. Most commonly, soft plaque ruptures result in an immediate heart attack [15], [101]. The process of plaque development within an individual is called atherogenesis [101]. Over time, the plaque becomes so thick that it blocks the blood flow in the arteries. This abnormal narrowing of a blood vessel is known as stenosis [9], [115].

1.5 Treatment of CAD: coronary angioplasty, stenting and coronary artery bypass grafting

Depending on the severity of the disease, medications and life style changes may be used to treat CAD. In advanced cases, however, other aggressive treatments, such as stand-alone percutaneous coronary intervention (PCI), PCI followed by coronary stent implantation, and coronary artery bypass surgery, become necessary [37].

This kind of interventional cardiology dates back to 1711 when Stephen Hales carried out a cardiac catheterization on a living horse. In 1929, the first documented human cardiac catheterization was performed by Dr. Werner Forssmann. Until the 1950s, catheterization involved an open cut down procedure in which the soft tissues surrounding the artery or vein were dissected followed by a puncture in the artery or the vein (Sones technique). The percutaneous approach was developed by Sven-Ivar Seldinger in 1953. The concept of transluminal angioplasty was described by Charles

Dotter and Melvin Judkins in 1964. Andreas Gruentzig carried out the first successful human percutaneous transluminal coronary angioplasty in 1977 [29], [96].

Percutaneous coronary intervention (PCI) or percutaneous transluminal coronary angioplasty (PCTA) is also known as coronary angioplasty [97]. In a percutaneous approach, the access to the inner organs or other tissues is done via needle-puncture of the skin, rather than by using an "open" cut-down approach of the tissues around the artery. It is called transluminal because the guide wire of the balloon catheter is passed across the lumen of the blood vessel [113]. During a stand-alone PCI, an empty and collapsed balloon on a guide wire known as catheter is passed into the narrowed blood vessel or blocked coronary artery. This process of inserting a catheter is known as catheterization. Once in place, the balloon is inflated to push the plaque outward against the wall of the artery. This opens the blocked or narrowed coronary arteries and restores the flow of blood. Then the balloon is deflated and withdrawn [98].

About 5-10% of cases that undergo PCI report acute vessel closure while 30-50% cases report late lumen narrowing known as in-segment restenosis [95]. In-segment restenosis is the gradual reduction or renarrowing of the lumen circumference. 60-70% of the in-segment restenosis is caused by arterial remodeling and 30-40% is caused by neointimal hyperplasia (NIH) [95]. Remodeling can be defined by changes in the size of the vessel wall, intima [82], while NIH is the formation of a new (neo) or thickened layer of the intima [65]. NIH is also referred as intimal hyperplasia (IH) or neointimal proliferation (NIP).

To prevent in-segment restenosis, a small mesh tube (endovascular scaffolding device) called a stent is placed in the artery to keep it open after the procedure. This

process of inserting a stent in the coronary artery is known as coronary stenting (See Figure 1.6). The stent is crimped over the collapsed balloon and is inserted in the artery using a catheter. The balloon is expanded then deflated and removed. As the balloon expands, the stent expands and stays in the coronary artery even after the balloon is deflated and removed [96]. The stent supports the lumen of the artery and helps it keep open. See Section 1.6 for a brief classification of coronary stents.

Coronary artery bypass grafting (CABG) is an alternative treatment to coronary angioplasty. In this procedure, the arteries with stenoses are bypassed by grafting vessels from elsewhere in the body. Usually, CABG is recommended for patients who have narrowed blood vessels at many locations [105]. Coronary angioplasty is less invasive and costs less than CABG [113]; however, there is a lack of consensus on the issue of difference between the clinical outcomes of stenting and bypass.

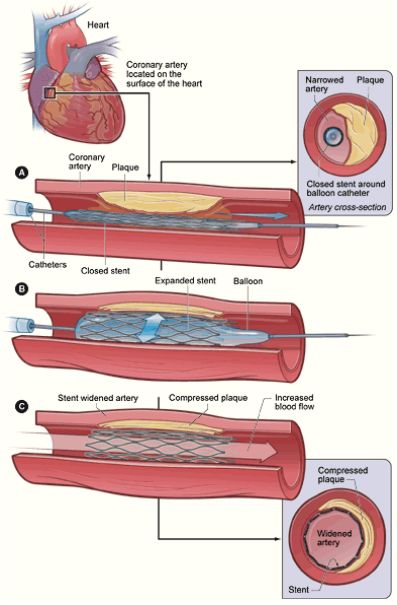

Figure 1.6: Angioplasty and coronary stents [36]

1.6 Classification of coronary stents

In 1986, the first coronary stent was implanted in humans by Jacques Puel and Ulrich Sigwart [29], [84]. Based on the material used for stent fabrication, coronary stents can be broadly classified into two categories,

- Balloon-expandable: They are made from materials that can be plastically deformed by the inflation of a balloon. These are manufactured in their crimped form [68], [85]. The first commercially available stent was a balloon-expandable stent called the Palmaz–Schatz stent [29], [68], [84]. The ideal material used to fabricate a balloon expandable-stent should be easily deformable at balloon pressures, that is, it should have low yield strength and high elastic modulus to reduce the stent recoil. 316L stainless steel is most commonly used for fabricating balloon-expandable stents as it is highly corrosion resistant and possesses all of the above qualities. Some examples of balloon expandable stents are the Johnson and Johnson 'Palmaz-Schatz', the Cordis 'Crossflex', and the Medtronic 'Wiktor'[68], [85]. See Figure (1.7).

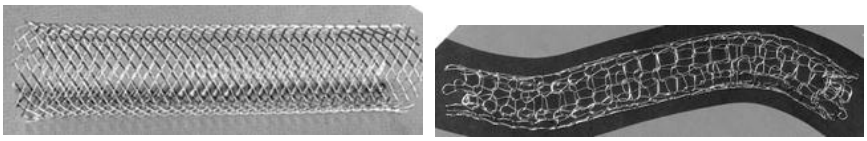

(a)Braided 'wall stent' (b)Knitted 'Strecker stent

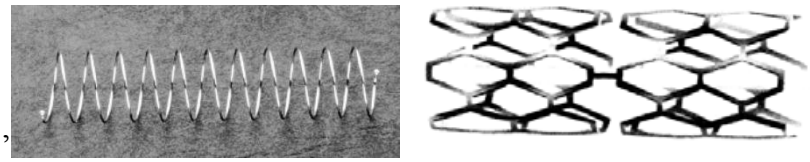

(c)Coiled 'Intracoil stent' (d)Palmaz-Schatz tube stent

Figure: 1.7: Coronary artery stents [54], [75]

- Self-expandable: They are manufactured in their actual size and shape and are compressed by a sheath. Once the stent is in place, the sheath is withdrawn and the stent self-expands to the manufactured diameter [68], [85]. The first stent that was implanted by Puel and Sigwart was a self-expanding wall stent [29], [84]. Materials used for self-expanding stents should withstand large elastic strains. Nitinol, a nickel-titanium alloy, is the most widely used material for self-expanding stents. The Schneider 'Wall stent', Cook 'Z Stent', and the Boston Scientific Corporation (BSC) 'Wall stent' are some examples of self-expanding stents [85]. Self-expanding stents are not very common today because they have a tendency to expand in the weeks after deployment leading to larger growth of neointima. They also substantially shorten upon expanding and their small cell size limits their application in side-branches [68].

Apart from the above classification which is based on the mechanism of deployment, coronary stents can also be classified based on other criteria [85].

- Forms of material used in stent fabrication

  Stents can be made from sheet metal, round or flat wire, or tubing. Some examples of tube stents made from sheet metal are the BSC/Medinol 'NIR', the Navius 'ZR1', and the Cook 'GRII'. The BSC 'Strecker' and the Medtronic AVE S7 stents are examples of wire form of stents. The Palmaz-Schatz stent is a tube stent made from a steel tube [68]. The tube stents made from sheet metal have to be rolled up to a tubular shape after the pattern is created. Then the stent is either welded or locked using special mechanical features.

- Stent manufacturing/fabricating method

  If a stent is fabricated from a "wire-form of material", then wire-forming techniques, such as coiling, braiding or knitting are used to finish the process. All coil stents are self-expanding and are made of Nitinol [85]. Other fabrication methods include laser cutting and photochemical etching.

- Stent geometry

  Based on geometry, the earlier designs of stents were classified as slotted-tube or coil geometry stents. However, Stoeckel et al. [85] classified stent geometry as helical spiral, woven, individual rings, or sequential rings. The stents with sequential ring geometry comprise of a series of expandable z-shaped structural elements, known as struts, joined by connecting elements known as bridges, hinges, connectors, or nodes. Figure (1.8) explains the terms 'strut', 'bridge' and 'inflection point'. The stents can

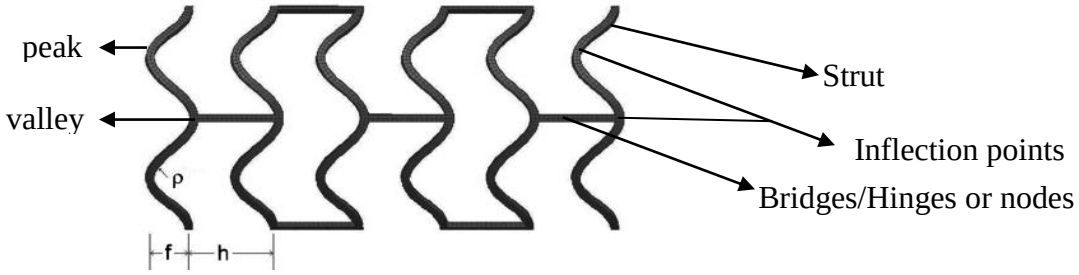

Figure: 1.8: 2D stent geometry showing the struts,bridge connections and inflection points [4]

be made to be more flexible by adding a flex-connector between two consecutive struts. These flex-connectors can be U-, V-, S- or N-shaped. Figure 1.9(a) shows an NIR stent that has a 'V' shaped flex-connector.

Based on the bridge connections, sequential ring stents can be sub-classified into regular connection, periodic connection, and peak-peak or peak-valley connection. Morton et al.[68] refers to sequential stents as modular stents. If all the inflection points of two consecutive struts are connected by bridging elements then, such a design is known as closed-cell design. Figure 1.9(a) shows a closed-cell NIR stent. If some or all the inflection points of two consecutive struts are not connected, then it is an open-cell design. The unconnected struts in an open-cell design add to the longitudinal flexibility of that stent. Figure 1.9 (b) shows an open cell design, where two successive struts are connected by only one peak-peak connection.

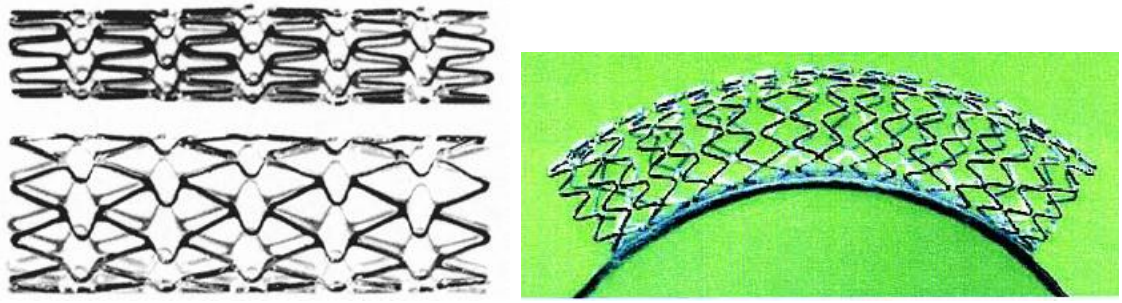

(a) NIR stent (b) AVE S7 stent

Figure 1.9: Closed-cell and open-cell stent designs [85]

- Coatings:

  The first licensed coronary artery stents were bare metal stents (BMS). They have no coating (material or drug) on their surface [102]. Restenosis (renarrowing of arteries in the stented-region) and ST are two major complications that can arise due to implantation of BMSs. See Chapter 1, Section 1.7 for more details. Coated stents

were introduced to overcome these complications [55]. There are several types of coated stents, namely:

- Coated, drug-free BMSs: In these stents, a drug-free coating is deposited on the stent surface either to increase its visibility (in X-rays etc) or biocompatibility [28]. Iridium oxide, gold, platinum, or tantalum are some examples of these coatings [85].
- Drug-eluting stents (DESs): These consist of two components viz., the metal stent and the drug with or without a polymer. Heparin (anticoagulant) or an anti-inflamatory, anti-migratory, and anti-proliferative drug such as paclitaxel, sirolimus, zotarolimus, everolimus, biolimus, dexamethoasone [55].

- Biodegradable stents: Even though DES reduced the rates of restenosis and ST, the risk of late-ST and very late ST, several risks remained when a DES is used, two being myocardial infraction and death [55], [106]. Biodegradable stents were developed to overcome these risks. These stents are absorbed over a period of time and there is no permanent implant, thus preventing the need for a prolonged antiplatelet therapy [63]. These stents, however have several drawbacks, such as the stent not being easy to visualize fluoroscopically, and faster resorption rates that may lead to undesirable remodeling [55]. ‘Absorb’ is the first approved biodegradable stent. As of January 2011, it is available to a few institutions in Europe. By the end of 2012, it is expected to be available throughout Europe [39].

1.7 Motivation for research (hypothesis) and objective of the current study

A 2011 fact sheet from the World Health Organization states that cardiovascular disease is the number one cause of death globally, accounting for 17.3 million deaths, in 2008, with 42% of these deaths being caused by CAD [122].

Among the blood vessels, coronary arteries are the most susceptible to atherosclerosis [17]. The treatment options for a coronary artery disease are listed in Chapter 1, Section 1.5. Since the late 1990s, most coronary angioplasties include placement of a stent in the artery [96]. Chapter 1, Section 1.6 which includes the classification of stents, states that the two major complications that can arise due to the implantation of a BMS are stent thrombosis (ST) and restenosis [55].

ST is the formation of a thrombus (blood clot) on the stent [64]. ST are classified as acute ST, sub-acute ST, late ST and very late ST according to the criteria listed in Table 1.1. One of the factors that seem to be responsible for ST is the inhibition of the growth of a new endothelial layer over the stent surface. ST typically leads to sudden death [106].

It is important to understand the differences between ST and thrombosis. ST occurs after the stent implantation and thrombosis occurs before stent implantation (See Chapter 1, Section 1.4). Thrombosis can also occur immediately after a balloon angioplasty. The balloon expansion inside the narrowed coronary artery can cause vascular wall damage in locations where the balloon contacts the wall. This vascular wall injury can trigger an inflammatory response, resulting in the formation of a thrombus at the site of damage. This will eventually lead to renarrowing of the artery [114].

Table 1.1: Classification and criteria of ST [83]

Classification	Criteria
1. Acute ST	0-24 hours after stent implantation
2. Sub-acute ST	24 hours-30 days after stent implantation
3. Late ST	30 days-1 year after stent implantation
4. Very late ST	≥ 1 y after the stent implantation

Earlier studies show that restenosis develops in 20-35% cases that undergo PCI followed by BMS implantation [95], [114]. In the current study, in-stent restenosis (which is renarrowing of arteries in the stented region) is referred to as restenosis. In-segment restenosis which usually occurs after a PCI procedure (with or without stent implants), is the term used to represent renarrowing in the arterial region (If a stent is present, then this term refers to the renarrowing that occurs on either side of the stent but not in the stented region). See Section 1.5 for in-segment restenosis. Restenosis is largely due to NIH [95]. Intimal thickening (IT) is the thickening of intima due to plaque formation and this is a natural process that is not a consequence of PCI or stent implantation. NIH, however, is due to the rapid proliferation and migration of smooth muscle cells in response to inflammation resulting from the injury to the endothelium due to the stent deployment [44], [55]. Low wall shear stress (< 0.5Pa) is believed to be favorable for plaque accumulation and NIH [50]. Oscillations in the direction of the wall shear stress seem to increase the potential for NIH [47]. Also, at WSS < 0.5 Pa, endothelial cells are circular in shape. This coupled with the blood stagnation regions usually seen in regions with low WSS leads to increased accumulation of particles to the artery wall as a result of increased residence time and increased permeability of the endothelial layer [69].

Below is a summary of the factors that contribute to NIH:

- Proliferation and migration of smooth muscle cells [44], [55]
- Stent strut interactions with the vessel wall [81]
- Post deployment arterial geometry dictated by stent design independent of arterial wall injury [22]
- Low and oscillatory wall shear stress, WSS (oscillations in the direction of WSS) [47], [51].
- Elevated Wall shear stress gradient (WSSG) [51]
- Residual plaque burden after coronary stent implantation [78]

Factors that contribute to restenosis are:

- NIH [95]
- Smaller arteries with reference diameter < 3.0 mm [6]
- Mechanical stretch of the arterial wall (arterial wall injury) during the stent deployment activates the protein kinease Akt pathway which, inturn, plays an important role in cell survival, proliferation, and migration, leading to restenosis [129]
- Gender of patient [55]
- Diabetes and multiple stent implantation [42]
- Stent coating [30]

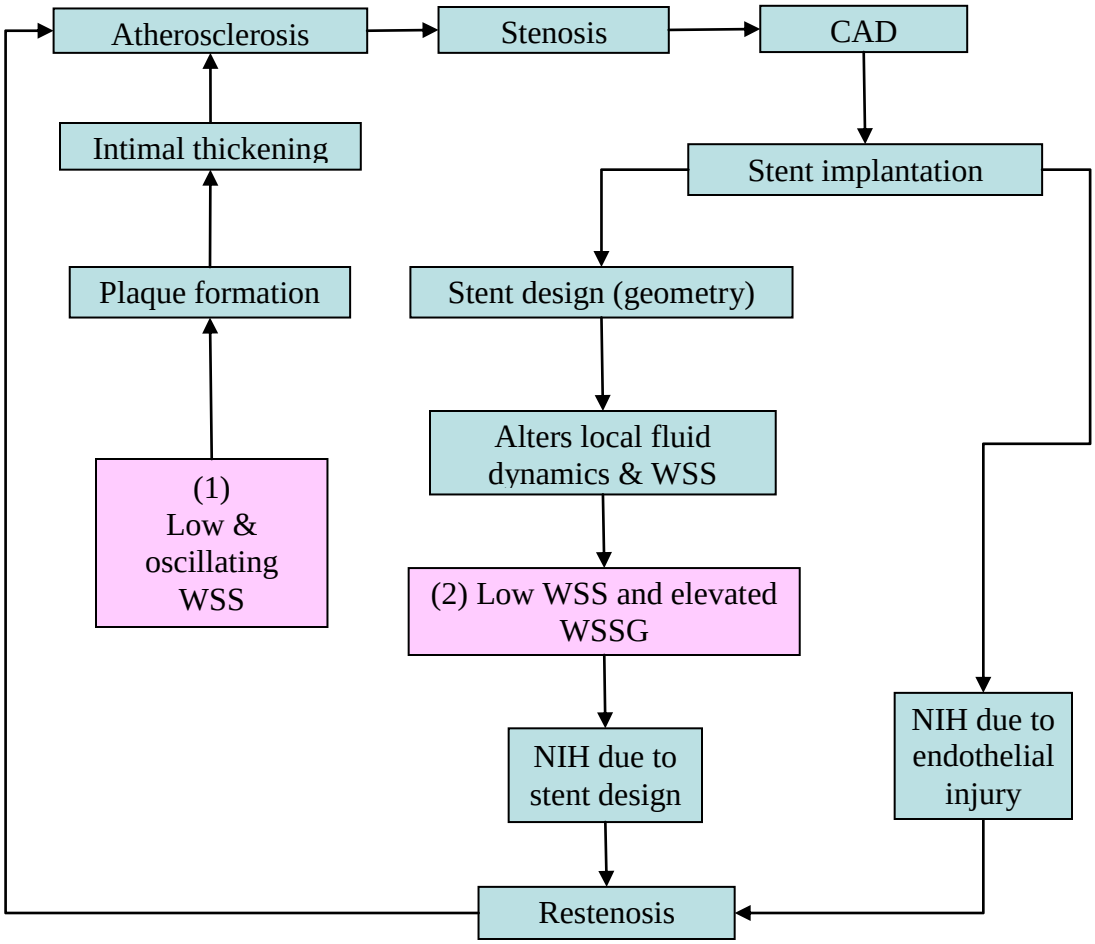

Figure 1.10: Factors leading to stenosis and restenosis.

The starting point for the flow chart shown in Figure (1.10) is: (1) Low and oscillating WSS. This flow chart highlights that low and oscillating WSS is involved in the development of both stenosis and restenosis. Hence, WSS is an important parameter to observe in hemodynamic studies. The literature does not present results from which it can be concluded that fluid-structure interaction (FSI) does, or does not, significantly influence computational predictions of WSS in a stented coronary artery. Including FSI, especially 2-way FSI, produces models that require substantially more computational resources to model this flow. Therefore, the current study seeks to determine the

influence of FSI on computational prediction of WSS in a stented coronary artery. Since BMSs are still an option for patients who cannot tolerate the coated or biodegradable stents [62], a geometric model of a BMS was used.

2. LITERATURE REVIEW ON STENTS

This chapter presents some literature studies on stents. These studies confirm the relation between NIH/restenosis and some of the hemodynamic factors such as low wall shear stress (WSS), high wall shear stress gradient (WSSG), stent geometry/stent structure, coating on stent surface, implantation of multiple stents, and smaller final lumen diameter (after the procedure).

2.1 In vivo and In vitro studies

Most of the in vivo studies compare the performance of different commercially available stent designs and how these designs influence the extent of restenosis. Kastrati et al.[42] carried out a study on patients with coronary stents and concluded that diabetes, multiple stents, and small final minimal lumen diameter are strong predictors of restenosis. To evaluate the influence of stent design and stent coating on restenosis, Hoffmann et al [30] performed angiographic and intravascular ultrasound (IVUS) studies on patients who were implanted with six different stents, namely Multi-Link stents, InFlow stents, InFlow gold coated stents, Palmaz-Schatz stents, NIR steel stents and NIR gold-coated stents. The conclusion of this study agreed with the conclusion of a few other studies that the restenosis is higher with gold-coated stents. Mauri et al.[59] assessed the effects of stent length and lesion length on coronary restenosis using angiographic follow-up studies from patients who were implanted with BMSs. They found that the longer excess stent length (stent length in excess of lesion length), higher the risk of restenosis.

A large number of in vitro studies have been carried out to analyze blood flow and a significant number of these studies evaluated the influence of WSS on intimal thickening (IT) and NIH. There are, however, other hemodynamic parameters such as

WSSG and oscillatory shear index (OSI) that are likely to influence NIH [44], [47], [49], [69]. (See Chapter 2, Section 2.3 for more details about these parameters).

Zarins et al.[127] and Ku et al. [47] carried out studies in models of human carotid bifurcation. Both of them used Laser Doppler Anemometer system to measure their flow velocity and they concluded (independently) that IT occurs in regions of low WSS. Zarins et al also stated that regions with moderate to high shear stress, where flow remains unidirectional and axially aligned, are relatively spared of IT. Ku et al. who found strong correlations between IT and the inverse of maximum wall shear stress, inverse of mean wall shear stress and oscillatory shear index (OSI), also reported that marked oscillations (evaluated by OSI) in the direction of wall shear may increase plaque formation. The experiments performed by Rogers et al [81] on the iliac artery of rabbits using four different stent designs concluded that the interactions of the stent struts with the vessel wall influences the NIH to a greater extent as compared to the arterial enlargement or stent surface material. Computer-assisted digital planimetry was used to determine the cross-sectional area of neointima.

In vitro studies are usually complemented with computational or numerical analysis. In some of these in vitro studies, the experimental studies were used for validating the numerical/computational analysis but, in most of them, a part of the analysis was carried out by the experiments (such as extraction of data for geometry to be used in the computational analysis and physiological waveform extraction) and the rest was completed using Computational Fluid Dynamics (CFD). See Chapter 2, Section 2.1.1 and 2.2 for some of these studies.

2.1.1 Combined numerical and in vitro studies in stented arteries

Mates et al [58] carried out experimental studies on a dynamic model of the coronary circulation which simulated both time-varying supply pressure and peripheral resistance. A mathematical model was developed based on the results from the experimental study. The experimental studies were carried out with and without stenotic lesions. In the case where the stenotic lesion was present, it was assumed to be isolated. Mates et al. concluded that at normal heart rates, the flow is quasi-steady i.e., the dynamic effects are minimal. Their experimental model, however, did not include elasticity of the arteries. They also speculated that at higher heart rates, the dynamic effects may become important.

2.2 Computational studies in stented arteries

Experimental analysis of arteries is difficult especially when dealing with coronary arteries because they are only 2-4 mm in diameter. Fortunately, the advances in computational technology and resources make it possible to create more accurate and realistic computational models of arteries. Also, computational analysis help parameterize the studies i.e., with minimal effort and, time, several studies can be carried out on arteries that vary in size, properties etc. The computational studies of arteries can be broadly classified as one-dimensional (1D), two-dimensional (2D) and three dimensional (3D). Based on the arterial wall model, the 2D and the 3D studies can be further characterized as rigid wall studies or compliant wall studies. Since the current study is carried out using a 3D geometry, only the 3D studies are reviewed here.

2.2.1 Rigid wall studies

Perktold et al. [76] simulated the 3D pulsatile flow field in a model of the left anterior descending (LAD) coronary artery bifurcation. They assumed that the arterial walls are rigid. Since their experimental values were in good agreement with the computational study. The results confirm the presence of flow separation and strong secondary motion in LAD. They also stated that the WSS is influenced by the vessel curvature. Taylor et al. [89], described a finite element framework for analyzing blood flow in arteries. They carried out rigid-wall analysis on the carotid artery bifurcation and the abdominal aorta.

Myers et al [70], carried out steady and unsteady flow analysis in a model of 3D human RCA. They concluded that it is important to replicate patient-specific geometry and the influence of inlet velocity waveform is limited to the inlet region when computing the time-averaged WSS. They also stated that branch flows are not very important in predicting WSS in the main branch of RCA. Carlier et al [8] performed experiments in the iliac arteries of rabbits. The objective of their study was to determine the relationship between WSS and NIH formation in stents by increasing the WSS locally with a flow divider. The study used a combination of angiographic and 3D computational analyses. The results showed that placing a flow divider in the stent locally increases the magnitude of WSS, leading to a reduction in restenosis.

LaDisa et al. [52] carried out 3D computational studies in a stented model of the canine left anterior descending coronary artery. Arterial geometry was based on in vivo measurements. Stent geometry was similar to the Palmaz Schatz stent. Meshes were generated using a custom-generated algorithm in MATLAB and the computational analysis was carried out using CFD-ACE (finite volume representation). Even though

realistic blood flow waveforms were recorded, steady flow boundary conditions were imposed using the maximum and minimum velocity of the realistic flow waveforms. LaDisa et al. concluded that the presence of a stent alters the near wall-velocity and the magnitude of the minimum WSS (up to 77%) as compared to an unstented vessel. They also found that the lower WSS regions were more pronounced at the outlet. Another rigid wall 3D computational study by LaDisa et al [49] related the stent design and deployment ratio to the magnitude of WSS associated with NIH. In yet another rigid wall study, LaDisa et al. [51] found that NIH was localized to regions of low WSS and acute elevations in the spatial WSS gradients(WSSGs). These analyses were carried out in a 3D model of a stented- iliac artery (of rabbits). MATLAB and CFD-ACE were used to perform the CFD analysis. LaDisa et al have carried out several rigid, steady and time-dependent, 3D computational studies on arteries beyond those cited herein.

Balossino et al.[3] examined the influence of stent design on local hemodynamics in stented coronary arteries. Their 3D computational model included artery, blood, plaque, and four different models of stents. Once the deformed configurations of the artery, plaque, and stent were obtained, the fluid walls were assumed to be rigid. ANSYS and FLUENT were used to perform this analysis. Physiological time-dependent waveforms were adopted from the literature reports. This study confirmed the link between stent geometry and hemodynamic factors that influence restenosis. Dehlaghi et al. [14] investigated the WSS in a stented coronary artery using 3D CFD. Their studies, employing a rigid wall model, concluded that the strut spacing, strut profile and number of struts influence the WSS. Duraiswamy et al. [18] compared near-wall hemodynamic parameters for four stented artery models. Simulations were carried out in a flat (but 3D)

rectangular stented vessel with rigid wall assumptions and pulsatile flow conditions. Four different stent designs were compared. WSS, WSSG, and flow separation parameters were reported. Among the four stents, Bx Velocity and NIR stents were concluded to be hemodynamically favorable.

Zarandi et al [126] evaluated the non-Newtonian hemodynamics and shear stress distribution in a 3D model of a healthy and a stented coronary artery bifurcation using COMSOL. They concluded that the stent produces local flow disturbances and regions of low and non-uniform shear stress. Hsiao et al. [33] carried out parametric stent models in a search for the design parameter(s) that most strongly influence the hemodynamic behavior. The parametric designs were built by varying the stent dimensions from -30% to +30% of the original stent dimension. ABAQUS was used for the stent model and its analysis while FLUENT was used to analyze the steady, non-Newtonian, laminar, incompressible blood flow. The arterial wall was assumed to be fixed. In this model, the stent interactions with the angioplastic balloon and the arterial wall were not considered.

Vavourakis et al. [93], and Taylor et al. [89] state that the rigid wall assumption is reasonable in large arteries because there is only a 5-10% change in the arterial vessel diameter during the cardiac cycle and this change in diameter further decreases in a diseased artery. However, the literature studies listed in Chapter 2, Sections 2.2.2 and 2.2.3 indicate that it is important to consider fluid-structure interactions when modeling blood flows in arteries. A large number of the compliant wall studies were carried out in 3D, with either a user-created geometric model or a patient-specific model that is recreated using CT/MRI images of the patient.

2.2.2 Compliant artery studies with FSI and its influence on WSS

Full fluid-structure interaction (FSI) is the process in which the presence of a flow elicits a response from a solid in contact with the fluid, which in turn influences the flow. [110]. Flow-induced vibration of structures is a well-known example of this interaction. The need to include FSI in a computational model for some cardiovascular problems is obvious because it is intrinsic in the behavior of the physiology under investigation (e.g., aortic aneurysms, heart valves) [91]. There are a few FSI studies that deal with blood flow in arteries [77], [90], [128], [91].

Perktold and Rappitsch [77] conducted a 3D, time-dependent analysis of a carotid artery bifurcation. They used published physiological waveforms as boundary conditions An incompressible non-Newtonian flow model was combined with a thin shell arterial wall model to simulate the flow of interest. The model accounts for the interaction between blood and artery; however, the load on the interface only included the pressure force. The forces exerted by the viscous stresses were ignored. The finite element code, ABAQUS, was used for the wall model. It was concluded that including the compliant wall decreased the WSS by 25% as compared to the rigid wall model.

Torii et al [90] developed a simulation tool that modeled cardiovascular FSIs. With this tool, they analyzed a patient-specific model (of the internal carotid artery) subjected to pulsatile flow boundary conditions obtained from in vivo measurements. The arterial domain was fixed at the upstream and downstream ends of the computational domain and represented by an elastic model. They concluded that the distribution of WSS on the compliant arterial walls is significantly different from that on the rigid arterial walls.

Zeng et al [128] created a computational model of a branchless RCA, the geometry of which was derived from imaging techniques. Physiological flow boundary conditions were used. They concluded that arterial wall compliance influences the WSS in the distal region of RCA and the proximal region is unaffected. They also indicate that their results have to be evaluated in conjunction with the outflow to the myocardium through the branches of RCA. Imaging techniques were used to derive the arterial geometry and deformation while an inhouse finite element code was used for the flow analysis.

Torri et al. [91] compared FSI and rigid-wall models of a human RCA and concluded that even though the difference in the maximum time averaged wall shear stress (TAWSS) and oscillatory shear stress (OSI) were insignificant(4.5% and 2.7% respectively) in both the models, the differences in instantaneous WSS profiles were noticeable especially in the distal region of the artery. Their model, which consisted of an arterial wall with 62% stenosis, was reconstructed using patient-specific CT images. The boundary conditions to the flow field were based on in vivo measurements. A time-dependent velocity was specified as the inlet boundary condition and a time dependent pressure was specified at the outflow boundary. A 9-parameter Mooney-Rivlin hyperelastic material model was used to represent the arterial wall but it is unclear what material model was used to represent the stenosis.

2.2.3 Compliant artery studies with FSI (but not related to WSS)

There also a number of computational FSI studies that evaluate variables other than WSS; for example, conditions for wall collapse and plaque rupture.

Tang et al. studied 3D, stenosed, thin-walled [88] and thick-walled [86] arterial models with FSI for blood flow in carotid arteries. Steady flow was assumed and the boundary conditions used are not patient-specific. The ADINA finite element package was used for these studies. Both of these models were directed towards quantifying possible wall collapse conditions and flow characteristics which may be related to artery collapse. Tang et al [87] analyzed steady flow and wall compression in stenotic arteries using a 3D thick wall model with FSI and concluded that severe stenosis causes conditions that may be related to artery compression, plaque rupture, platelet activation and thrombus formation. Gay et al. [24] modeled the interactions between blood flow and a stent using the immersed finite element method. Their 3D model does not include arterial wall interactions with the blood flow. It does, however include 3D modeling of the stent-balloon expansion system. Using this model, they studied the flow patterns during the stent deployment, and its deformation and stress deformation.

Li et al [56] conducted FSI studies in stenosed arteries. Li et al developed a model that includes FSI, a turbulence model, and realistic boundary conditions. They used a combination of 2D and 3D analysis. The flow modeling was done in 3D using FLUENT, the solid model was represented by a 2D geometry and was analyzed using ABAQUS. MATLAB was used to couple the results from the models. The arterial wall was modeled as a linear elastic material. The study, however, focused on factors contributing to plaque rupture. Wu et al [123] whose 3D computational models included the artery, stent, balloon and plaque, simulated the interactions between stent and arterial wall in curved and straight arterial vessels. Final lumen area, tissue prolapse (between stent struts) and stress distribution were compared between the straight and curved wall models.

2.3 Hemodynamic parameters that influence the occurrence of NIH and restenosis

The following WSS-based hemodynamic parameters play a role in NIH/restenosis [44], [69]:

- Wall shear stress (WSS)

  Shear stress is a tensor within the flow field and it is given by

$$\tau = \mu \begin{bmatrix} 2\frac{\partial u}{\partial x} & \frac{\partial v}{\partial x}+\frac{\partial u}{\partial y} & \frac{\partial w}{\partial x}+\frac{\partial u}{\partial z} \\ \frac{\partial u}{\partial y}+\frac{\partial v}{\partial x} & 2\frac{\partial v}{\partial y} & \frac{\partial w}{\partial y}+\frac{\partial v}{\partial z} \\ \frac{\partial u}{\partial z}+\frac{\partial w}{\partial x} & \frac{\partial v}{\partial z}+\frac{\partial w}{\partial y} & 2\frac{\partial w}{\partial z} \end{bmatrix} = \mu\dot{\gamma}, \tag{2.1}$$

  where τ is the shear stress tensor, μ is the dynamic viscosity, and $\dot{\gamma}$ is the shear rate tensor. The magnitude of shear tress tensor is given by Equation (2.2) [52]. The details on how to compute the magnitude of a tensor are in references [94] and [120].

$$|\dot{\gamma}| = \sqrt{\frac{1}{2}\begin{pmatrix} 4\left(\frac{\partial u}{\partial x}\right)^2 + 2\left(\frac{\partial u}{\partial y}+\frac{\partial v}{\partial x}\right)^2 + 2\left(\frac{\partial u}{\partial z}+\frac{\partial w}{\partial x}\right)^2 + \\ +4\left(\frac{\partial v}{\partial y}\right)^2 + 2\left(\frac{\partial v}{\partial z}+\frac{\partial w}{\partial y}\right)^2 + 4\left(\frac{\partial w}{\partial z}\right)^2 \end{pmatrix}} \tag{2.2}$$

  WSS is given by

$$WSS = |\tau| = \mu|\dot{\gamma}| \tag{2.3}$$

- Time-averaged wall shear stress (TAWSS)

  On a surface or an edge, the shear stress tensor reduces to a vector given by

$$\vec{\tau}_w = (\tau_x)\hat{i} + (\tau_y)\hat{j} + (\tau_z)\hat{k} \tag{2.4}$$

  where each component of the vector is the sum of the elements of a row of the stress tensor (τ_x the first row, τ_y the second and τ_z the third) .The stress tensor is given by Equation (2.1). TAWSS is given by:

$$TAWSS = \overline{|\vec{\tau}|} = \frac{1}{T}\int_0^T |\vec{\tau}_w| dt = \frac{1}{T}\int_0^T \left(\sqrt{(\tau_x)^2 + (\tau_y)^2 + (\tau_z)^2} \right) dt, \tag{2.5}$$

- Wall shear stress gradient (WSSG)

  Endothelial cells align themselves with the mean flow direction which corresponds to the local direction of the TAWSS. The resultant WSSG tensor in the local coordinates is given by

$$\nabla \vec{\tau} = \begin{bmatrix} \frac{\partial \tau_m}{\partial m} & \frac{\partial \tau_m}{\partial n} & \frac{\partial \tau_m}{\partial l} \\ \frac{\partial \tau_n}{\partial m} & \frac{\partial \tau_n}{\partial n} & \frac{\partial \tau_n}{\partial l} \\ \frac{\partial \tau_l}{\partial m} & \frac{\partial \tau_l}{\partial n} & \frac{\partial \tau_l}{\partial l} \end{bmatrix}, \tag{2.6}$$

  where ‘m’ is the temporal mean WSS direction, ‘n’ is tangential to the surface and normal to ‘m’, and ‘l’ is the surface normal direction. The components of ‘l’ are not

of importance to the endothelial cells because it is the tangential forces that influence them.

Hence, when it comes to evaluating endothelial cell function, Equation (2.6) is reduced to

$$\nabla \vec{\tau} = \begin{bmatrix} \frac{\partial \tau_m}{\partial m} & \frac{\partial \tau_m}{\partial n} \\ \frac{\partial \tau_n}{\partial m} & \frac{\partial \tau_n}{\partial n} \end{bmatrix} \tag{2.7}$$

$\frac{\partial \tau_m}{\partial m}$ and $\frac{\partial \tau_n}{\partial n}$ generate intracellular tension and have been determined to be the dominant influence on IT or NIH [44]. Therefore, the literature generally presents values for WSSG computed from:

$$WSSG = \sqrt{\left(\frac{\partial \tau_m}{\partial m}\right)^2 + \left(\frac{\partial \tau_n}{\partial n}\right)^2}, \tag{2.8}$$

where τ_m is the shear stress in the m-direction and τ_n is the shear stress in the n-direction.

- Oscillatory shear index (OSI)

  "Cyclic departure of the wall shear stress vector from its predominant axial alignment indicates flow disruption over time and is known as the oscillatory shear index (OSI) [44]. OSI represents a measure of the shear stress acting on the luminal surface due to either "crossflow" or reversing flow velocity components occurring during pulsatile flow" [47].

OSI is given by

$$OSI = \frac{1}{2}\left(1 - \frac{\left|\int_0^T \vec{\tau}\, dt\right|}{\int_0^T \left|\vec{\tau}\right| dt}\right), \tag{2.9}$$

where τ is the shear stress vector and T is the time period.

Niemann et al [72] define OSI as

$$OSI = \frac{1}{2}\left(1 - \frac{\sqrt{\left(\int_0^T \tau_x dt\right)^2 + \left(\int_0^T \tau_y dt\right)^2 + \left(\int_0^T \tau_z dt\right)^2}}{\int_0^T \sqrt{\left(\tau_x\right)^2 + \left(\tau_y\right)^2 + \left(\tau_z\right)^2}}\right), \tag{2.10}$$

where $\tau_{x,}$ $\tau_{y,}$ and τ_z are the magnitudes of shear stress in the x, y, and z directions.

OSI ranges between 0 and 0.5. Zero OSI signifies a total unidirectional WSS and OSI of 0.5 describes a purely unsteady and oscillatory flow [73].

The objective of the current study is to determine the influence of FSI on the magnitude of WSS. Note, however, that since each of the other aforementioned parameters is related to WSS and literature studies confirm their relation to restenosis and NIH, some of these parameters were evaluated in the current study. See Chapter 4 for the results.

2.4 Numerical methods used in the FSI studies of stents

The FSI models used in studies of coronary arteries can be either one-way or two-way coupled. When a FSI study is one-way coupled it means that either the fluid flow influences the solid, or the solid displacement influences the fluid flow, but not both. In a two-way coupling, each domain influences the other. To the best of my knowledge, the following FSI studies are yet to be conducted:

- A FSI study with two-way coupling that includes plaque, artery, blood, cardiac muscle, and stent in the analysis
- A FSI study with two-way coupling that includes coronary artery, blood, and stent (like the current study).

The two approaches to solve a one-way or two-way coupled FSI problem are [93]:

- Solving the equations describing the fluid motion and the solid wall motion separately in a segregated manner, using two different solvers, and then using the results from one domain as updated boundary conditions for the other domain. This is known as the partitioned approach [110]
- Solving the equations describing the fluid motion and the solid wall motion simultaneously in a fully-coupled model. This is also known as the monolithic approach [110]

The Arbitrary-Lagrangian-Eulerian (ALE) algorithm is the most widely used numerical method for the fully coupled FSI approach. This method is computationally very intensive. Other methods used to solve FSI problems include the immersed boundary method, transpiration techniques based on linearization principles, and the coupled-momentum method [93]. The current study is conducted using COMSOL

Multiphysics software which uses ALE formulation. Hence some details about ALE formulation are given in the next section.

2.4.1 ALE formulation/algorithm in COMSOL

The physics of a problem determines the partial differential equations (PDEs) that are solved in a finite element model. These equations are formulated either in the material coordinate system or the spatial coordinate system. When a material coordinate system is used, then it is known as the Lagrangian formulation and when a spatial coordinate system is used, it is known as the Eulerian formulation. The ALE method, which is a combination of the Lagrangian and Eulerian formulations, allows moving boundaries i.e., it has a moving mesh [12]. See [10] for more details about COMSOL's ALE formulation.

In the COMSOL ALE formulation, the representation of the solid domain (artery and stent) is in material coordinates and the fluid domain (blood) is represented by the spatial coordinates. These coordinates are related to each other by

$$x = x(X,t) = X + u(X,t), \tag{2.11}$$

where x is the spatial coordinate, X is the material coordinate, and u is the displacement vector in the x-direction pointing from the reference position to the current position. The relationships between y,z and Y,Z are similar to Equation (2.11) (the displacement vector is replaced by v(Y,t) and w(Z,t) for y and z, respectively). Along with the equations for the physics, the mesh deformation on the domains with free deformation (see [10]) is determined by one of three equations and it called "smoothing". For the current study, a hyperelastic smoothing method has been used because it works better for FSI problems [12]. The important thing to note here is that in order for an FSI simulation to run

successfully, COMSOL solves two different kinds of PDEs. One set represents the physics of the model (see Chapter 3, Section 3.5) and the other set of represents the mesh movement. For more details on the equations that determine the mesh movement, see [12].

2.5 An ideal finite element model for realistic blood flow

Based on the literature review and the conclusions of the current study (see Chapter 5), a finite element model that includes all of the following features is likely to represent a more realistic blood flow in diseased, coronary arteries. However, depending on the objective of a study not all of these features may be necessary.

1. Realistic patient-specific arterial geometry and boundary conditions for blood flow
2. Arterial model that considers the incompressibility of arterial wall, tissue anisotropy, residual stresses, heterogeneity and layered structure of artery
3. Non-homogenous plaque represented by a material model
4. Realistic stent geometry
5. Coronary artery movement and the presence of cardiac muscle
6. Stent-balloon assembly model (and interactions between them)
7. Initial stresses present in the arterial wall
8. FSI between blood, artery and stent

3. FINITE ELEMENT MODEL

The objective of the current study was to evaluate the need for modeling fluid structure interactions (FSI) in the computational analyses of stented coronary arteries. Modeling fully-coupled FSI interactions significantly increases the computational resources required to simulate flow of interest as compared to a rigid wall model. It is therefore desirable to determine if the additional complexity and effort produces a significant difference in prediction of parameters of physiological interest.

Due to finite computational resources and the limited availability of realistic data, the current study only includes the following features in the computational model:

1. Realistic boundary conditions for the blood flow
2. Realistic stent (BMS) geometry
3. Linear elastic material model for the arteries
4. Flow was modeled in a healthy coronary artery i.e., no plaque model
5. Straight tube geometry i.e., no patient-specific geometry
6. FSI in blood, artery and stent

3.1 Computational tool: COMSOL Multiphysics

COMSOL Multiphysics was chosen as the computational tool for this study because it is capable of modeling multiple physical phenomena simultaneously. It can simultaneously model physics involving fluid mechanics, solid mechanics, chemical reactions etc. Using COMSOL, it should be possible to extend the current study of a bare metal stent to include simulation of a drug-elution stent. Apart from this, COMSOL is capable of creating reasonably complex geometries and has a built-in meshing tool unlike a few other Computational Fluid Dynamics (CFD) software that need an external mesh

generating software. COMSOL also has a large variety of solvers and off-the-shelf modules like the FSI module. These off-the-shelf modules save time in setting up the model because they comprise of all the equations required to model the physics. For example, the FSI module:

- identifies the fluid-solid interface automatically. This is very helpful with complex geometries.
- has in-built equations
    - for load applied at the fluid-solid interface,
    - that enable the solid to deform based on the force applied by the fluid
    - that deform the fluid mesh to conform with the solid wall displacement

3.2 Geometric model and symmetry

The region of blood flow (blood domain) is represented by a cylinder that is 10mm long and has a cross-sectional area of 6.26 sq.mm (2.82 mm diameter). The artery is modeled as a hollow cylinder with an internal diameter of 2.82 mm and a wall thickness that is 8% of the lumen diameter. The stent model and its dimensions were obtained from a journal paper [25]. In the current model, the stent is 2 mm long and has struts that are 0.008 cm thick. The full geometric model and an enlarged view of the stent model are shown in Figures 3.1 and 3.3. Figure 3.2 shows a view of the geometric model with the stent inside. The cylinder has no features that depend on azimuthal position. The stent geometry is regular, repeating in axial and azimuthal directions. The computational resources required for the simulation have been greatly reduced by reducing the full-cylinder model to an extruded pie-sector model (Figure 3.4) with an included angle of 36 degrees with symmetry conditions imposed on both faces of the pie-slice.

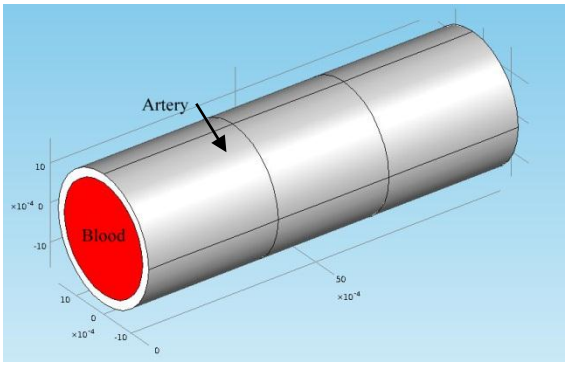

Figure 3.1
Full geometric model

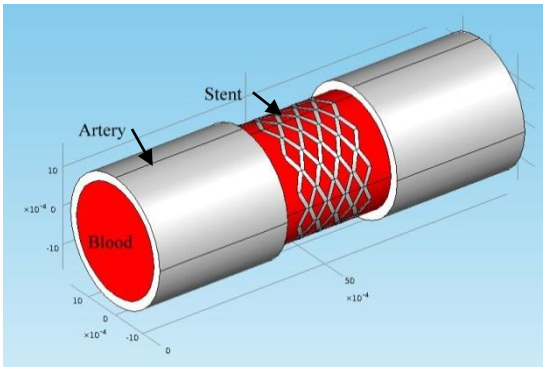

Figure 3.2
View of geometric model with stent

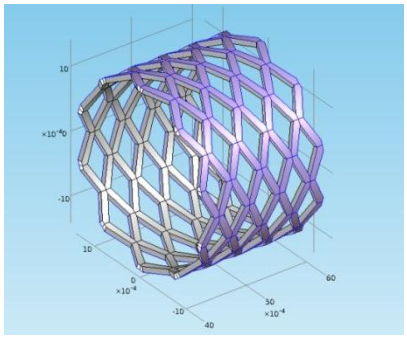

Figure 3.3
Stent model (enlarged view)

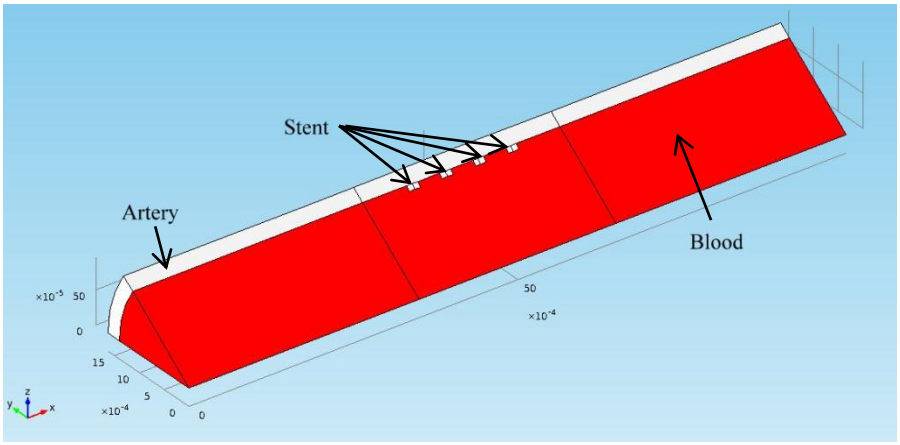

Figure 3.4: Model used in current study

3.3 Material properties

In the current study, blood is modeled as an incompressible, homogenous, and Newtonian fluid with a density (ρ) of 1050 kg/m^3 and a dynamic viscosity (μ) of 0.0035 Pa-s. The arterial wall is represented as a homogenous, incompressible, linear elastic material with an elastic modulus (E) of 10^6 Pa, a Poisson's ratio (υ) of 0.45, and a density (ρ) of 1060 kg/m^3. Chapter 1 provides the references for these numbers. All the studies are carried out using the material properties of a 316L stainless steel stent. Below are the properties used to model the stent material.

Table 3.1: Material properties of stent

	Density [kg/m^3]	Elastic modulus [GPa]	Poisson's ratio
316L stainless steel	8000	200	0.30

The blood flow is assumed to be laminar. Although the velocity and pressure boundary conditions are periodic in time, a quasi-steady model that does not include time-dependent terms in the modeling equations for either the solid or flow domains serves as the basis for the computational simulation. Therefore, instead of reporting data at selected times from a single transient simulation, the data presented is from a sequence of stationary solutions in which each has boundary condition values appropriate for that time. From a physical point-of-view, this neglects the influence of inertia for this simulation.

3.4 Finite element grid (mesh)

One of the basic steps in a finite element analysis is to divide the model into a finite number of elements. This process which is known as discretization reduces the original model to a collection of linear, quadratic, or higher order elements. The order of the elements is selected by the user. See Chapter 2, Section 3.7 for more details.

A mesh convergence study was conducted using five meshes viz., M1, M4, M5, M6 and M8. The mesh resolution increases with increasing mesh number. The meshes consist of wedge and tetrahedral elements.

.

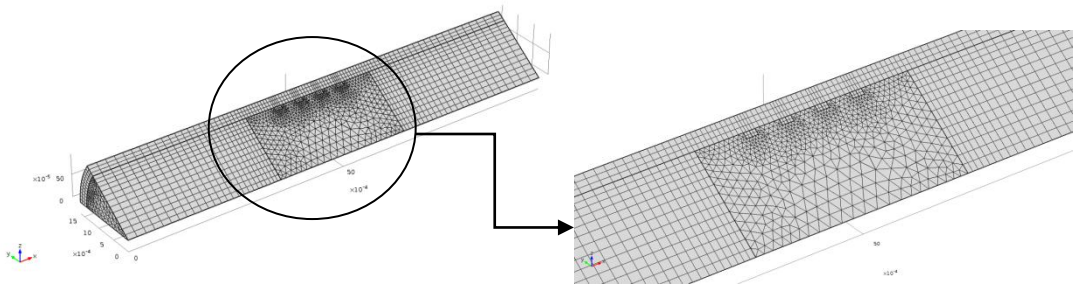

(a) M1

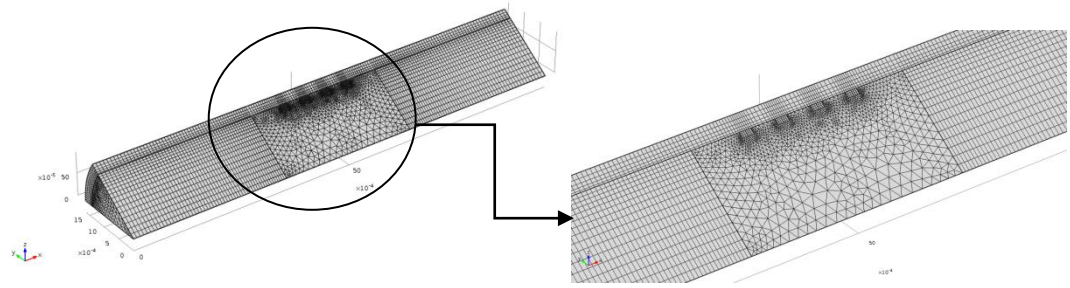

(b) M5

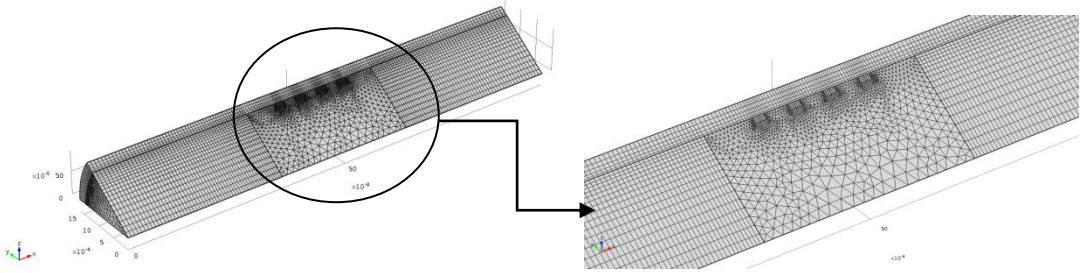

(c) M6

Figure 3.5: Mesh distribution (full view)

Table 3.2: Details of finite element mesh

Meshes	Distribution	No. of elements	DOF
M1	5x2 – 2w	52,203	105,510
M4	5x4 – 2w	113,317	251,971
M5	8x4 – 3w	168,892	357,389
M6	10x4 – 3w	199,048	427,692
M8	14x4 – 4w	298,842	624,826

Table 3.2 gives the number of elements and the degrees of freedom (DOF) in each mesh. Figure (3.5) shows M1, M5 and M6 mesh configurations listed in this table. The mesh configuration of M4 is similar to that of mesh, M5 (See Figure 3.5); however, the number of elements in M5 are more than the number of elements in M4. Similarly M8 and M6 have similar configurations but M8 has more number of elements. The numbers under the column with heading "distribution" indicate the distribution between the struts along a line through the center of the diamond shaped opening formed by the stent struts. For example, in Table 3.2, Column2, Row 5 reads "14x4 – 4w". This means that there are 14 elements (either structured or unstructured) between the tips of the diamond, 4 elements across the strut thickness (radial) and 4 elements along strut width (axial). Figure (3.6) shows the geometric representation of the terms strut thickness (radial) and strut width (axial). Figure (3.7) shows the above discussed element "distribution" (14 elements, 5 elements, 4 elements) for mesh M8.

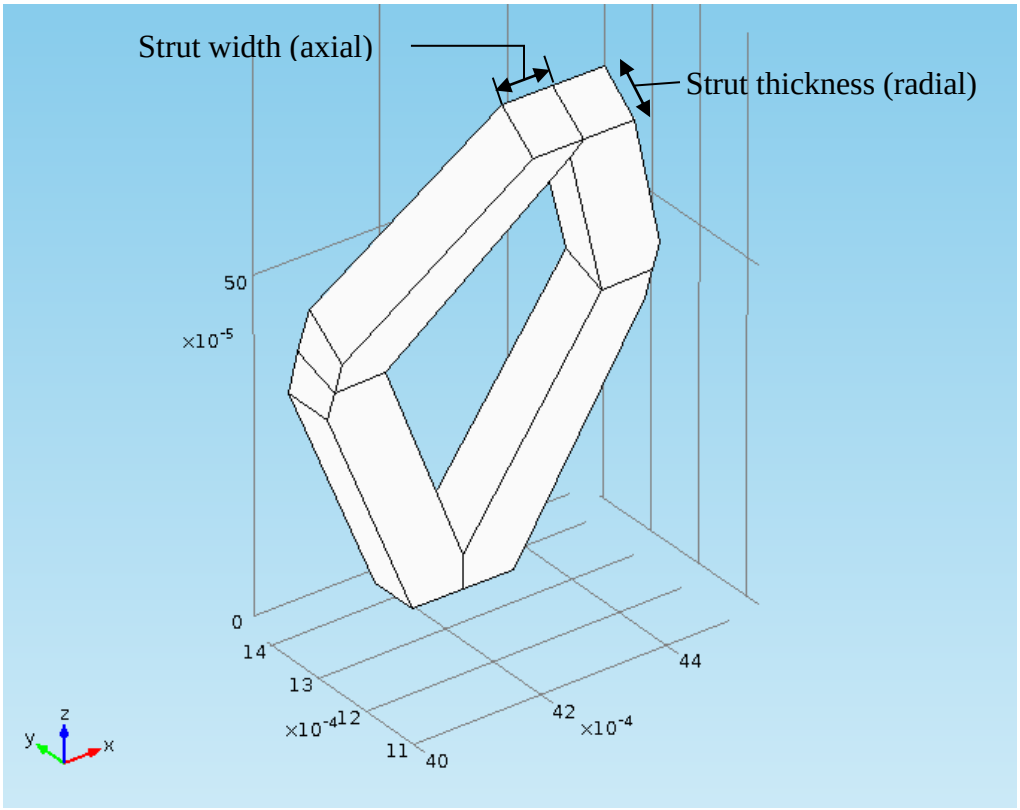

Figure 3.6: Single strut showing the terms strut thickness (radial) and strut width (axial)

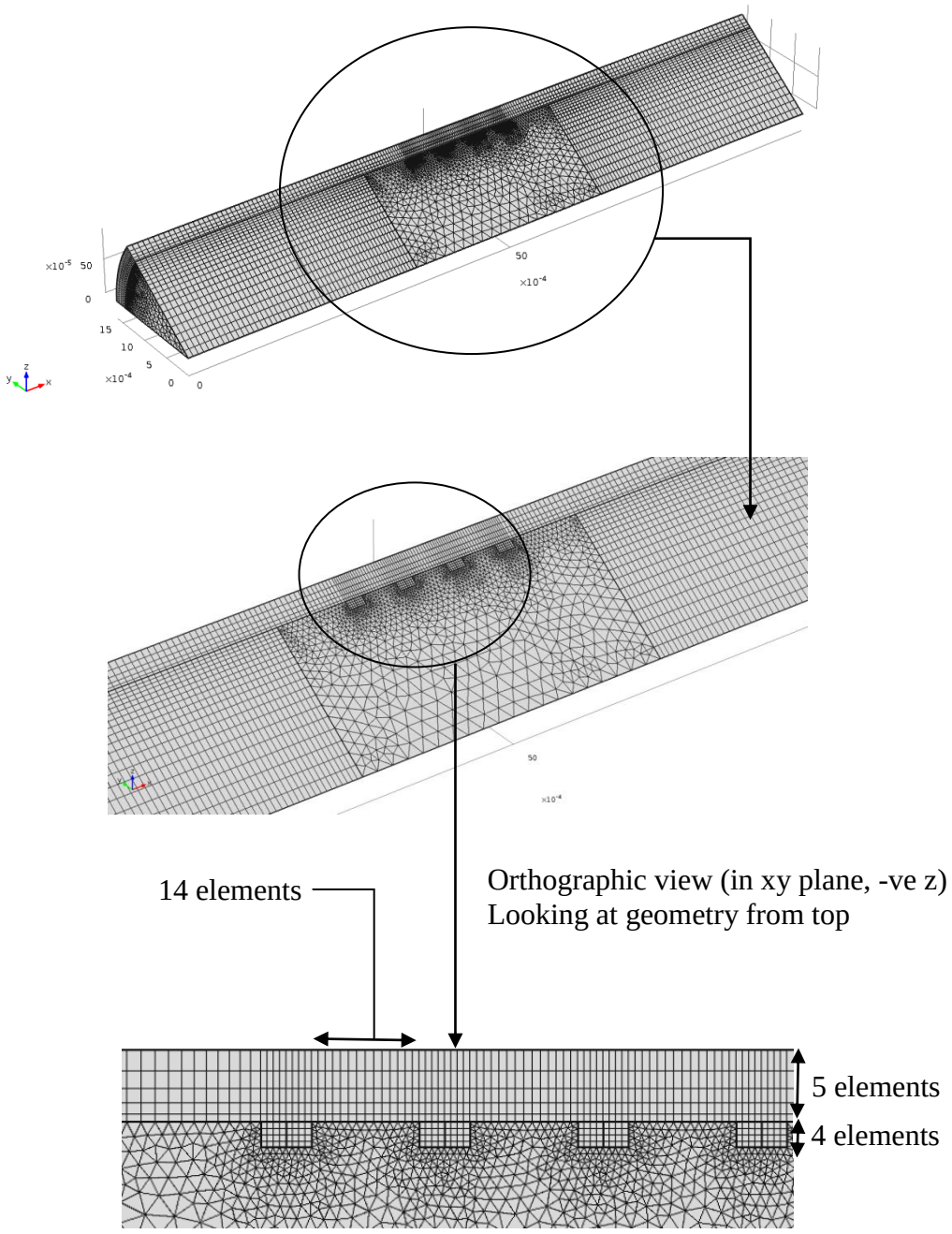

Figure 3.7: Mesh 8

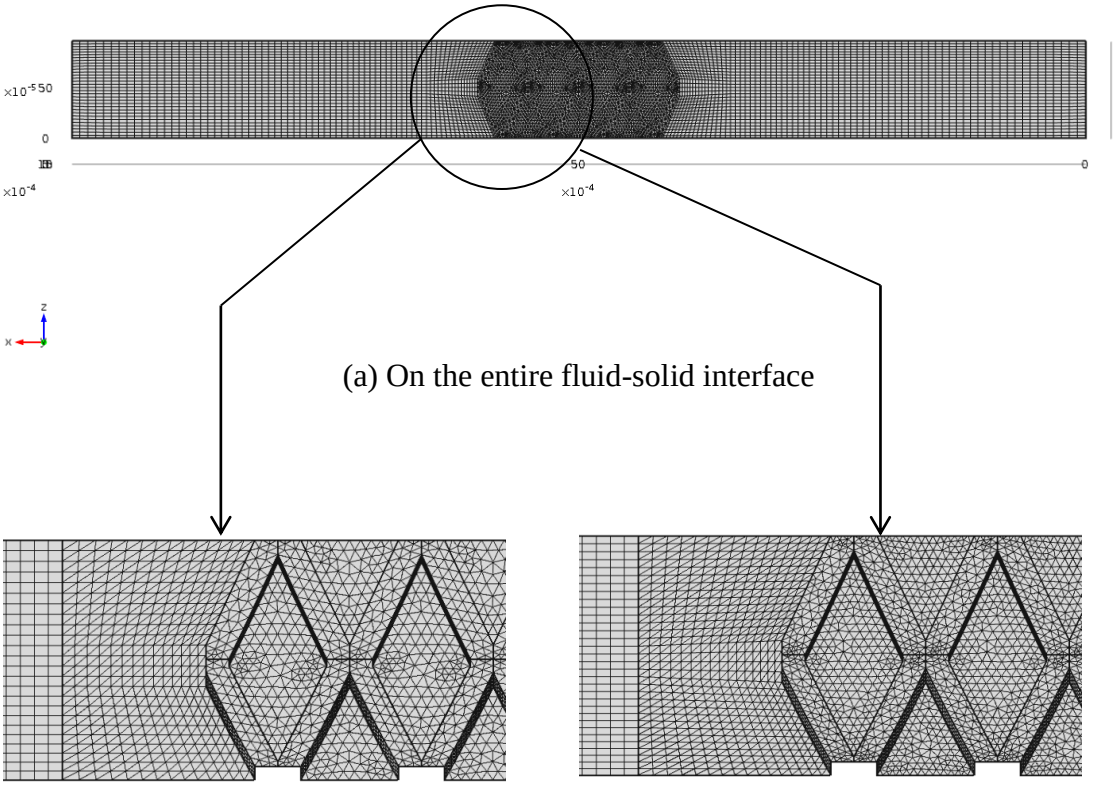

(b) Enlarged view of M6 at the interface (c) Enlarged view of M8 at the interface

Figure (3.8) Mesh configuration on fluid-solid interface

Figure (3.8a) shows the mesh on the fluid-solid interface for mesh, M8. Figures (3.8b) and (3.8c) show an enlarged view of this interface mesh for meshes, M6 and M8 respectively. Even though the current geometry has four struts, Figures (3.8b) and (3.8c) show the interface mesh only for two struts (for clarity). The interface mesh distribution in and around the remaining two struts is similar to what is shown in these figures.

3.5 Partial differential equations (PDE) solved

Since the blood flow is assumed to be steady, incompressible, homogenous and Newtonian, the fluid flow equation that is being solved by COMSOL [12] is given by Equation(3.1).

$$\rho\left(u_{fluid}\cdot\nabla\right)u_{fluid}=\nabla\cdot\left(-pI+2\mu S\right)+F, \tag{3.1}$$

where u_{fluid} is the vector velocity.

I is the 3x3 identity matrix. S is the strain rate tensor and it is given by

$$S=\frac{1}{2}\left(\nabla u_{fluid}+\nabla u_{fluid}{}^{T}\right) \tag{3.2}$$

If u, v, and, w are the velocity in the x, y, and z directions, then S in matrix form is expressed as shown in Equation (3.3)

$$S=\begin{bmatrix} S_{xx} & S_{xy} & S_{xz} \\ S_{yx} & S_{yy} & S_{yz} \\ S_{zx} & S_{zy} & S_{zz} \end{bmatrix}=\frac{1}{2}\begin{bmatrix} 2\frac{\partial u}{\partial x} & \frac{\partial v}{\partial x}+\frac{\partial u}{\partial y} & \frac{\partial w}{\partial x}+\frac{\partial u}{\partial z} \\ \frac{\partial u}{\partial y}+\frac{\partial v}{\partial x} & 2\frac{\partial v}{\partial y} & \frac{\partial w}{\partial y}+\frac{\partial v}{\partial z} \\ \frac{\partial u}{\partial z}+\frac{\partial w}{\partial x} & \frac{\partial v}{\partial z}+\frac{\partial w}{\partial y} & 2\frac{\partial w}{\partial z} \end{bmatrix}=\frac{1}{2}\nabla u_{fluid}=\frac{\tau}{2\mu} \tag{3.3}$$

In Equation (3.3), τ is the shear stress and

$$\nabla \cdot 2\mu S = \nabla \cdot \tau = \nabla \cdot \mu \nabla u_{fluid} = \mu \nabla^2 u_{fluid} \tag{3.4}$$

Using the above expressions, Equation (3.1) reduces to

$$\rho u_{fluid} \cdot \nabla u_{fluid} = -\nabla p + \mu \nabla^2 u_{fluid} + F \tag{3.5}$$

F is the volume force vector and it includes forces like gravity. In FSI models, "F" is the force exerted on the solid boundary by the fluid. The magnitude of this force is the same as the reaction force on the fluid but opposite in direction [13]. This force is already included in COMSOL's off-the-shelf FSI module and should not be considered as a new boundary condition. The reaction force on the fluid (incompressible) due to F is given by f

$$f = n \cdot \{-pI + \tau\}, \tag{3.6}$$

where n is the outward normal on the boundary, P is the pressure, I is the identity matrix, τ is the shear stress. However, since the Navier-Stokes equations are solved in the spatial frame while the solid mechanics interfaces are defined in the material frame, this force needs to be transformed [13]. Hence the final expression of F becomes

$$F = f \cdot \frac{dv}{dV}, \tag{3.7}$$

where dv and dV are the mesh element scale factors for the spatial and material frames respectively. The mesh element scale factor is used for mapping between the local and global coordinates. For more information on the mesh element scale factor, see reference [12]. Also, since FSI involves a moving mesh, the fluid velocity in Equation (3.6) is replaced by the wall velocity,

$$u_{fluid} = u_{wall} = \frac{\partial u_{solid}}{\partial t}, \tag{3.8}$$

where u_{solid} is the displacement of the solid.

Equation (3.1) has two unknowns, which are the blood velocity, u, and the pressure, p. Continuity provides the second equation to be satisfied. For an incompressible, steady flow, it reduces to

$$\rho \nabla \cdot u_{fluid} = 0 \tag{3.9}$$

The pressure and velocity boundary conditions that are used to solve Equation (3.1) are discussed in Chapter 3, Section 3.6. In this equation, the coefficients of the partial differential terms are not constant but they are the dependent variables. Hence, the equation is classified as nonlinear.

The equation that is used to solve the unknowns in the solid domain (artery and stent) is based on the principle of virtual work. It states that the sum of the virtual work from internal strains is equal to work from the external loads [13]. For the current study, the simplified form is given by

$$-\nabla \cdot \sigma = F_v \tag{3.10}$$

Since the normal and shear strain variables depended on the displacement variables, using the above principle the displacements are evaluated.

3.6 Boundary conditions

The boundary conditions used for the blood, stent and artery are shown in Figure (3.9)

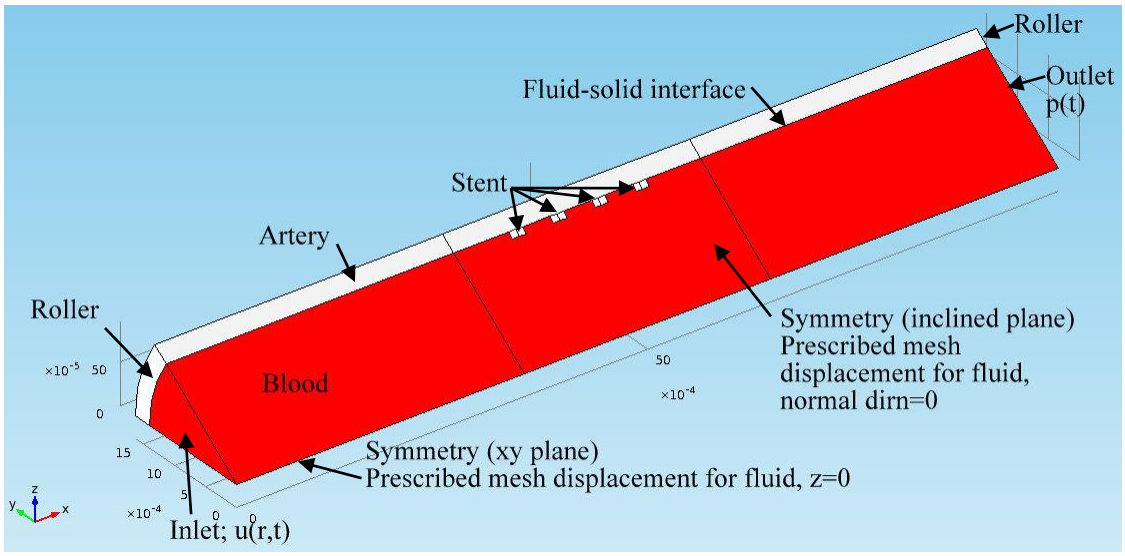

Figure 3.9: Boundary conditions used in the current study (for FSI sub-study)

Physiological velocity and pressure waveforms are used as the inlet and outlet boundary conditions of the blood domain. These waveforms are periodic and were published by Torii et al [91]. The data corresponding to the waveforms were recorded during a PCI procedure in the RCA of a patient with severe stenosis [91]. Figure (3.10a) shows the velocity waveform at the centerline of the inlet to the RCA and Figure (3.10b) shows the pressure waveform at the outlet of the RCA. This pressure is assumed to be constant across the cross-section of the outlet.

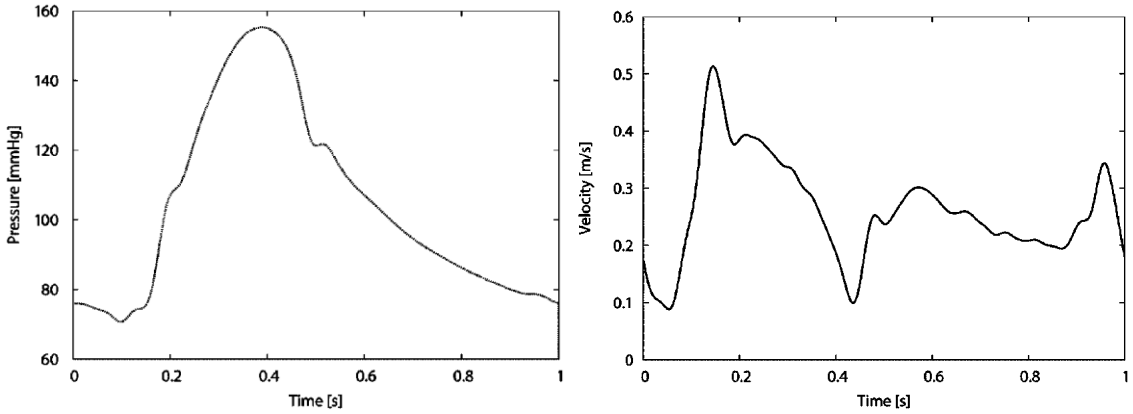

(a) Pressure waveform at the outlet of an RCA (b)Velocity waveform at the centerline of the inlet of an RCA

Figure 3.10: Physiological waveforms [91]

The waveform in Figure (3.10a) represents a patient-specific unsteady pulsatile velocity. However, since it is recorded only at the center of the inlet to the RCA, the data cannot be directly used as the inlet boundary condition. The Womersley velocity equation is commonly used to represent an unsteady, pulsatile blood flow (See Chapter 1, Section 1.3). Since the pressure gradient along the artery is not known, the Womersley velocity equation has to be modified so that it is independent of the pressure gradient. See Appendix C for details on this derivation. The Womersley velocity equation (independent of pressure gradient) is given by Equation (3.11)

$$\Rightarrow u(r,t)=\frac{2q_0}{\pi R^2}\left(1-h^2\right)+\sum_{\substack{n=-M\\ n\neq 0}}^{M}\left[\frac{q_n(r)}{\pi R^2}\frac{\left(1-\dfrac{J_0(\lambda_n r)}{J_0(\lambda_n R)}\right)}{\left(1-\dfrac{2J_1(\lambda_n R)}{R\lambda_n J_0(\lambda_n R)}\right)}\right]e^{in\omega t} \tag{3.11}$$

where

$u(r,t)$ is the time-dependent velocity of the flow

r is the coordinate in the radial direction,

R is the radius of the rigid, straight cylinder,

$$h = r / R \tag{3.12}$$

$$\lambda_n^2 = \frac{i^3 n\omega}{\nu} = i^3 \frac{\alpha_n^2}{R^2} \Leftrightarrow \alpha_n = R\sqrt{\frac{n\omega}{\nu}} \tag{3.13}$$

$$n = 1, 2, 3, \ldots . M \text{ where } M = N / 2 \ \left(\textit{See Appendix B}\right) \tag{3.14}$$

$$\omega = \frac{2\pi}{T} \tag{3.15}$$

T is the time period of the flow,

ω is the angular frequency (pulse frequency) of the flow

ν is the kinematic viscosity of the fluid.

In Equation (3.11) , $q_n(r)$ and q_0 are Fourier coefficients computed using the data from Figure 3.10(a).

Since the pressure waveform shown in Figure 3.10(b) is periodic, it can be represented as a Fourier series (See Appendix B for details) given by

$$p(x,t) = a_{p0} + 2\sum_{n=1}^{M} a_{pn}(x)\cos(n\omega t) + 2\sum_{n=1}^{M} b_{pn}(x)\sin(n\omega t) \tag{3.16}$$

where ω is the angular frequency and is given by Equation(3.16), a_{p0}, a_{pn} b_{pn} are Fourier coefficients that are computed using the data from Figure 3.10(b). The values and details on how the Fourier coefficients ($q_n(r)$, q_0, a_{p0}, a_{pn} b_{pn}) are evaluated is described in Appendix B. It is important to note that the expression for the inlet velocity boundary condition (Equation (3.11)) is a function of the inlet radius, r because:

(a) Since the current analysis involves a moving mesh (See Chapter 2, Section 2.4.1), the radius "r" changes with time. Sometimes, the radius, r is larger than the initially prescribed lumen radius (R). If r>R, then the velocity computed form the equation at the inlet to the blood domain becomes negative and this changes the direction of flow leading to convergence issues. To prevent this from happening, the inlet boundary condition is modified as:

$$u\_inlet(r,t) = (r \le R) * u(r,t) + (r > R) * u_0 \tag{3.17}$$

where $u_0 = 0$ and $u(r,t)$ is given by Equation (3.11)

(b) The current analysis is carried out using the Cartesian coordinates. However, the Womersley velocity profile was derived using the cylindrical coordinate system (See Appendix C). In order to transform the cylindrical coordinates to the Cartesian coordinates, the radial coordinate, 'r' in Equation (3.11) is replaced by

$$r = \sqrt{Y^2 + Z^2}, \tag{3.18}$$

where Y and Z are the Cartesian material coordinates. 'r' can also be defined as

$$r = \sqrt{y^2 + z^2}, \tag{3.19}$$

where y and z are the spatial coordinates. In Equation (3.11),'r' represents the inner radius of the artery in the original geometry (before deformation). Since COMSOL is used for the current study, Equation (3.18) is used to transform the cylindrical coordinates to Cartesian coordinates because in COMSOL, Y and Z are independent material coordinates that relate to the original geometry. Coordinates y and z are spatial coordinates that depend on the moving mesh and, as a result, they are also solution-dependent and, hence, cannot be used [12]. The relation between the material and spatial coordinates is given by Equation(2.11) in Chapter 2.

(c) In COMSOL, the Dirichlet boundary conditions have constraints (restrictions) imposed upon the dependent variables. By default, these constraints are bidirectional constraints. Depending on the physics involved, however, these can be changed to unidirectional constraints. In the current study, the inlet velocity boundary condition given by Equation (3.11) is a normal inflow velocity (and it is also a Dirichlet boundary condition) that involves moving mesh coordinates. For such a condition, it is recommended (by COMSOL) to use a unidirectional constraint [12]. Using bidirectional constraints results in applying the boundary conditions to the moving mesh equations which is not desirable for the current study.

The outlet boundary condition is specified as a "pressure, no-viscous-stress" boundary condition and it is given by

$$p = p(x,t), \tag{3.20}$$

where $p(x,t)$ is given by Equation (3.16). The "pressure, no-viscous-stress" boundary condition is similar to the pressure boundary condition except that it is more stable. For the current study, the pressure, no-viscous boundary conditions resolved some of the convergence issues.

To summarize, the inlet and outlet boundary conditions are as follows:

- Inlet boundary condition:
    - Normal velocity boundary condition
    - Unidirectional constraints
    - Equation(3.17).
- Outlet boundary condition:
    - Pressure, no-viscous-stress boundary condition
    - Equation (3.16) and bidirectional constraints (default option)

Due to the symmetry in the geometry of blood, stent and artery about the x-axis, symmetry boundary conditions are used to reduce the computational domain from a full cylinder to an extruded pie-sector that is 10 times smaller. In COMSOL, the symmetry boundary conditions for the solid domains (artery and stent) ensure that the boundary is free in plane and fixed in the out of plane direction (normal displacement is zero) while for the fluid domain, the symmetry boundary condition prescribes no penetration and vanishing shear stresses.

The equations of the symmetry boundary condition for the fluid are given below [12]

$$u_{fluid} \cdot n = 0 \tag{3.21}$$

$$\left(-pI + \tau\right) \cdot n = 0 \tag{3.22}$$

A roller boundary condition is used on the front and rear faces of the artery. This prevents axial motion of the artery (but does not restrain the radial motion) i.e., the displacement normal to the surface with the roller boundary condition is zero. By constraining the artery axially, it is being assumed that the arterial model being investigated is a part of an artery/circulation system.

In the current study, the outer radius of the stent geometry is equal to the inner radius of the arterial wall. As a result, COMSOL assumes that the stent is always in contact with the arterial wall even when the arterial wall expands due to the blood flow. This is a reasonable assumption because realistically, after the implantation, the stent is not expected to move. Also, as mentioned in Chapter 3, Section 3.1, the off-the-shelf FSI module automatically applies the boundary load at the fluid-solid interface. The details and the expression used by COMSOL to compute this boundary load are given in Chapter 3, Section 3.5.

The displacement of the fluid mesh (prescribed mesh displacement boundary condition) in the xy-plane is constrained in the z-direction; i.e., it does not move in the axial direction. The fluid mesh (prescribed mesh displacement) is also constrained on the inclined plane in a direction normal to the plane. These two prescribed mesh

displacements on the fluid mesh enable the fluid to follow the solid as it displaces (expands or contracts radially). The "free deformation" setting of mesh that determines the equations used for the mesh movement is of the hyperelastic smoothing type. In this study, any other smoothing type resulted in convergence issues. More details and the equations related to the moving mesh and smoothing types, are given in [12].

3.6.1 Inlet boundary condition: Womersley velocity vs steady, parabolic velocity

In the current study, the Womersley number is 1.9. It is computed as follows:

$$\alpha = R\sqrt{\frac{\omega}{\nu}} = 0.00141\sqrt{\frac{(2\pi/1)}{(0.0035/1050)}} \sim 1.9 \tag{3.23}$$

If the Womersley number is less than 1, the inlet velocity profile can be approximated by a parabolic velocity profile (See Chapter 1, Section 1.3). However, from Figure (3.11), it can be seen that the pulsatile component of the Womersley velocity profile is significant and cannot be ignored. At t = 0.15 s (this is where the inlet velocity is the maximum), the average percentage difference between the Womersley velocity and the steady parabolic velocity is about 40%. Moreover, considering the pulsatile velocity makes the flow more realistic. Figure (3.11) was plotted by evaluating Equation (3.11) at different values of r and t.

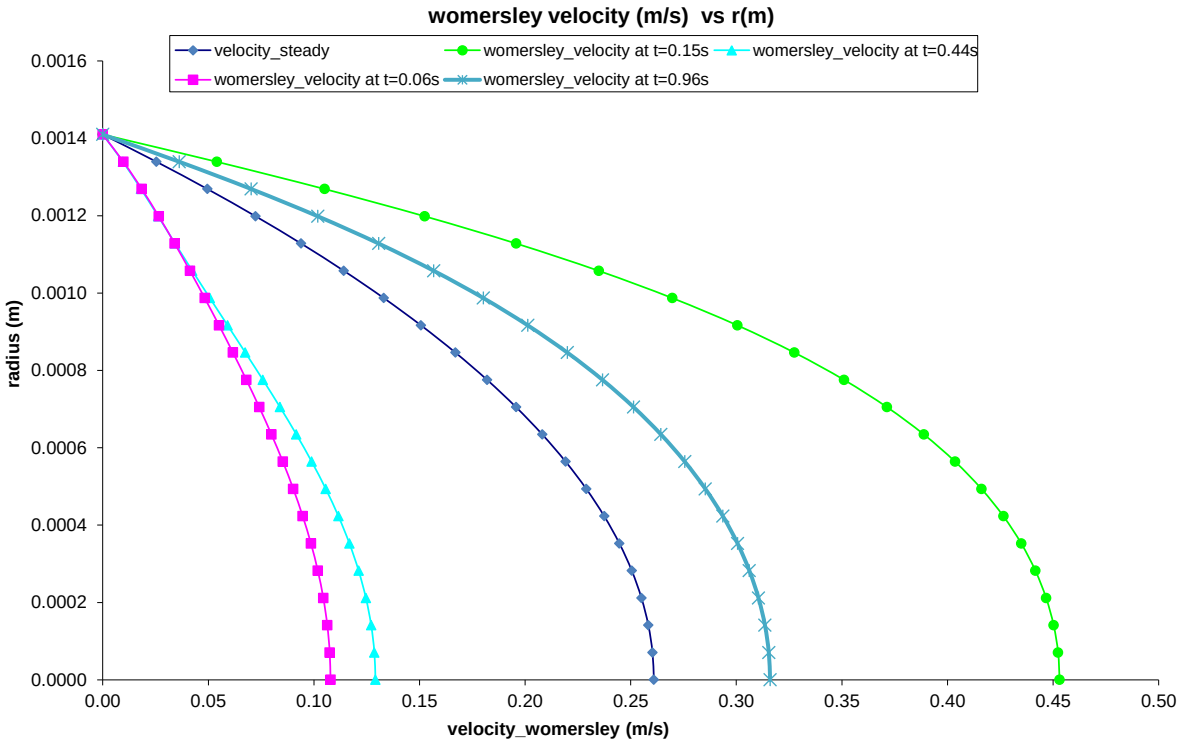

Figure 3.11: Plot of Womersley velocity as a function of radius (at the inlet face to the geometry)

3.7 Finite element method

As mentioned in Chapter 3, Section 3.4, the first step in a finite element analysis is to discretize the physical domain. Upon discretization, linear, quadratic or higher order elements are used to represent the geometry and an approximate solution is computed for the dependent variables using interpolation functions. For example, consider the dependent variable, velocity (u), which can be approximated as follows:

$$u = \sum_{j=1}^{n} U_j \phi_j, \tag{3.24}$$

where U_j are the values of u at each node of an element. U_j is also called as the solution vector. ϕ_j is the approximate function that is usually represented by a polynomial and these are derived using the interpolation theory [80]. Hence the name interpolation functions. When the approximate functions are expressed in terms of the local coordinates, they are known as shape functions [11]. It is assumed that the dependent variables are continuous. It is these shape functions that determine the order of the element (linear, quadratic etc.). More details about the shape functions and the finite element method are found in references [11], [80]. The current study uses linear order elements in both the fluid and the solid domains. The fluid domain uses P1+P1 elements (first order interpolation function to approximate velocity and pressure and the solid domain uses linear elements to approximate the displacement. See [10] for a more detailed description.

Given the PDE, boundary conditions, and the interpolation functions, COMSOL solves the problem by converting the PDE to a weak form. "A weak form of a differential equation is defined to be a weighted-integral statement of a differential equation in which the differentiation is transferred from the dependent variable to the weight function such that all natural boundary conditions of the problem are also included in the integral statement"[80]. More details about the weak form can be found in [11]. COMSOL uses the Galerkin method to discretize the weak form PDE. In order to handle numerical instabilities, COMSOL uses the streamline and crosswind diffusion methods. For details see the [11].

3.8 Research problem and COMSOL solver details

In order to achieve the objective of the current study, two different sub-studies are carried out viz., FSI sub-study and no-FSI sub-study. The FSI sub-study was built using the boundary conditions shown in Figure (3.9) and the no-FSI sub-study was built using the boundary conditions shown in Figure (3.12). The differences between the finite element models that use these studies are listed in Table (3.3).

Table 3.3: Important differences between FSI and no-FSI models

		FSI	No-FSI
1.	Force acting on the fluid-solid interface	Force is included and it given by Equation (3.7)	No force is acting on the wall. Equation (3.7) is not included.
2.	Mesh	Moving	Fixed
3.	Domains used in the analysis	Artery, stent and blood	Blood (artery and stent are a part of the geometry but there is no physics assigned to them)
4.	Equations representing the physics	(3.5), (3.7),(3.9) (3.10), (2.11)	(3.5), (3.9)
5.	Equation at the interface (FSI) or wall (no-FSI)	(3.7)	u = 0 (no slip)
6.	Boundary conditions	Figure (3.9)	Figure (3.12)

Discretization of the domain of interest using finite elements converts the weak form of the equations modeling the solid and flow domains into a large system of nonlinear algebraic equations. To state the COMSOL solution algorithm briefly, first an initial estimate of the solution is used to linearize the system. The linearized system is

then solved using a user-selected linear solver (see below). COMSOL then uses “an affine invariant form of the damped Newton method” to solve the nonlinear system [11]. For more details see [11]

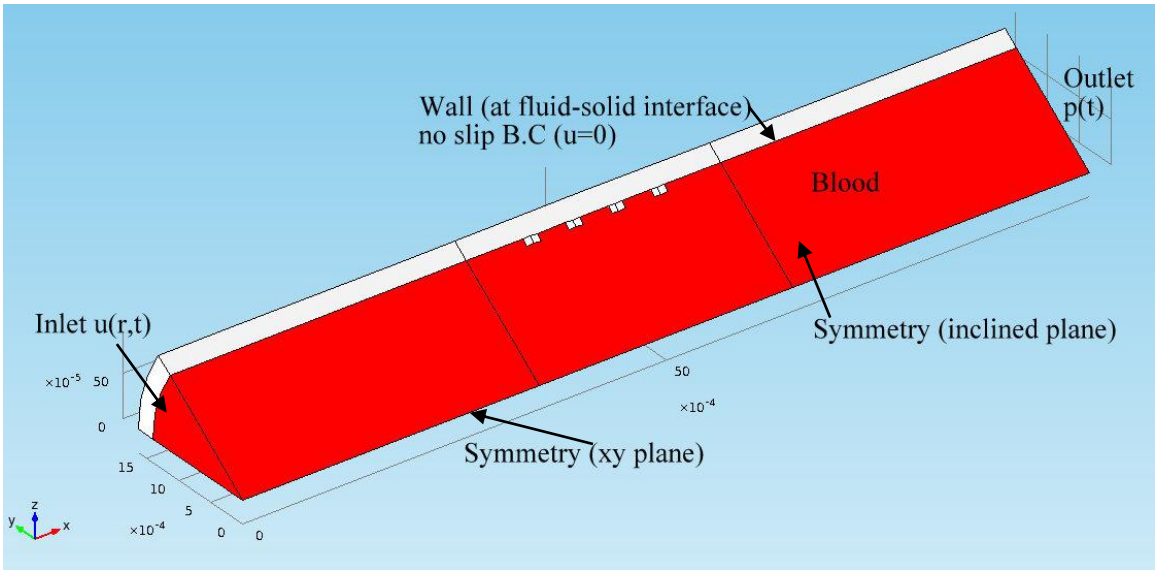

Figure 3.12: Boundary conditions used in the current study (for no-FSI sub-study)

In COMSOL, linear solvers can be divided into two categories which are: direct solvers and iterative solvers. Since the current study uses a direct solver (and not iterative solver) for both FSI and no-FSI sub-studies, some details about the direct solver are given below. For details about the COMSOL iterative solver, see [11]. The direct solver uses an LU factorization to solve for the unknown variable. L stands for lower and U stands for upper triangular matrix of the coefficient matrix. For example, when solving for a system of the form Ax=B [11] , the direct solver uses LU factorization on the coefficient matrix A and computes the unknown (dependent variables), ‘x’. COMSOL has three different direct solver algorithms, and they are the MUltifrontal Massively Parallel sparse direct solver (MUMPS), the PARDISO solver, and the Sparse Object Oriented Linear

Equations Solver (SPOOLES). The current study uses the MUMPS solver because as in COMSOL version 4.2a, it is recommended to run MUMPS when running a simulation in distributed mode (with cluster or parallel processors).

A solver can use a fully coupled approach or a segregated approach. In a fully coupled approach, the fluid and the solid equations are solved simultaneously instead of sequentially (See Chapter 2, Section 2.4). In the no-FSI sub-study, using a fully coupled approach means that the fluid velocity and pressure are solved simultaneously. In a segregated approach the fluid and the solid equations are solved sequentially. A fully coupled approach helps when the physics are strongly coupled. Both the FSI and the no-FSI sub-studies used a fully coupled approach.

On a different note, the time-dependent solver in COMSOL uses two kinds of implicit solvers which are the Generalized-alpha and backward differentiation formula (BDF) solvers. More details about these methods can be located in [11].

The skeleton of the research problem is shown in Figure (3.13)

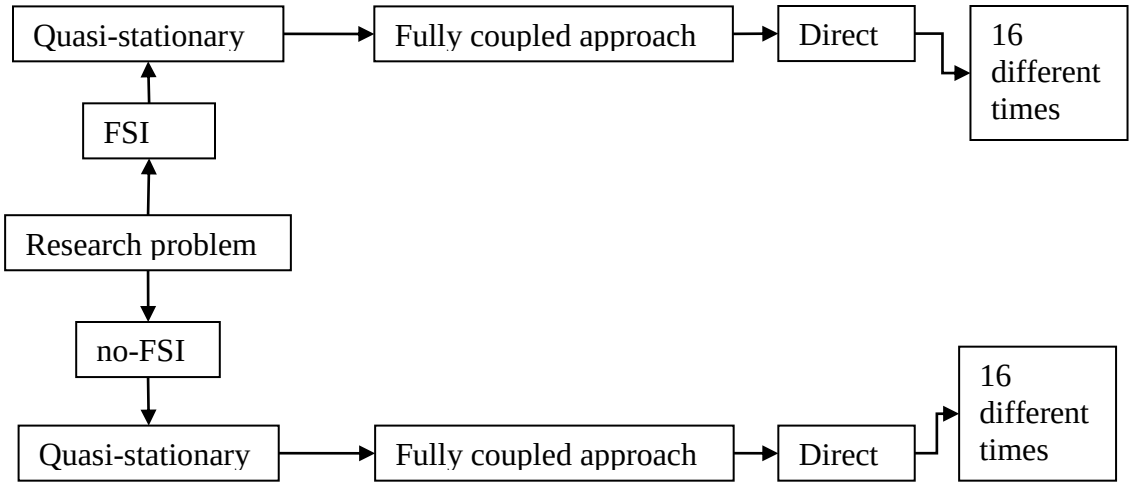

Figure 3.13: Summary of research problem

In COMSOL, when the relative error, E, is below a specified relative tolerance, the solution is said to be converged. The relative error is computed on the solution vector (i.e., the dependent variable matrix that is being solved for in the equations). The relative error is computed as the weighted Euclidean norm given as [11]:

$$err = \left(\frac{1}{N} \sum_{i=1}^{N} \left(\frac{|E_i|}{W_i} \right)^2 \right)^{1/2} \tag{3.25}$$

where

$$W_i = \max\left(|U_i|, S_i \right) \tag{3.26}$$

N is the number of degrees of freedom (DOF). S_i is a scale factor that solver determines on the basis of the scaling method (automatic, manual, initial value based and none). For the current study this scaling method is chosen as automatic. See [11] for more details about these methods. In the current study, the relative tolerance is set to 0.001. More details about the basis for selecting this relative tolerance are presented in Chapter 4, Section 4.4.

The current study is a quasi-stationary study (See Chapter 3, Section 3.3) which means that the equations are solved for steady flow but the boundary conditions are time-dependent and the simulation is run for 16 different times during the period of the boundary conditions: t = 0, 0.06, 0.07, 0.14, 0.15, 0.20, 0.37, 0.40, 0.44, 0.49, 0.50, 0.57,0.70,0.86,0.96,1s. These times correspond to the time when the maximum velocity, minimum velocity, maximum pressure, minimum pressure occur locally in the waveforms shown in Figures 3.10 (a) and (b). The results of the two sub-studies are presented in the next chapter.

4. RESULTS AND DISCUSSION

The current study comprises of two sub-studies which are the FSI sub-study and the no-FSI sub-study (See Chapter 3, Section 3.8, for more details on the sub-studies). The data was extracted at 16 different times (for both the sub-studies).However, only the results presented in Chapter 4, Section 4.9 use the data corresponding to all the 16 times. Most of the other results presented in this chapter use the data corresponding to one or all of the following four specific times which are t = 0.06 s, 0.15 s, 0.44 s, 0.96 s. These four specific times were selected because the inflow velocity and outflow pressure waveforms (Figure 3.10(a) and (b)) show that the:

- global maximum velocity occurs at t = 0.15 s
- global minimum velocity occurs at t = 0.44 s. This also corresponds to the global maximum pressure
- global minimum pressure occurs at t = 0.06 s.

The fourth point (t = 0.96 s) is selected because the velocity profile changes abruptly at this time. Wall shear stress (WSS), Wall shear stress gradient (WSSG), Oscillatory shear index (OSI), and Time-averaged wall shear stress (TAWSS) are the four parameters of interest. Chapter 2, Section 2.3 lists a few journal papers that correlate these parameters with the occurrence of restenosis and NIH.

Below are the expressions that are used to compute these parameters:

- **WSS:** Equation (4.1) is used to compute the WSS, τ

$$\tau = \dot{\gamma}\mu, \tag{4.1}$$

where $\dot{\gamma}$ is the magnitude of the shear rate tensor given by Equation (4.2) and μ is the dynamic viscosity. See Chapter 2, Section 2.3 for more details.

$$\dot{\gamma} = \sqrt{\frac{1}{2}\begin{pmatrix} 4\left(\frac{\partial u}{\partial x}\right)^2 + 2\left(\frac{\partial u}{\partial y}+\frac{\partial v}{\partial x}\right)^2 + 2\left(\frac{\partial u}{\partial z}+\frac{\partial w}{\partial x}\right)^2 + \\ +4\left(\frac{\partial v}{\partial y}\right)^2 + 2\left(\frac{\partial v}{\partial z}+\frac{\partial w}{\partial y}\right)^2 + 4\left(\frac{\partial w}{\partial z}\right)^2 \end{pmatrix}} \tag{4.2}$$

Since the objective of this computational study is to show how the FSI influences the magnitude of WSS, there are many sub-studies carried out on this (WSS) parameter. These WSS results are presented in Sections 4.1 to 4.6.

- **WSSG:** From Chapter 2, Section 2.3, the expression for the WSSG is given by

$$WSSG = \sqrt{\left(\frac{\partial \tau_m}{\partial m}\right)^2 + \left(\frac{\partial \tau_n}{\partial n}\right)^2}, \tag{4.3}$$

where τ_m and τ_n are the shear stress in the ‘m’ (local coordinate in the direction of the WSS) and ‘n’ directions (‘n’ is normal to the ‘m’ direction and it is the local coordinate in the tangential direction to the surface containing ‘m’ and ‘n’ coordinates). Using Equation(4.3), an unsuccessful attempt was made to compute the WSSG on the edge shown in Figure (4.1). The attempt was not successful because it was difficult to determine the magnitude of WSS in the local coordinates.

- **TAWSS**: The expression for TAWSS is given by

$$TAWSS = \overline{|\vec{\tau}|} = \frac{1}{T}\int_0^T |\vec{\tau}_w| dt = \frac{1}{T}\sum_{i=1}^{n}\left(\sqrt{\left(\tau_{x_i}^2 + \tau_{y_i}^2 + \tau_{z_i}^2\right)} dt_i\right), \tag{4.4}$$

where τ_x, τ_y, and τ_z are the magnitudes of shear stress in the x, y, and z directions. See below for more details on how to compute this expression.

- **OSI**: The expression for OSI is given by Equation (4.5)

$$OSI = \frac{1}{2}\left(1 - \frac{\left|\int_0^T \vec{\tau}\, dt\right|}{\int_0^T |\vec{\tau}| dt}\right) = \frac{1}{2}\left(1 - \frac{\sqrt{\left(\left(\sum_{i=1}^{n}\tau_{x_i} dt_i\right)^2 + \left(\sum_{i=1}^{n}\tau_{y_i} dt_i\right)^2 + \left(\sum_{i=1}^{n}\tau_{z_i} dt_i\right)^2\right)}}{\sum_{i=1}^{n}\left(\sqrt{\left(\tau_{x_i}^2 + \tau_{y_i}^2 + \tau_{z_i}^2\right)} dt_i\right)}\right) \tag{4.5}$$

Equations (4.4) and, (4.5) are deduced from Equations(2.5), (2.10) in Chapter 2, Section 2.3. In the current study, n = 15. As mentioned at the beginning of this chapter, the data was extracted at 16 different times (including t = 0 and t = 1 s, both of which represent the same data points in the periodic inlet velocity and outlet pressure waveforms). Hence n = 15. It is important to note that the Equations (4.4) and (4.5) are actually defined for a time-dependent problem. Since the current study is a quasi-stationary study, the magnitude of WSS is evaluated at discrete times. Hence, the integral symbol in Equations(4.4) and (4.5) is replaced by the summation symbol. In order to compute the TAWSS, the values of τ_x, τ_y, and τ_z at each of the 16 different times are extracted from COMSOL.

Below is a brief summary of the sub-studies that have been carried out to achieve the objective of the current study. The results of other small studies that were completed in the process of achieving this objective are also presented in this chapter:

- Mesh convergence study for the FSI and no-FSI cases
- Comparison of WSS for the FSI and no-FSI sub-studies using the finest mesh
- Tolerance selection criteria for the current study
- Magnitude of TAWSS and OSI for FSI and no-FSI sub-studies

4.1 Mesh Convergence Study

For both FSI and no-FSI sub-studies, mesh convergence was evaluated using the five meshes described in Chapter 3, Section 3.4. Magnitude of WSS was used to evaluate the mesh convergence. The WSS data were extracted along a selected edge (edge highlighted in blue in Figures 4.1 (a) and (b)). Sections 4.1.1 and 4.1.2 present the results of the mesh convergence study for the FSI and no-FSI sub-studies, respectively. In the results, the abbreviations 'ebe' and's' stand for edge-by-edge and stent. The edge-by-edge indicates that the data was collected one line segment at a time. In other words, the edge shown in Figure 4.1 (a) and (b) is made up of 23 line segments (or 23 entities). At any given instance, the x-coordinates and WSS data were collected for one entity at a time. Then the data for each entity were sorted in ascending order (of the x-coordinate) before combining it with the adjacent entity. A table was created with the sorted data corresponding to all 23 entities that make up the edge (highlighted in blue in Figure 4.1(a)) and this table was used to plot all the figures. This methodology was followed because extracting the data in one-step for the entire highlighted edge resulted in some data plotting issues due to the presence of duplicate nodes (See Section 4.5 for details).

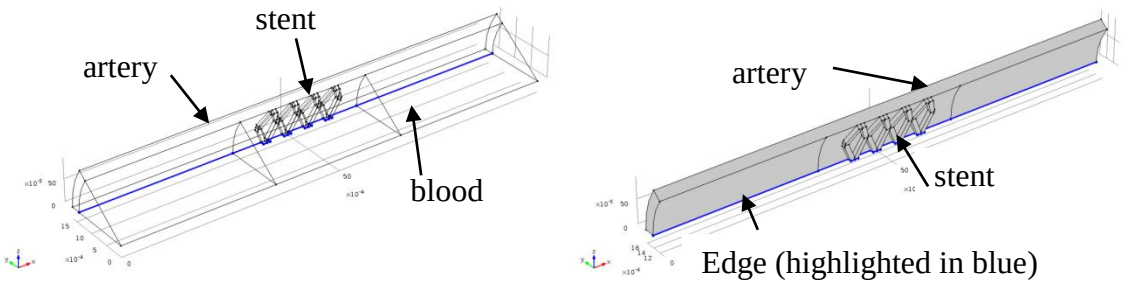

(a) View 1 (b) View 2

Figure 4.1: Edge used for mesh convergence

4.1.1 Mesh Convergence Study (FSI)

Figures 4.2 (a), (b), (c) and (d) show the WSS computed along the entire edge while the Figures 4.3 (a), (b), (c) and (d) show the results near the strut region (for clarity purposes). Both these sets of figures are plotted using the data from the FSI sub-study and the data were extracted at the edge shown in Figure (4.1). The Figures (a), (b), (c) and (d) correspond to the four different times t = 0.06 s, 0.15 s, 0.44 s and 0.96 s. Figures 4.4(a) and 4.4(b) show the enlarged view of the mesh convergence study at t = 0.44 s. The 'green line' in the plots is the 2D projection of the edge shown in Figure (4.1).

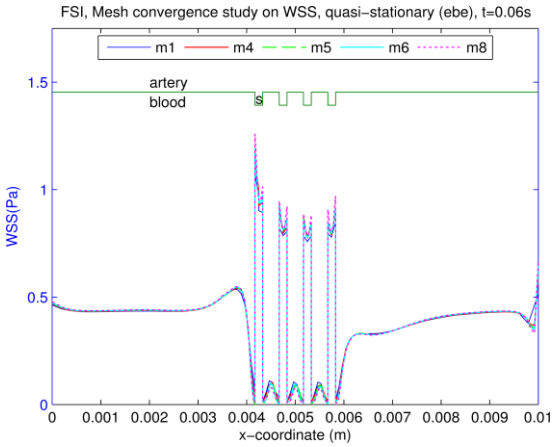

(a)WSS at t = 0.06 s

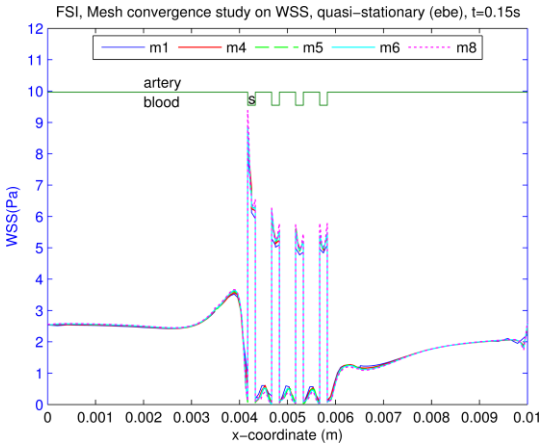

(b) WSS at t = 0.15 s

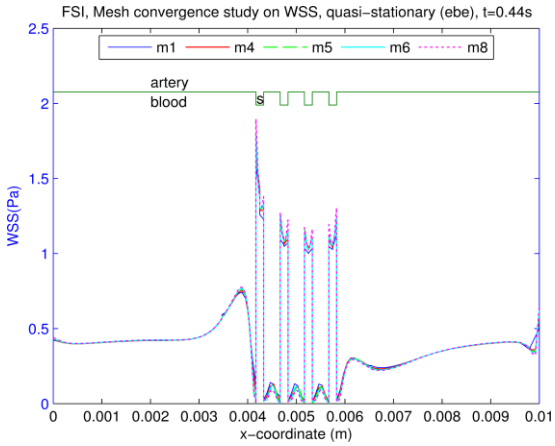

(c)WSS at t = 0.44 s

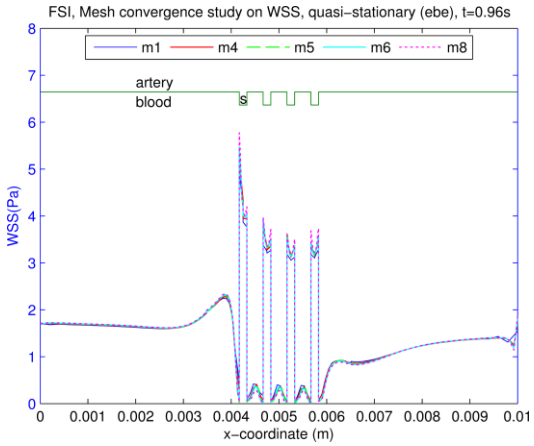

(d) WSS at t = 0.96 s

Figures 4.2: Mesh convergence study on WSS, FSI, quasi-stationary

(a)WSS at t = 0.06 s

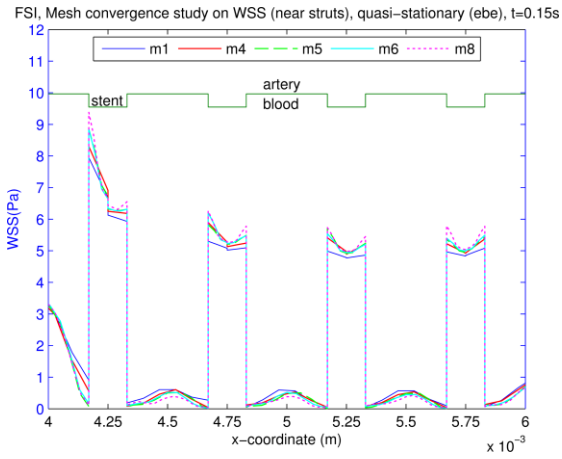

(b) WSS at t = 0.15 s

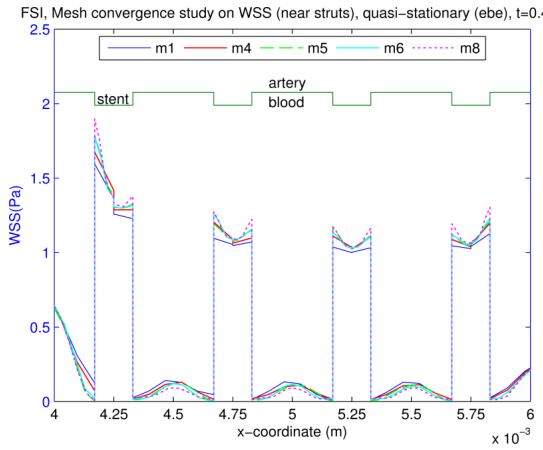

(c)WSS at t = 0.44 s

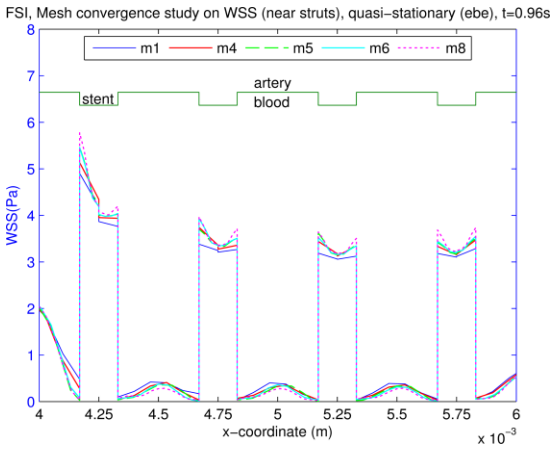

(d) WSS at t = 0.96 s

Figures 4.3: Mesh convergence study on WSS near struts, FSI, quasi-stationary

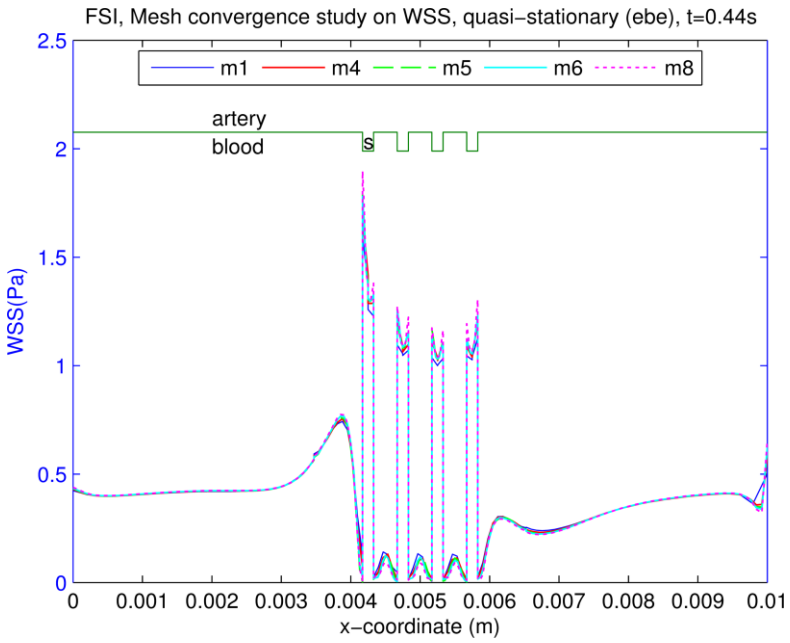

(a) WSS on the entire edge

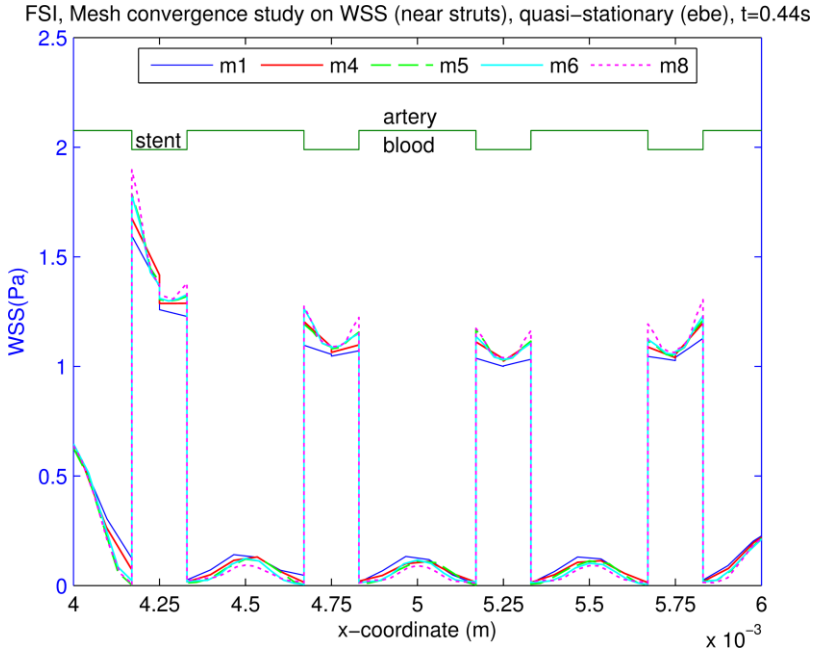

(b)WSS near the struts

Figures 4.4: Mesh convergence study on WSS, FSI, quasi-stationary, t = 0.44 s (enlarged view)

The results of this mesh convergence study show that the regions between the struts are reaching mesh independence while the regions before and after the strut are clearly mesh independent. Although it would be desirable to test an even finer mesh in the neighborhood of the stent, available computational resources are not capable of supporting that simulation. Further, it was observed that in many instances the small changes in WSS (between the struts) accompanying mesh refinements were oscillating in magnitude providing further confidence in the convergence of the mesh study. Hence the finest mesh, M8, is used for evaluating the results in all the studies.

4.1.2 Mesh Convergence Study (no-FSI)

Figures 4.5 (a), (b), (c) and (d) show the WSS computed along the entire edge while the Figures 4.6 (a), (b), (c) and (d) show the results near the strut region (for clarity purposes). The data used to plot these results were extracted at the edge shown in Figure (4.1) and they are from the no-FSI sub-study. The Figures (a), (b), (c) and (d) correspond to the four different times t = 0.06 s, 0.15 s, 0.44 s and 0.96 s. Figures 4.7(a) and (b) show the enlarged view of the mesh convergence study for the no-FSI case at t = 0.44 s.

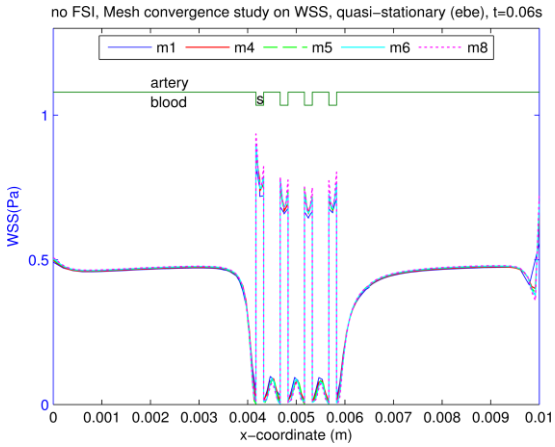

(a)WSS at t = 0.06 s

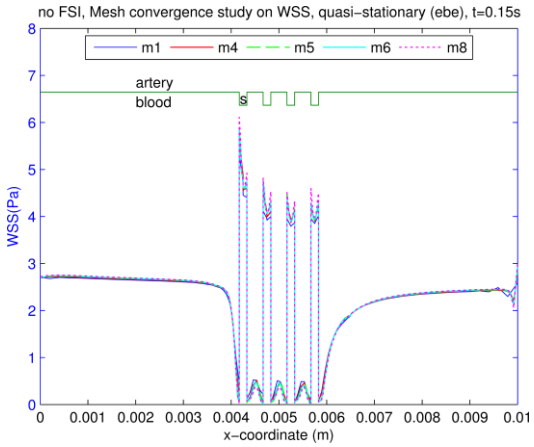

(b) WSS at t = 0.15 s

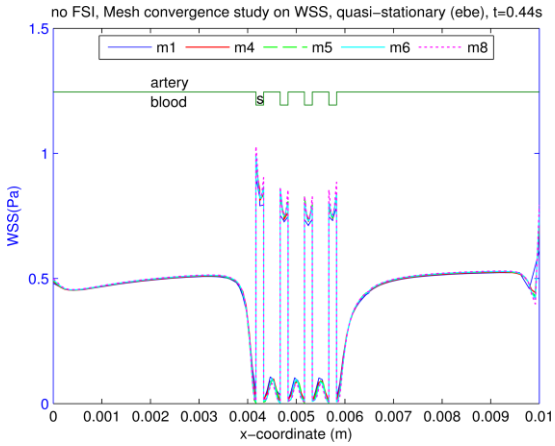

(c)WSS at t = 0.44 s

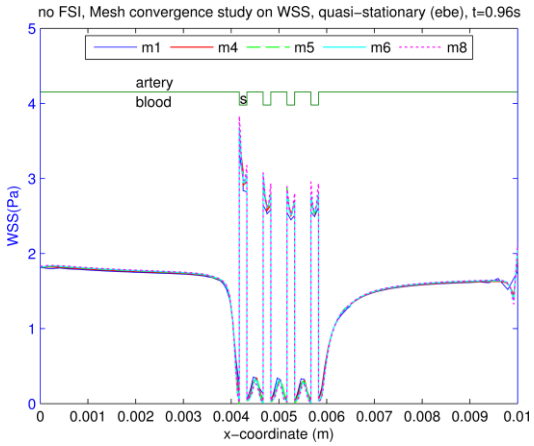

(d) WSS at t = 0.96 s

Figures 4.5: Mesh convergence study on WSS, no-FSI, quasi-stationary

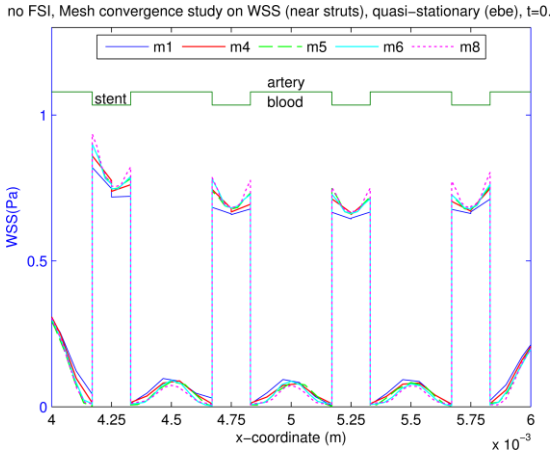

(a)WSS at t = 0.06 s

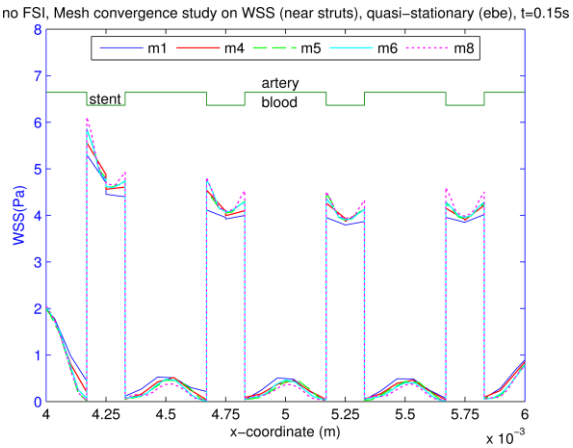

(b) WSS at t = 0.15 s

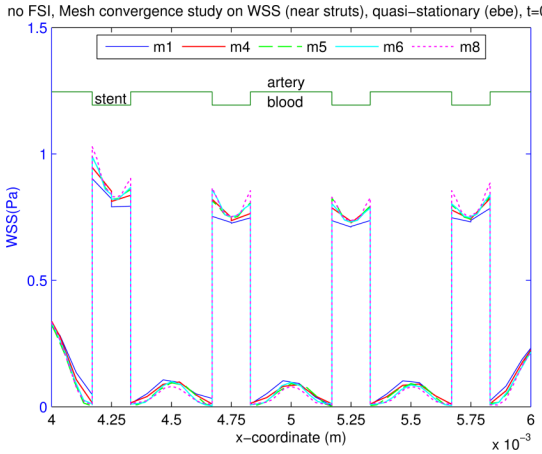

(c)WSS at t = 0.44 s

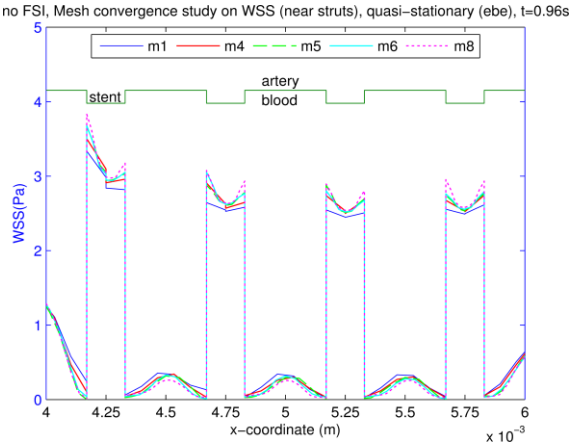

(d) WSS at t = 0.96 s

Figures 4.6: Mesh convergence study on WSS near struts, no-FSI, quasi-stationary

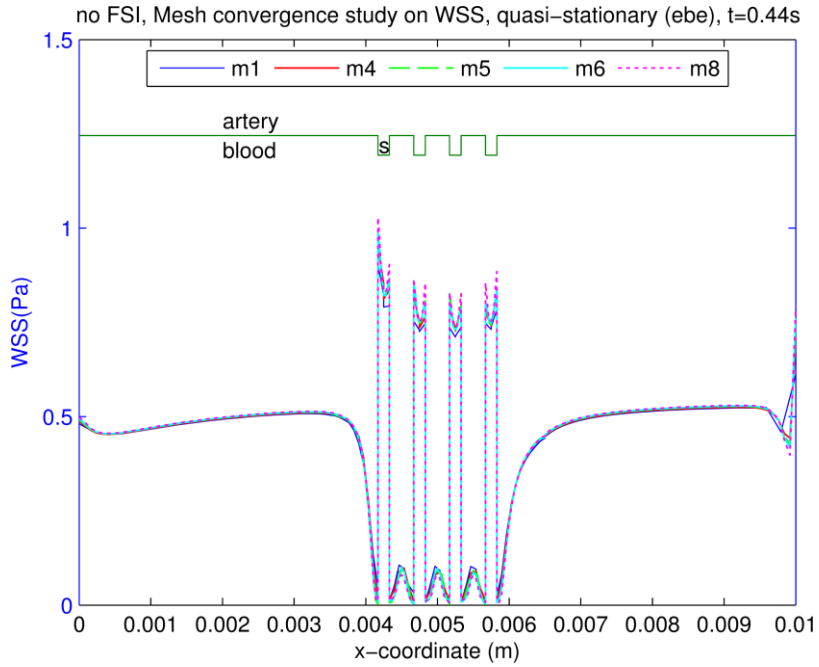

(a)WSS on the entire edge

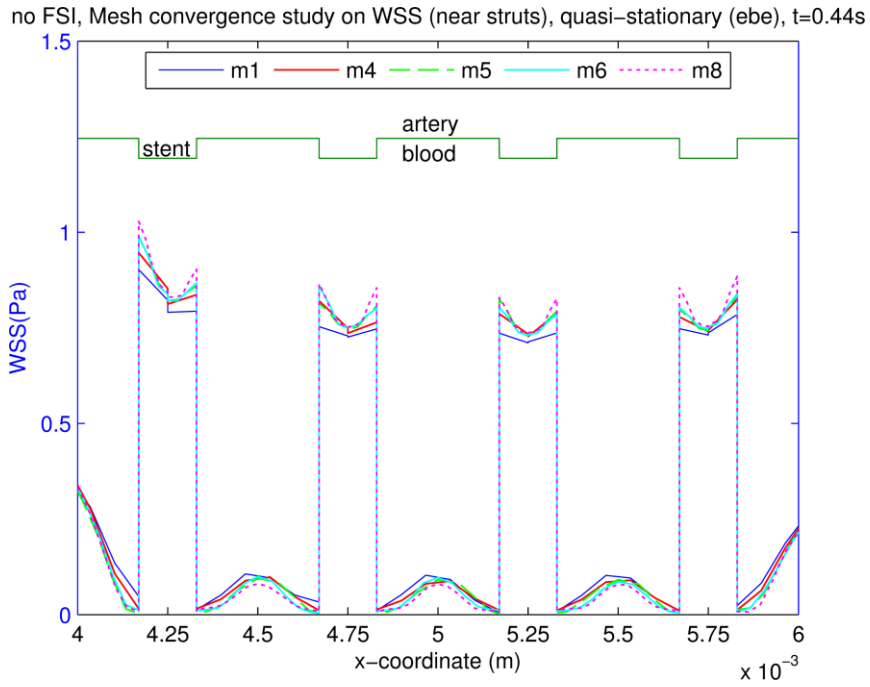

(b)WSS near the struts

Figures 4.7: Mesh convergence study on WSS, no-FSI, quasi-stationary, t = 0.44 s

The results of this mesh convergence study show that the regions between the struts are reaching mesh independence while the regions before and after the strut are clearly mesh independent. Although it would be desirable to test an even finer mesh in the neighborhood of the stent, available computational resources are not capable of supporting that simulation. Further, it was observed that in many instances the small changes in WSS accompanying mesh refinements were oscillating in magnitude providing further confidence in the convergence of the mesh study. Hence the finest mesh, M8, is used for evaluating the results in all the studies.

4.2 FSI versus no-FSI

All the data in this section were computed using the finest mesh, M8, and the results presented here were extracted from the edge shown in Figure 4.1(a) and (b). This study compares the WSS for the FSI and the no-FSI sub-studies. Figures 4.8 (a), (b), (c) and (d) show the results on the entire edge while the Figures 4.9 (a), (b), (c) and (d) show the results near the strut region (for clarity purposes). The Figures (a), (b), (c) and (d) correspond to the four different times t = 0.06 s, 0.15 s, 0.44 s and 0.96 s. Figures 4.10(a) and (b) show the enlarged view of the WSS for the FSI and no-FSI results at 0.44 s.

It can be observed that in the region away from the struts, the magnitude of the WSS for the FSI sub-study is lower than the magnitude of the WSS for the no-FSI sub-study (See Figure (4.8)). This can be explained by the wall compliance of the FSI sub-study. As the pressure in the blood domain increases, the radius of the vessel also increases. Consequently, the velocity decreases resulting in a lower WSS compared to the WSS from the no-FSI sub-study (which has no wall compliance). Figure (4.8) also shows that the magnitude of WSS (from FSI sub-study) increases and decreases rapidly just

before the stent region. On the stent surface, the WSS magnitude is higher for the FSI sub-study. In the region between the struts (where restenosis occurs), the results of the two sub-studies are close to each other (See Figure (4.9)). The shape of the WSS curves on the stent, in between the struts, in the proximal and in the distal regions of the geometric model is similar for the FSI and no-FSI sub-studies. The primary area of interest in the current study is the region between the struts because this is where the restenosis occurs. Hence, some more WSS studies were carried out in this region.

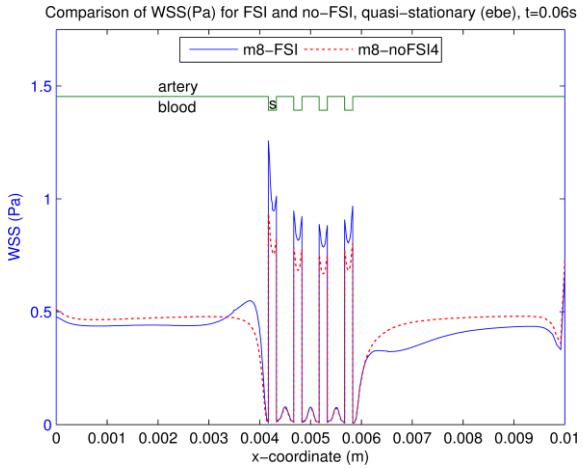

(a)WSS at t = 0.06 s

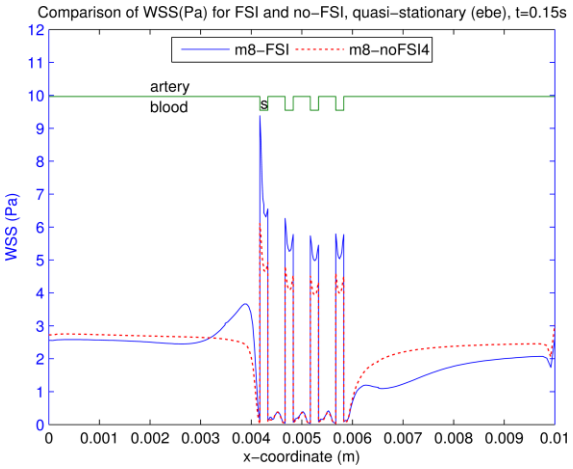

(b)WSS at t = 0.15 s

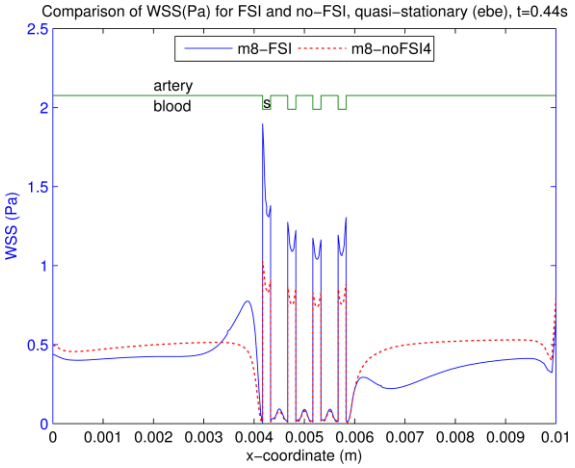

(c)WSS at t = 0.44 s

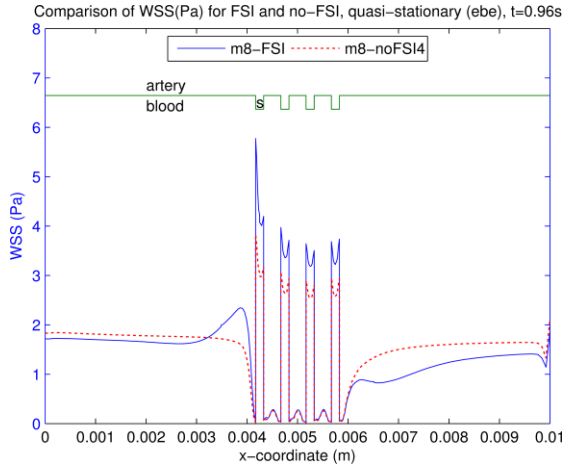

(d)WSS at t = 0.96 s

Figure (4.8): WSS for the FSI vs no-FSI, quasi-stationary

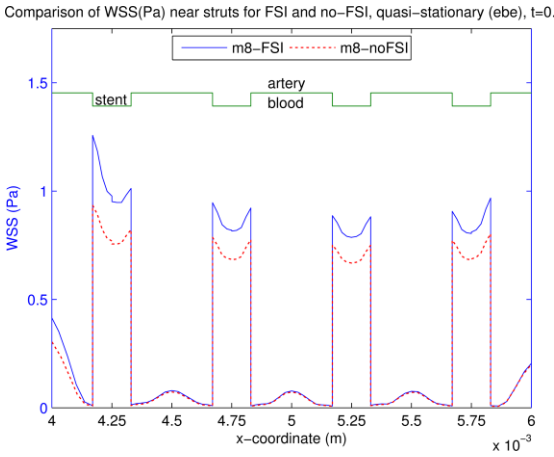

(a)WSS at t = 0.06 s

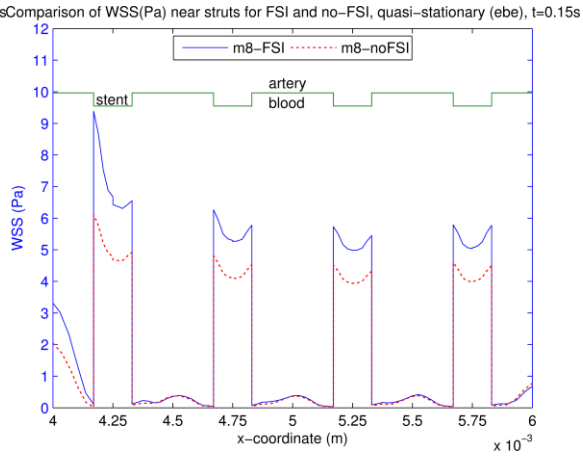

(b) WSS at t = 0.15 s

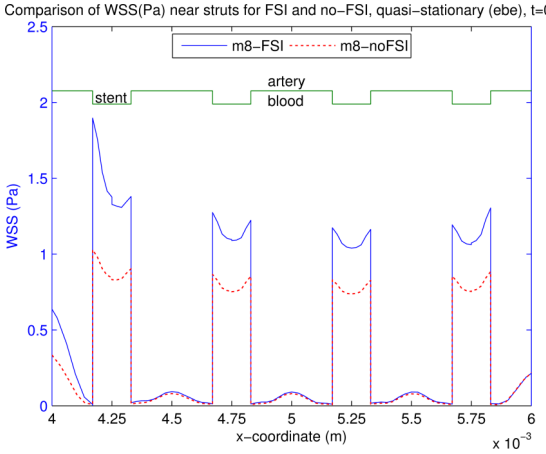

(c)WSS at t = 0.44 s

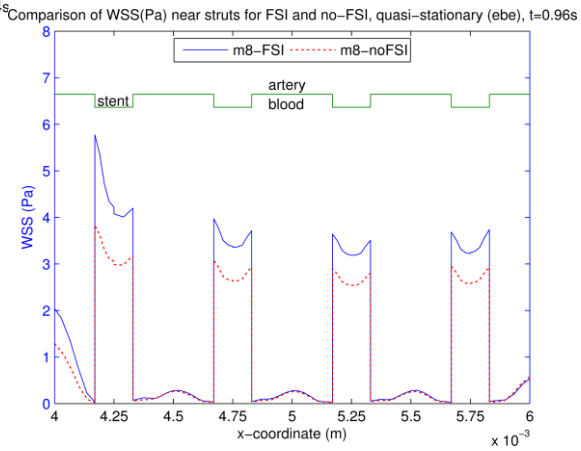

(d) WSS at t = 0.96 s

Figure 4.9: WSS for FSI vs no-FSI, quasi-stationary

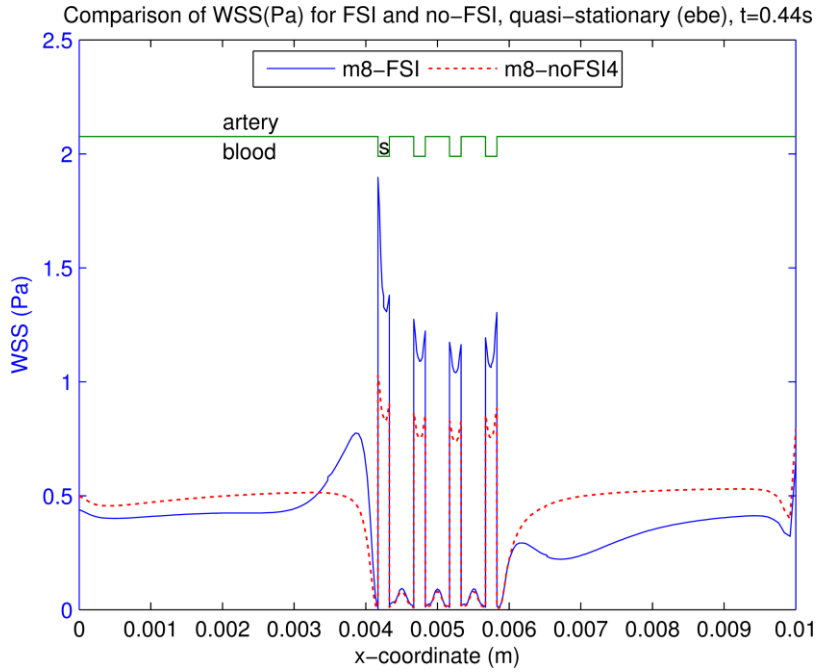

(a) WSS on the entire edge

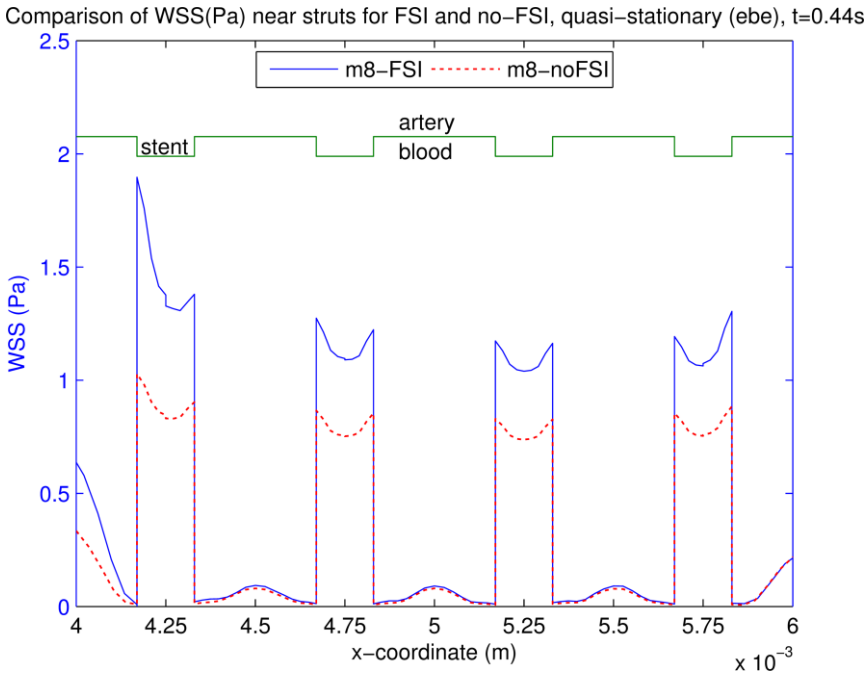

(b)WSS near the struts

Figure 4.10: WSS for FSI vs no-FSI, quasi-stationary t = 0.44 s (enlarged view)

Figures 4.11(a), (b), (c) and (d) show the percentage error in the WSS as a function of the x-coordinate. The percentage error is computed as %error =abs (WSS_{FSI}-WSS_{NFSI})/WSS_{FSI} and is presented for simulations at times t = 0.06 s, 0.15 s, 0.44 s and 0.96 s. On the edge shown in Figure 4.1(a) and (b), the error analysis was carried out only at those regions where the artery is exposed to the blood flow (no percentage error was computed on the stent surface. The percentage error was not computed on the stent because NIH is related to the magnitude of WSS on the arterial wall (and not due to the magnitude of WSS on the stent wall). Please note that the x-coordinate used in Figure (4.11) corresponds to the x-coordinate of the edge (in Figure 4.1 (a) and (b)) from the FSI sub-study. The FSI sub-study includes wall compliance. As a result, the x-coordinate of the FSI sub-study is slightly different from the x-coordinate for the no-FSI sub-study. Since the magnitude of difference in x-coordinates is in the order of 10^{-5}, the error introduced should be negligible for the purposes of the present study.

Figure (4.11) demonstrates that between the struts and in the distal region of the geometric model, the results of the FSI sub-study are noticeably different from the no-FSI sub-study. In between the struts, the percentage error between the FSI and no-FSI sub-studies varies from 1% to 50% depending on the velocity and pressure magnitude (i.e. based on the time ‘t’ when the results are evaluated).

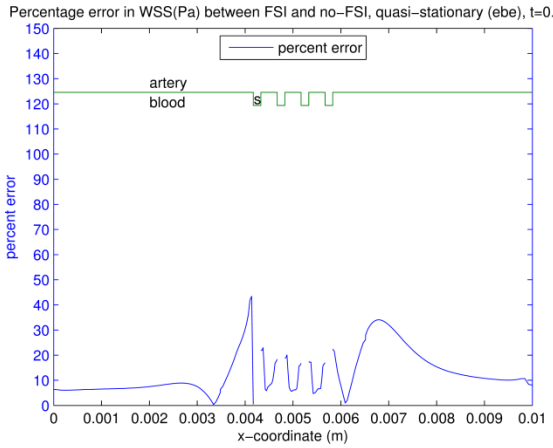

(a)Percentage error at t = 0.06 s

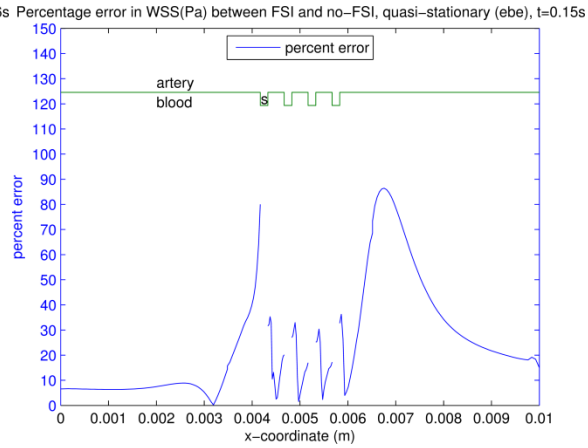

(b) Percentage error at t = 0.15 s

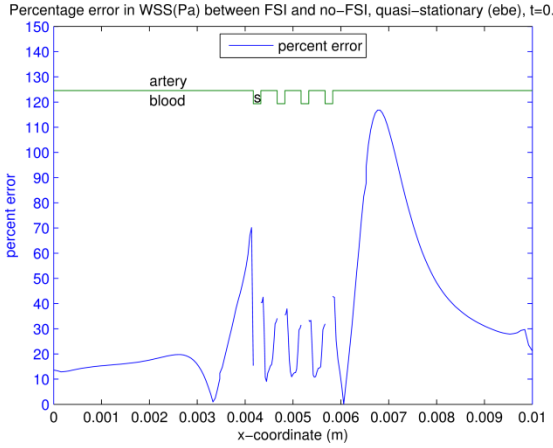

(c) Percentage error at t = 0.44 s

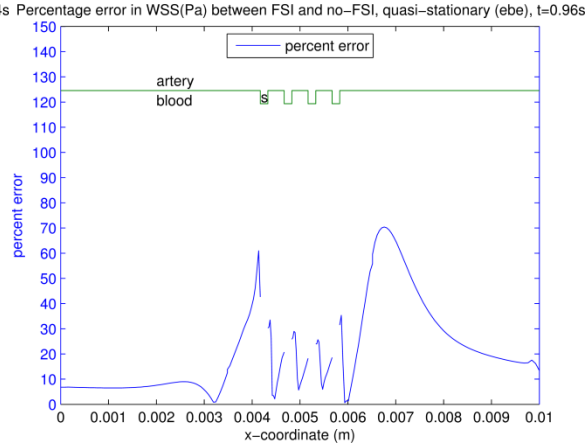

(d) Percentage error at t = 0.96 s

Figures 4.11: Percentage error in WSS for FSI vs no-FSI, quasi-stationary

4.3 FSI versus no-FSI (edge vs other locations)

In this study, the WSS computed on the 3 edges (shown in Figure 4.12) is compared with the WSS obtained along the line segments shown in Figure (4.12) and (4.13). This study was carried out for both the FSI and no-FSI sub-studies. Mesh, M8 is used for this analysis and the results are presented at times, t = 0.06, 0.15, 0.44 and 0.96 s. The line segments (8 different line segments) which are located in between the struts (on the artery-blood interface) were selected to be parallel to the axial direction. Four line segments make an angle of 12° with the y-axis. The other set of line segments (four more) are also parallel to the x-axis but they make an angle of 20° with the y-axis. Figures (4.12) and (4.13) show the locations of these line segments. Figure (4.13) presents the view of the blood domain when looking at it from the inflow side (the arterial domain is not shown). The red dots in this figure represent the line segments of interest. Figure (4.12) shows the stent and line segments (artery and blood are not shown for clarity purposes). Also, the stent in Figure (4.12) is presented at an angle that is not aligned with the axis. This particular view was chosen because it gives a better view of the location of the line segments.

On each of these 8 line segments, the user has defined five locations where the values of the WSS are to be computed. Hence there are 40 points (5 points per line segment and there are 8 line segments) where the WSS is computed. These user-defined coordinates are represented by the black dots (points) on the red lines shown in Figure (4.14). The line segments (2 out of 8), user-defined points and the nearest nodal locations in the first strut are shown in Figure (4.14). The location of these entities is similar in the remaining struts.

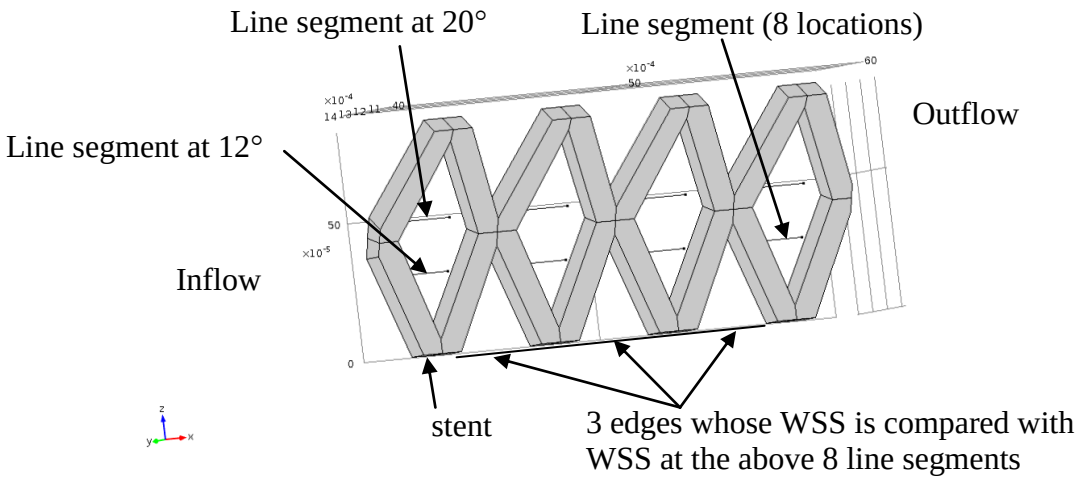

Figure 4.12: Edges and line segments used in Section 4.3

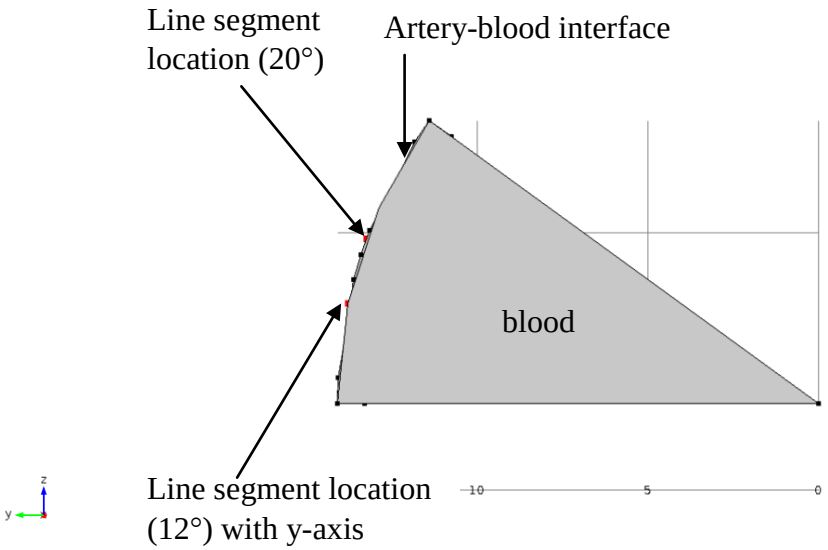

Figure 4.13: Edges and line segments used in Section 4.3: a different view

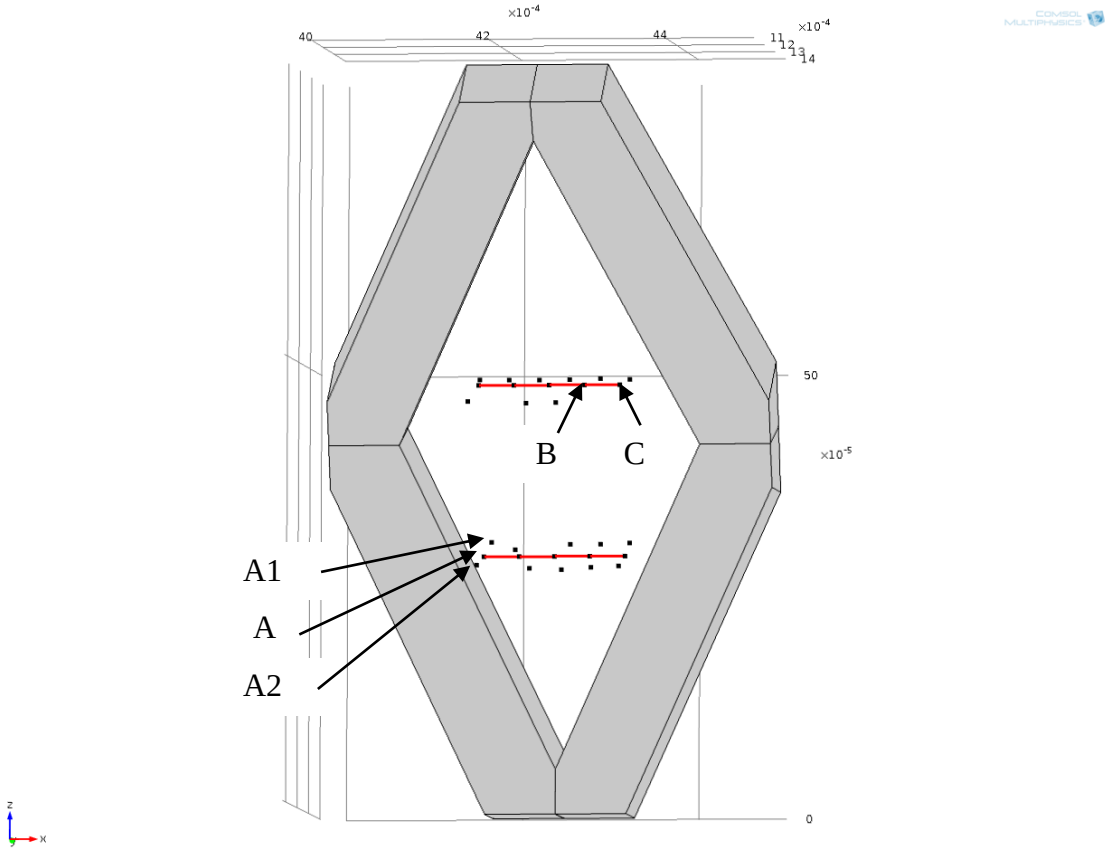

Figure 4.14: Location of the first and second minimum distances from the line segments of interest (in the first strut of the stent)

In Figure (4.14), the WSS is being computed on the line segments shown in red. These red line segments account for two out of the eight line segments shown in Figure (4.12). The points shown adjacent to the line segments were the closest nodal locations (nodes from mesh) where COMSOL computes the WSS. The values of WSS at these closest nodal points were used to approximate the values of WSS at the user-defined points on the line segment i.e., the WSS values from the two closest nodal points to the user-defined point (on the line segment) were extracted and their average was computed. This average was determined as the value of the WSS at the user-defined point on the line segment. For example, consider the points A, A1 and A2. A is a user-defined point with

coordinates A (0.004162, 0.001378188, 0.000293155). The coordinates of A1 and A2 are extracted from COMSOL and they are A1 (0.004153428273940, 0.001381155367075, 0.000283945219938) and A2 (0.004170723498887, 0.001377511235767, 0.000309267141546). A1 and A2 are the two closest nodal points to A where COMSOL computes the values of WSS. The WSS at A is approximated by taking the average of the WSS extracted at nodes A1 and A2. This procedure is repeated for all 40 points. It can be seen that for 80% of the points, the two closest nodal locations to the user-defined points (on the line segments) lie on either side of the line segment. However for 2 points, B and C, the closest locations lie on the same side of the line segment. It is assumed that the error introduced by this approximation is negligible because the distance between the user defined points and the nodal points varies in the order of 10^{-3}.

All the results in this section are extracted on mesh M8. Figures 4.15 (b), (c), (d) and (e), 4.16(b), (c),(d) and (e) present the variation of WSS with the x-coordinate for the FSI and no-FSI sub-studies at times t = 0.06 s, 0.15 s, 0.44 s, and 0.96 s. The data for these results were extracted at the edges and line segments shown in Figures 4.15(a) and 4.16(a). Figures 4.17(b), (c), (d) and (e) compared to the WSS values for the FSI and no-FSI sub-studies at the four different times listed above.

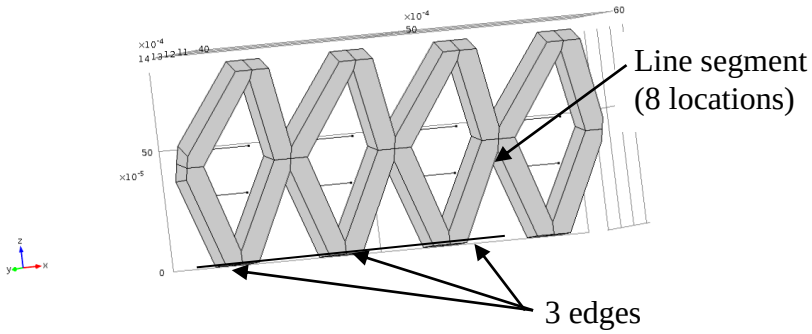

(a)

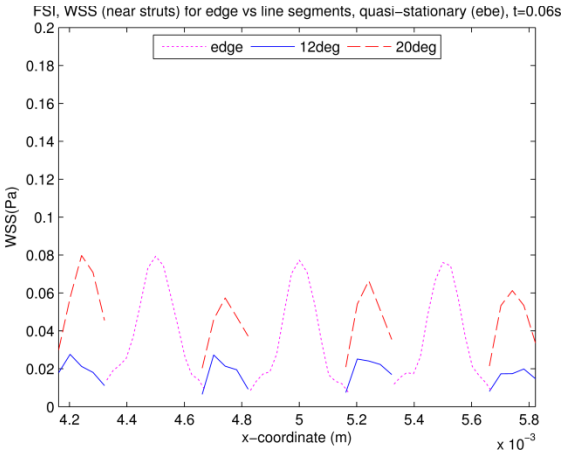

(b)WSS at t = 0.06 s

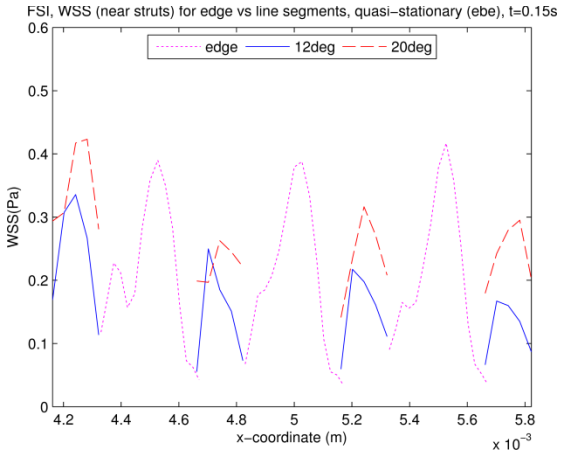

(c)WSS at t = 0.15 s

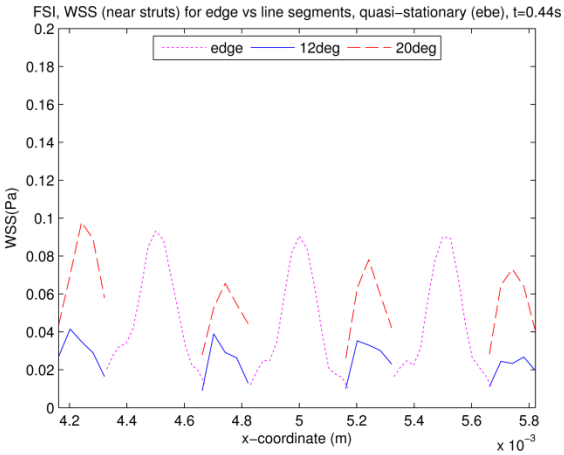

(d)WSS at t = 0.44 s

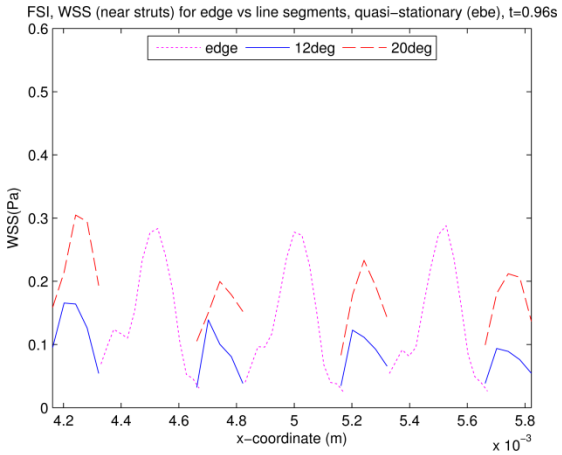

(e) WSS at t = 0.96 s

Figure 4.15: WSS at the edge vs line segments, FSI (near struts), quasi-stationary

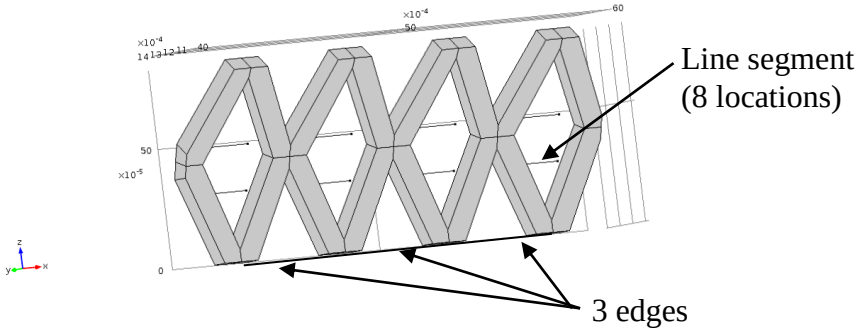

(a)

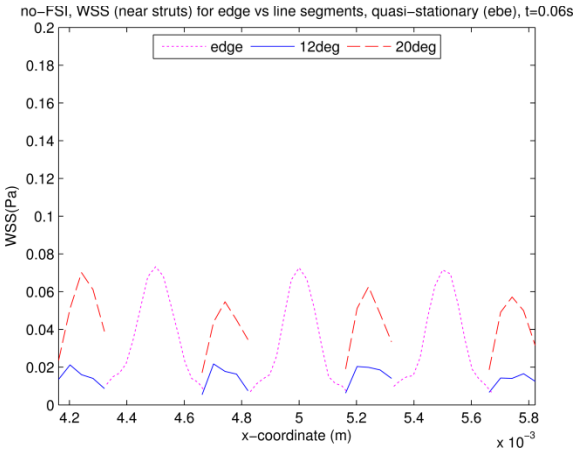

(b)WSS at t = 0.06 s

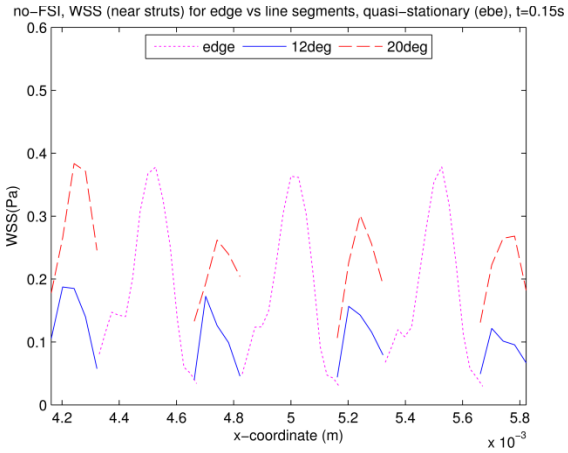

(c)WSS at t = 0.15 s

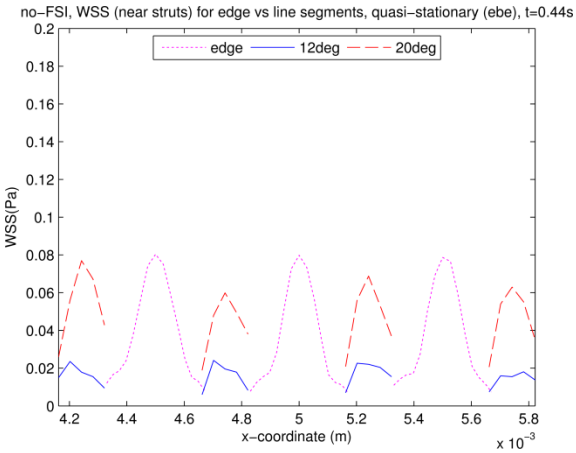

(d)WSS at t = 0.44 s

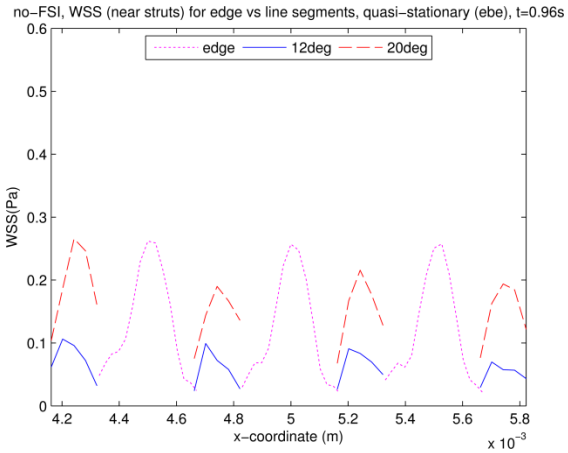

(e)WSS at t = 0.96 s

Figure 4.16: WSS at the edge vs line segments, no-FSI (near struts), quasi-stationary

The magnitude of the WSS for the FSI sub-study is comparable to that from the no-FSI sub-study at: (i) each of the 3 edges; and (ii) each of the line segments located at 20° (See Figure (4.17). The difference in the magnitude of WSS between the two sub-studies; however is relatively higher at each of the line segments located at 12°. It is important to note that the magnitude of WSS between the struts:

- is always less than 0.5Pa for both the FSI and no-FSI studies (See Figure (4.17)).
- for the FSI sub-study is almost always greater than the magnitude of WSS obtained from the no-FSI sub-study.

Below are some additional details that were observed from Figure 4.17.These details are not related directly to the stated objective of this study. In Figure 4.17(b), at the 20° line segments, the maximum magnitude of WSS inside the first strut is around 0.08Pa but the maximum magnitude of WSS inside the subsequent struts is about 0.06Pa, 0.07Pa, 0.06Pa. Similarly in Figure 4.17(e), the maximum magnitude of WSS inside each of the struts on the 12° line segments changes between 0.18 and 0.1Pa. This shows that the WSS does change with repetition of the local strut geometry. Some literature studies [3] use single stent elements. The above results indicate that it may be important to have more than one strut in a simulation. It can also be seen that: (1) inside the strut region, the WSS is lowest near the strut walls and it reaches a maximum value in between any two struts. (2) the shape of the WSS curves in between the struts is similar for the FSI and no-FSI sub-studies.

Also, note that the scale of WSS at time, t = 0.15 s and t = 0.96 s is three times the scale of WSS at t = 0.06 s and t = 0.44s, respectively. See Figure 4.17.

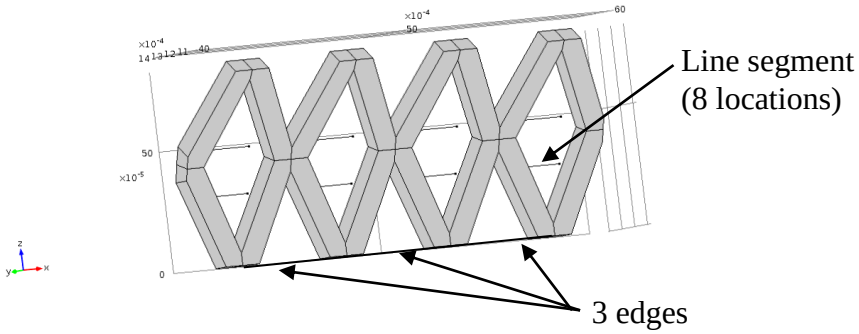

(a)

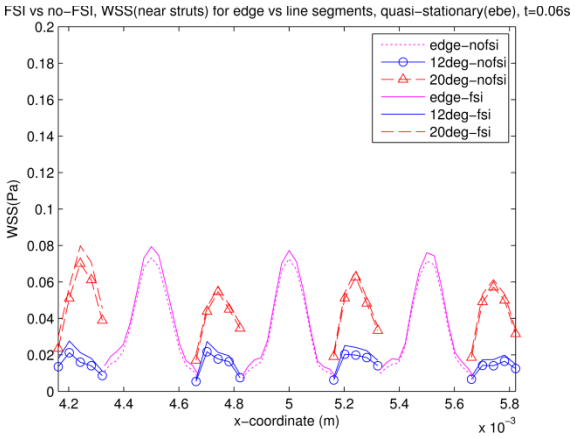

(b)WSS at t = 0.06 s

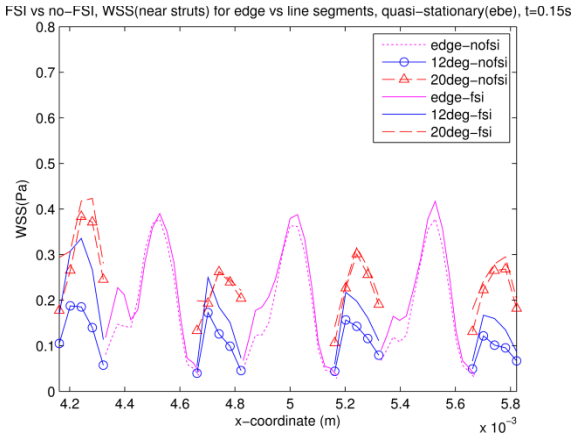

(c)WSS at t = 0.15 s

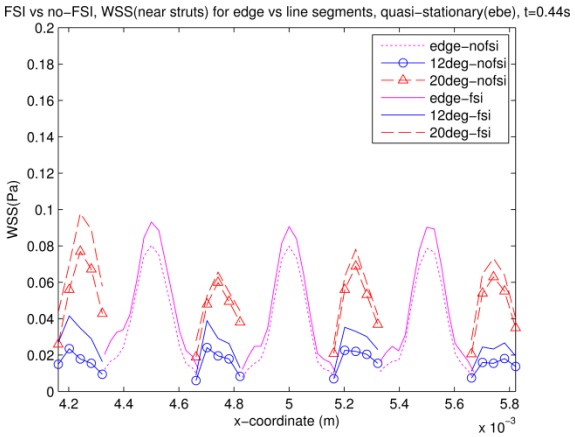

(d)WSS at t = 0.44 s

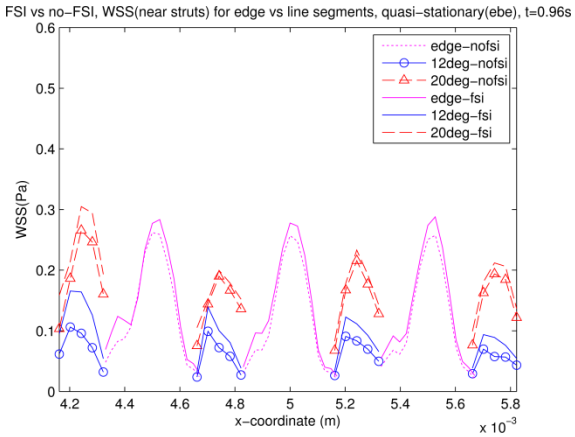

(e)WSS at t = 0.96 s

Figure 4.17: WSS, edge vs line segments, FSI vs no-FSI (near struts), quasi-stationary

Figures 4.18(a), (b), (c) and (d) which show the percentage error between the FSI and no-FSI sub-studies at the locations shown in Figure (4.12), were computed at t = 0.06 s, 0.15 s, 0.44 s, and 0.96 s. These figures demonstrate that, between the struts, the percentage error between the FSI and no-FSI sub-studies varies from 1% to 50% depending on the velocity and pressure magnitude (i.e. based on the time‘t’ when the results are evaluated).

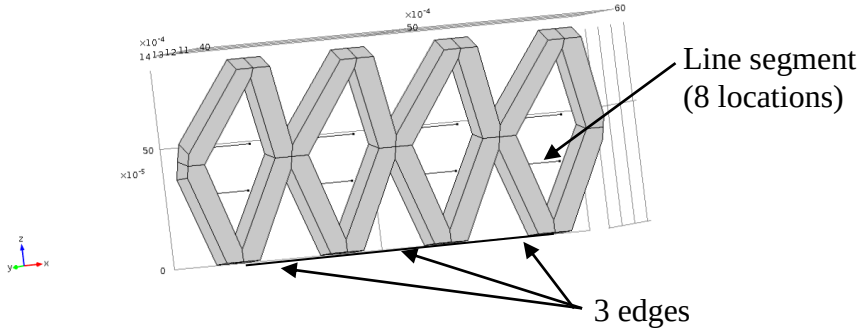

(a)

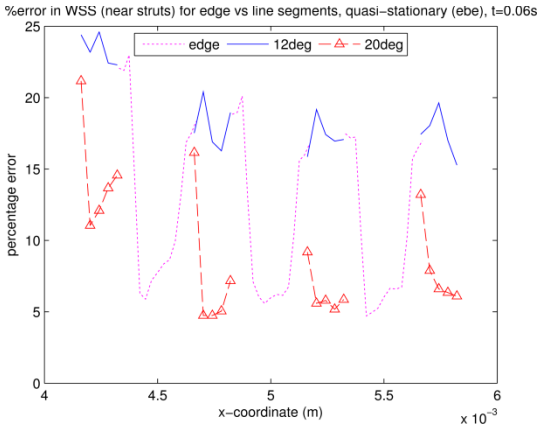

(b)Percentage error at t = 0.06 s

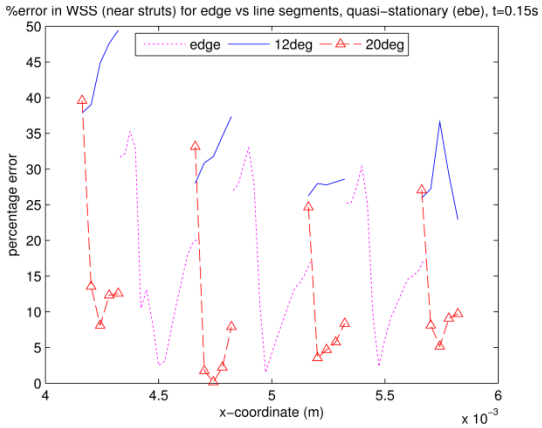

(c) Percentage error at t = 0.15 s

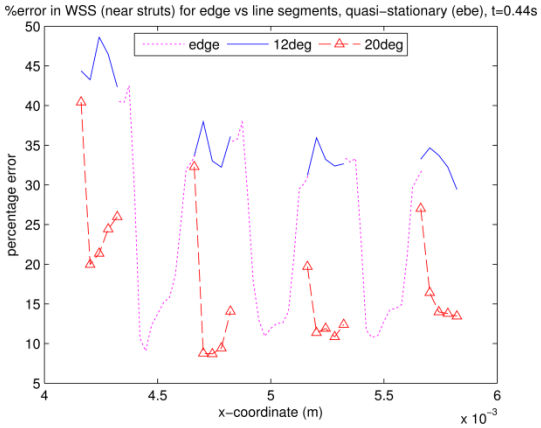

(d) Percentage error at t = 0.44 s

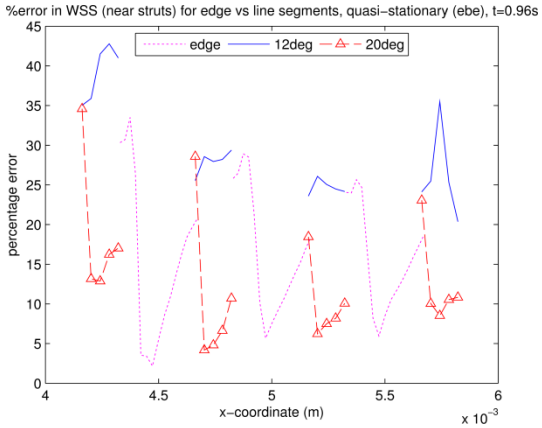

(e) Percentage error at t = 0.96 s

Figure 4.18: Percentage error in WSS between FSI and no-FSI, at the edge and line segments, quasi-stationary

4.4 Tolerance selection for the FSI and no-FSI sub-studies

This section presents the WSS results obtained by changing the tolerance criterion for convergence. The WSS (using mesh M8) was obtained for each sub-study for two different values of tolerance, which are 0.001 and 0.000001. These WSS values were computed at the edge shown in Figure (4.1).

In both the sub-studies, the percentage difference between the WSS for the two tolerances is negligible (for all the 16 times studied). The WSS values obtained for FSI sub-study with these two tolerances are shown in Figure 4.19(a) while the WSS values obtained for the no-FSI sub-study with the two tolerances are shown in Figure 4.19(b). Both these figures show a plot of the WSS as a function of x-coordinate at time, t = 0.44 s. It can be concluded from these figures that the WSS values are the same for both the tolerances. Hence, a tolerance criterion of 0.001 was used for all the analyses as it reduced the total run time to obtain a converged solution.

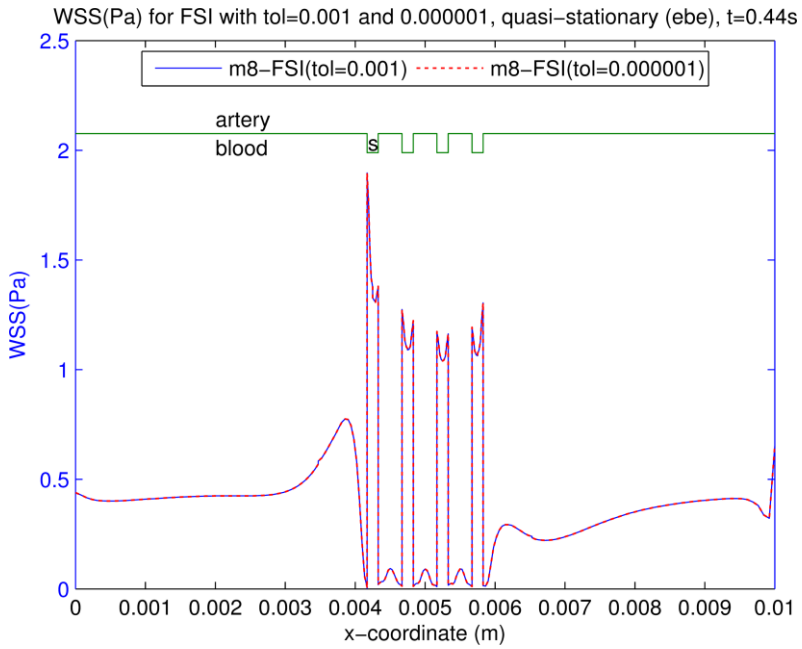

(a) FSI at t = 0.44 s

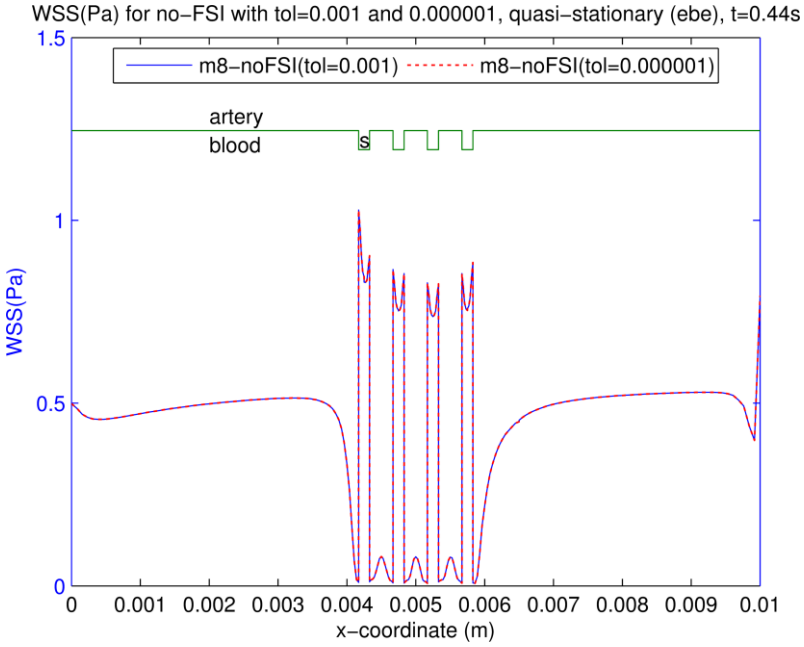

(b) no-FSI at t = 0.44 s

Figure 4.19: WSS values with tolerance of 0.001 and 0.000001 for the FSI and no-FSI sub-studies.

4.5 FSI and no-FSI sub-studies: Presence of duplicate nodes at a given location

The data plotted in Figure 4.20 (b) were extracted at the strut shown in Figure 4.20 (a). Figure 4.20(b) is a plot of the WSS as a function of the x-coordinate for mesh, M8, at time, t = 0.44 s, for the FSI sub-study. It shows that at each of the following nodes with coordinates A1 (0.00416999, 0.00133), B1 (0.004249994, 0.00133) and C1 (0.00417003, 0.00141), there exists a duplicate node represented by A2, B2, and C2. Even though the nodal coordinates are the same (duplicate), the values of WSS at the duplicate nodes were different. For example, at one such duplicate node with coordinates A1 (0.00416999, 0.00133), it can be seen that the WSS has two values which are 0.66Pa and 1.89 Pa. On further observation, multiple values of WSS at a given node have been observed at all the corner nodes in the geometric model. This happens because when COMSOL computes the dependent variables (eg: velocity, pressure), it assumes they are continuous. However, WSS is a derived value. It is not a dependent variable that is computed by COMSOL. It is computed from the solution by approximating the gradient of the velocity. So when the WSS values are computed at the corner nodes, the element on one side of the corner node produces one estimate for the WSS value and the element on the other side of the corner node produces a different value for the WSS. As a result, two different values of WSS are reported for a single location.

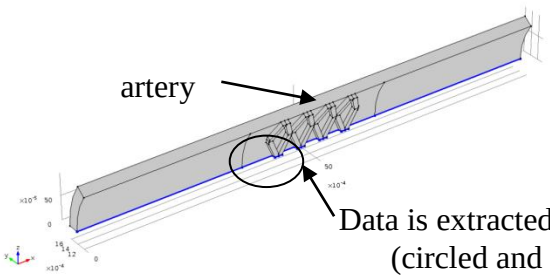

(a)

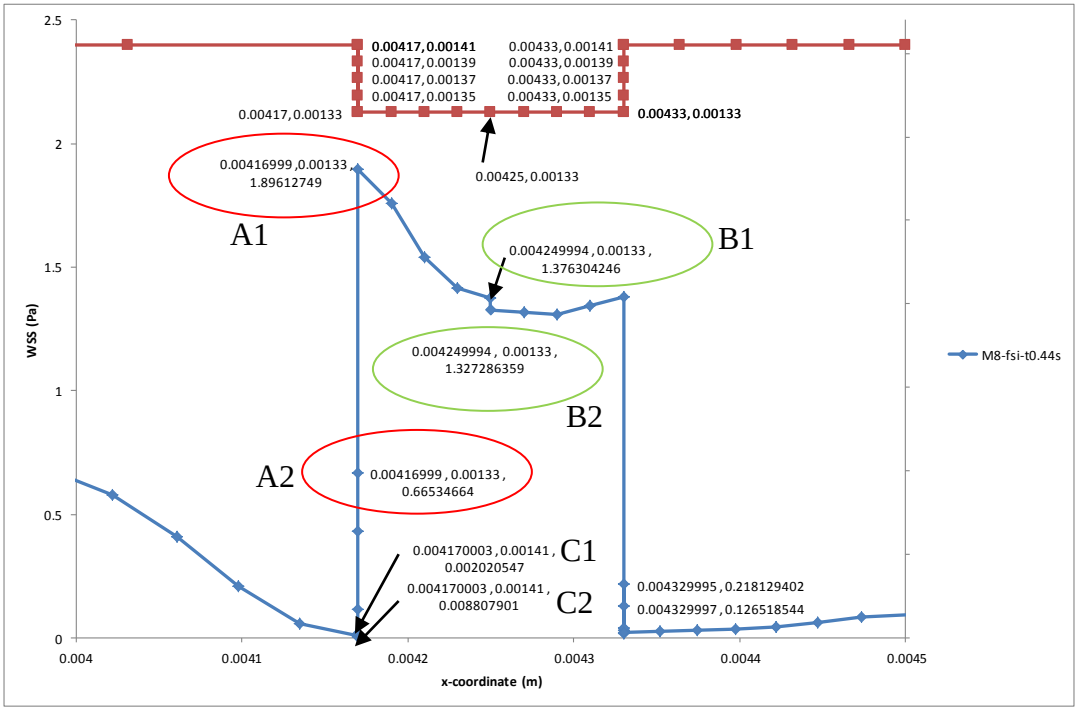

(b)

Figure 4.20: Presence of duplicate nodes in the analyses

Apart from the corner nodes, this duplicate node behavior was observed at the locations where two adjacent elements of a single strut join. Figure (4.21) helps in understanding the term ‘elements of strut’ and the ‘location where they join’. In Figure 4.20(b), coordinate (0.004249994, 0.00133) is one such location where two adjacent elements of a strut join. There are two values of WSS even at this node. Note, however, these values are very close to each other (1.37Pa and 1.32Pa) and the error introduced is negligible. These multiple values of WSS at a given node were observed even with the no-FSI sub-study. The conclusion of this study is that the values of WSS obtained at the corners are highly questionable.

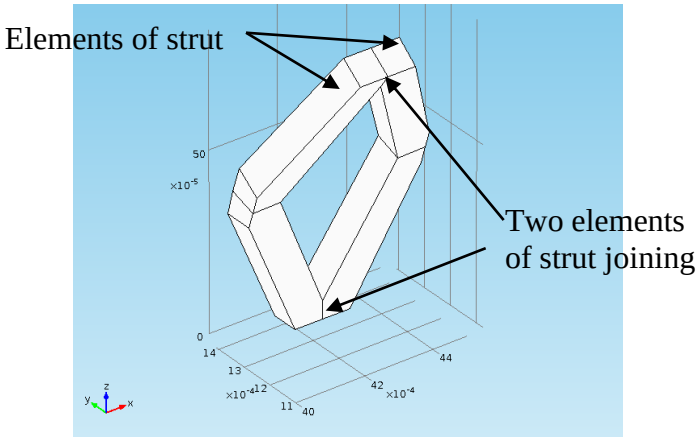

Figure 4.21: Elements of strut

4.6 FSI and no-FSI sub-studies: Surface plot of WSS

This section presents the WSS distribution at the fluid-solid interface for the FSI and no-FSI sub-studies. The results presented here are evaluated on mesh M8 at, t = 0.06, 0.15 s, 0.44 s, 0.96 s. This surface plot distribution of WSS is presented in Figures starting from

(4.22) to (4.25). In these figures, the (a)'s corresponds to the FSI sub-study and the (b)'s correspond to the no-FSI sub-study.

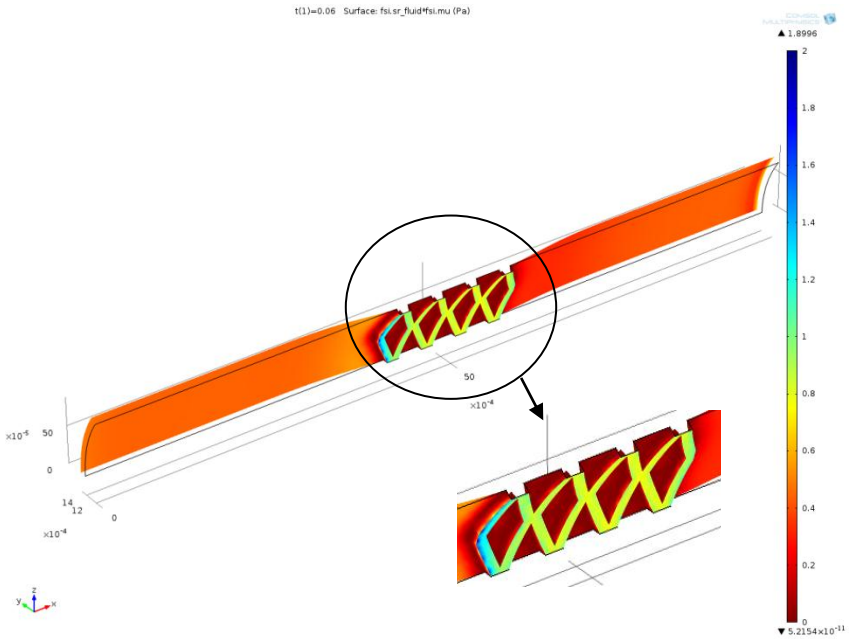

(a)WSS for FSI at t = 0.06 s

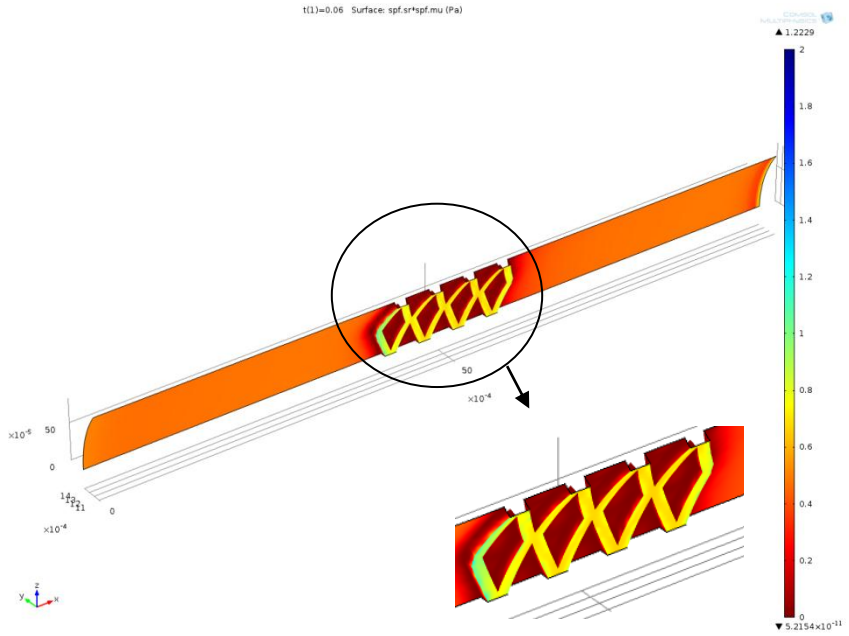

(b)WSS for no-FSI at t = 0.06 s

Figure 4.22: Surface plot of WSS, FSI and no-FSI, t = 0.06 s

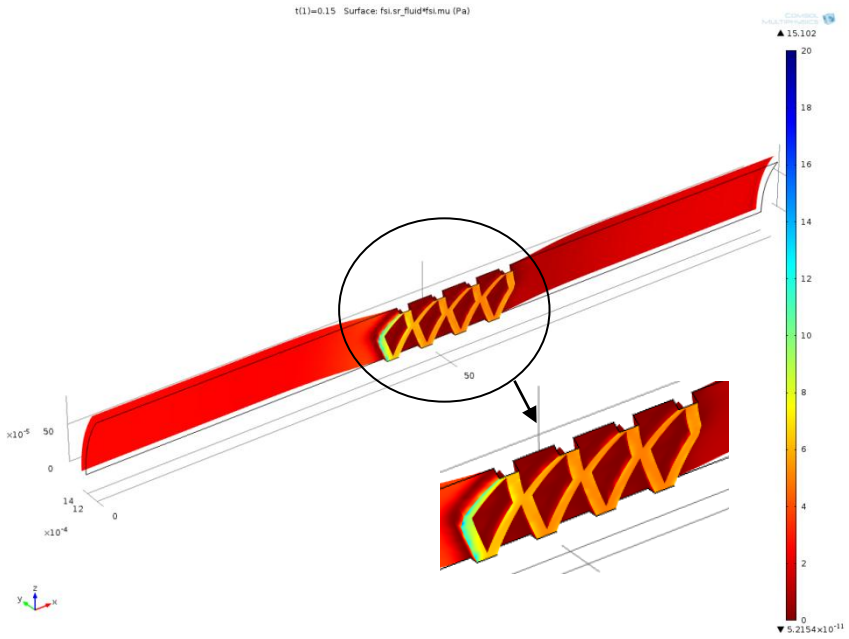

(a)WSS for FSI at t = 0.15 s

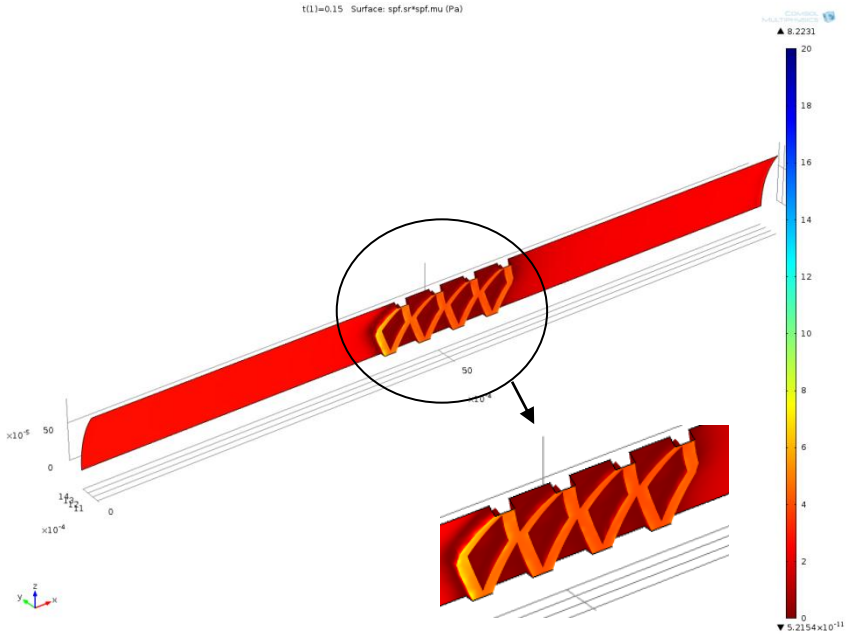

(b)WSS for no-FSI at t = 0.15 s

Figure 4.23: Surface plot of WSS, FSI and no-FSI, t = 0.15 s

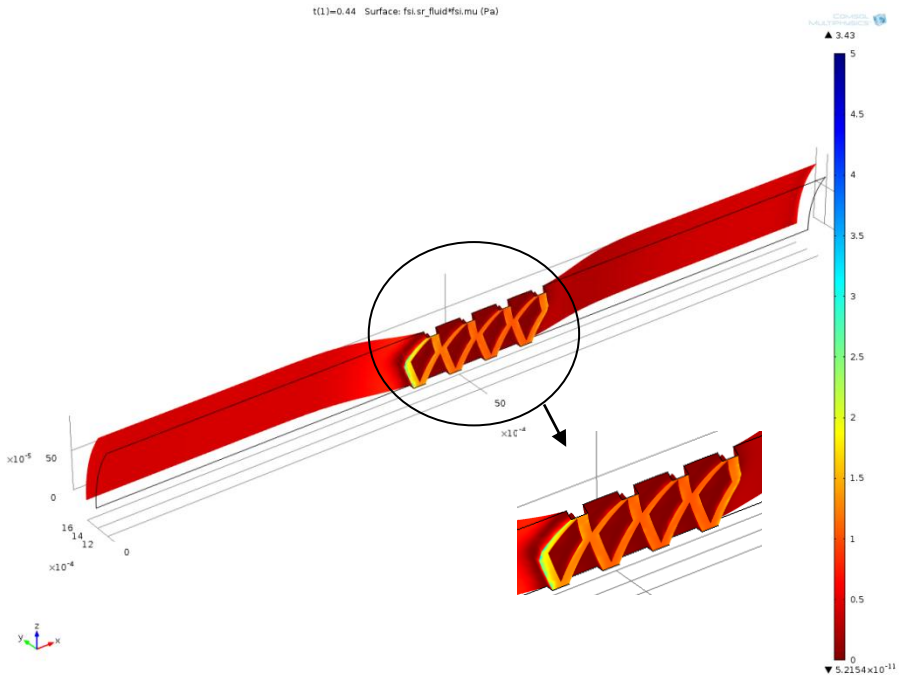

(a)WSS for FSI at t = 0.44 s

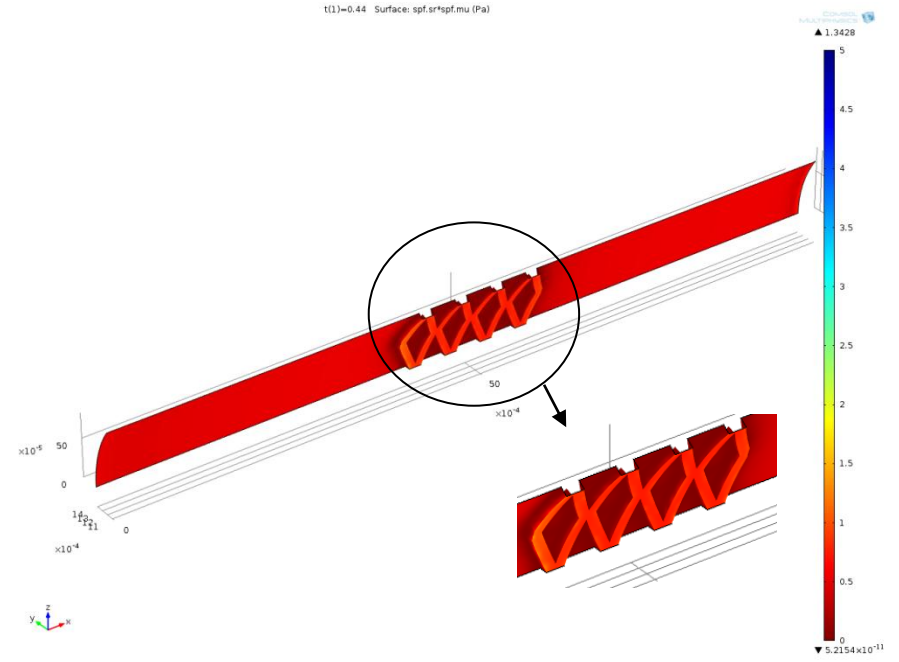

(b)WSS for no-FSI at t = 0.44 s

Figure 4.24: Surface plot of WSS, FSI and no-FSI, t = 0.44 s

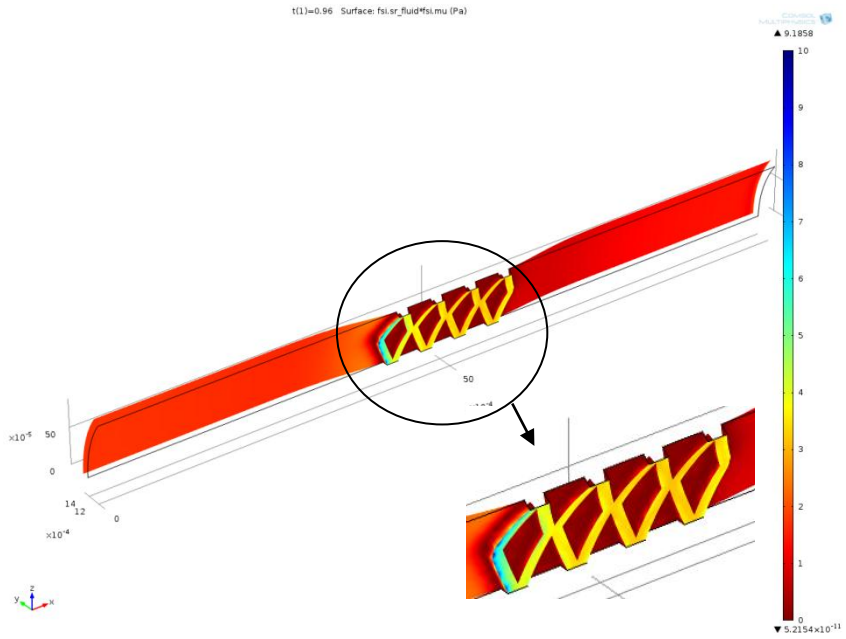

(a)WSS for FSI at t = 0.96 s

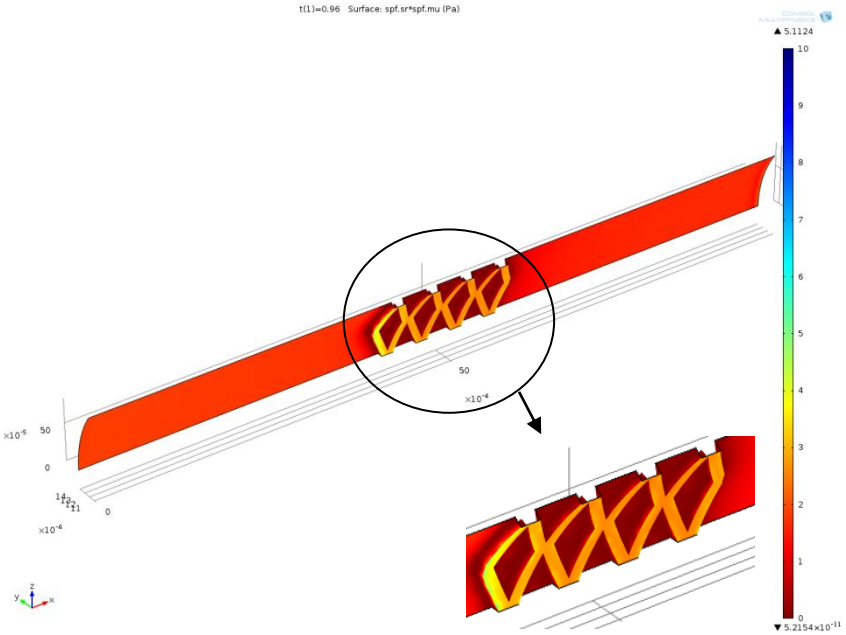

(b)WSS for no-FSI at t = 0.96 s

Figure 4.25: Surface plot of WSS, FSI and no-FSI, t = 0.96 s

The surface plots of the WSS show that the WSS between the struts is lower than the WSS at the proximal and distal ends (See Figures (4.22), (4.23), (4.24) and (4.25)). This is true for both the FSI and no-FSI sub-studies. Also, the magnitude of WSS between the struts is less than 0.5Pa for both the sub-studies at all the four times (t = 0.06s, 0.15 s, 0.44 s, 0.96 s).

Figure (4.26) shows the WSS distribution on the fluid-solid interface only in the locations where the magnitude of WSS < 0.5 Pa at times t = 0.06s, 0.15 s, 0.44 s, 0.96 s. This distribution is shown for both FSI and no-FSI sub-studies. In Figure (4.26), if there are regions on the fluid-solid interface where the magnitude of WSS > 0.5 Pa, then those regions are represented in white (color). At t = 0.06 s, both the FSI and no-FSI sub-studies show that in the region between the struts, the magnitude of WSS < 0.5 Pa. See Figure 4.26(a) and (b) The same figure also shows that the distal and proximal regions of the geometric model have WSS whose magnitude is < 0.5Pa. The presence of low WSS (< 0.5 Pa) in the proximal and distal regions of the geometric model, along with the location between the struts is also seen at, t = 0. 44 s (See Figure 4.26 (e) and (f)). At times, t = 0.15 s and t = 0.96 s, the low WSS (< 0.5 Pa) is observed only in the region between the struts (Figures 4.26 (c), (d), (g) and (h)).

Previous studies associate low WSS (< 0.5 Pa) with plaque accumulation and restenosis. Based on the information presented in Figure (4.26), it is likely that the current geometric model is predisposed to IT/plaque accumulation. Since, the current geometry is a user-defined geometry, this conclusion is not very critical. Given the conclusion about the geometry being predisposed to plaque accumulation, the current model can be proposed as a tool to predict regions of low WSS/IT/NIH.

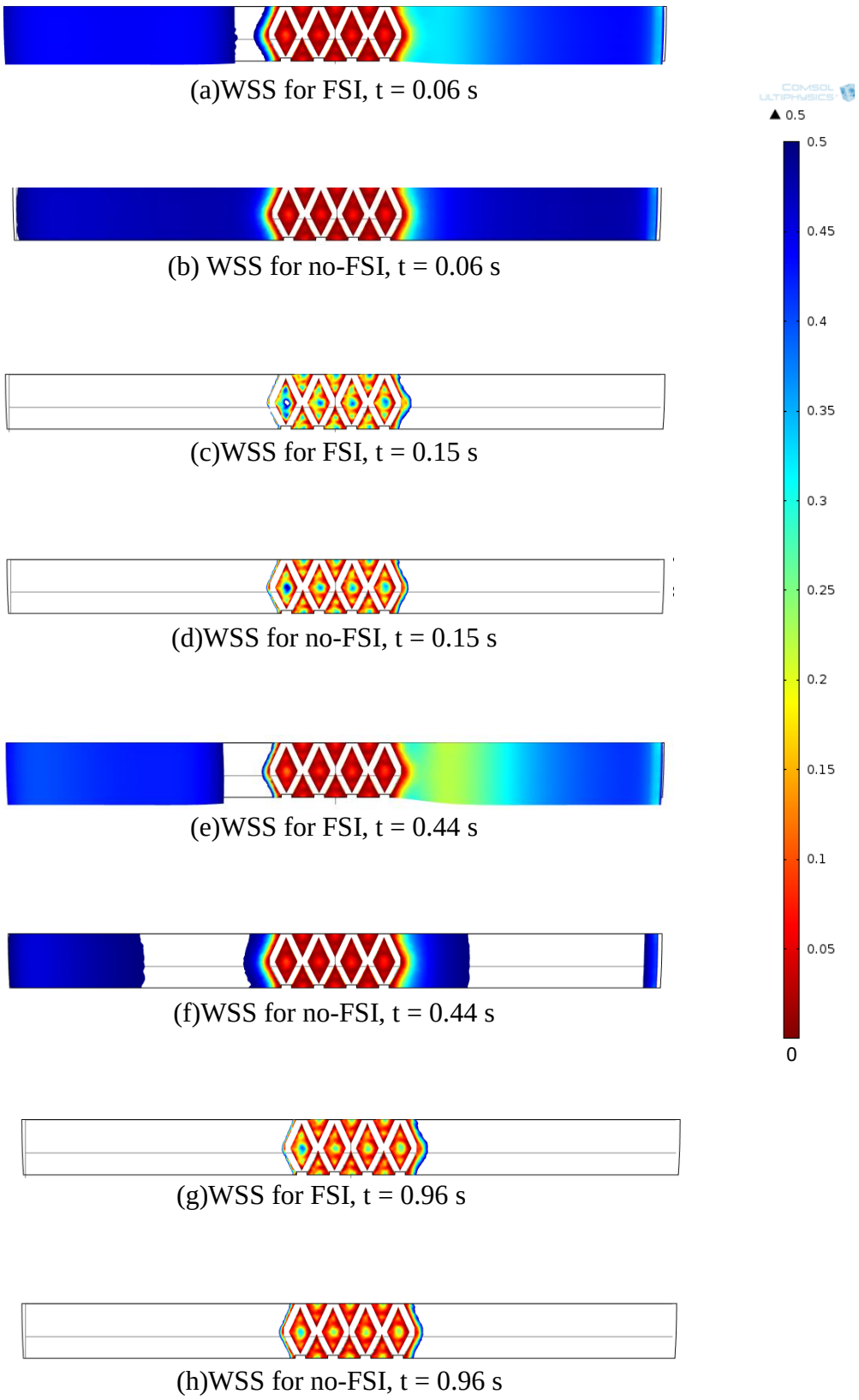

(a)WSS for FSI, t = 0.06 s

(b) WSS for no-FSI, t = 0.06 s

(c)WSS for FSI, t = 0.15 s

(d)WSS for no-FSI, t = 0.15 s

(e)WSS for FSI, t = 0.44 s

(f)WSS for no-FSI, t = 0.44 s

(g)WSS for FSI, t = 0.96 s

(h)WSS for no-FSI, t = 0.96 s

Figure 4.26: WSS distribution on fluid-solid interface: locations where WSS < 0.5 Pa

4.7 FSI and no-FSI sub-study: Velocity distribution and total displacement

The volumetric plots of the velocity distribution in the flow field and the total displacement in the arterial wall are presented in this section. These results are obtained from mesh M8 at times t = 0.06 s, 0.15 s, 0.44 s and 0.96 s for both the FSI and no-FSI sub-studies. Figures 4.27(a) and (b), 4.28(a) and (b), 4.29(a) and (b), 4.30(a) and (b) show the volumetric plots for the FSI and no-FSI sub-studies at the above mentioned times.

In the above mentioned figures, the results corresponding to the FSI sub-study show that the location of maximum velocity is always below the strut region. The location of the maximum velocity in the no-FSI sub-study varies between the inlet face and the region below the strut. Figure 4.29(a) shows that the maximum displacement (1.99e-4 m) in the arterial wall occurs at t = 0. 44 s.

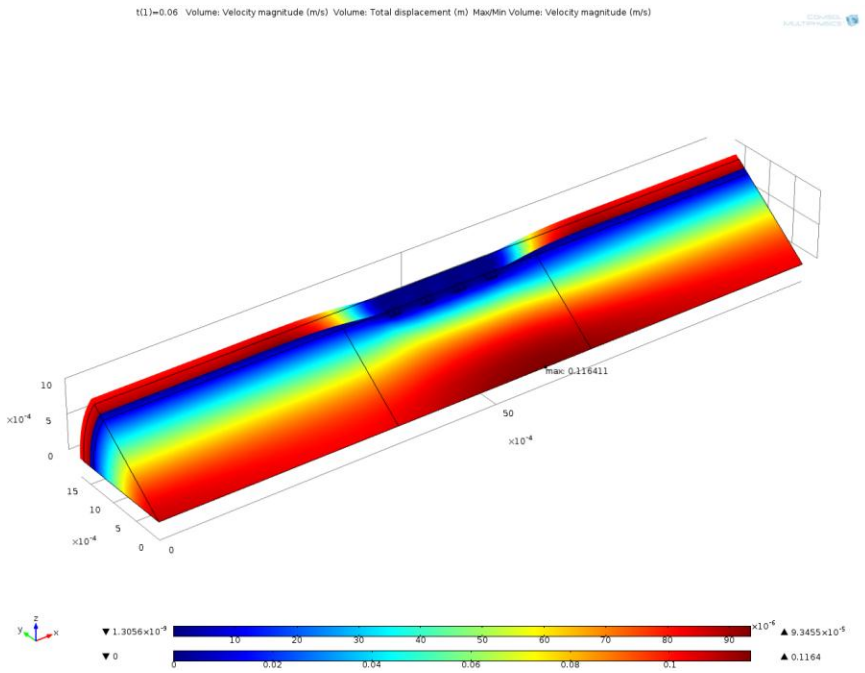

(a)Velocity distribution and total displacement of arterial wall for FSI at t = 0.06 s

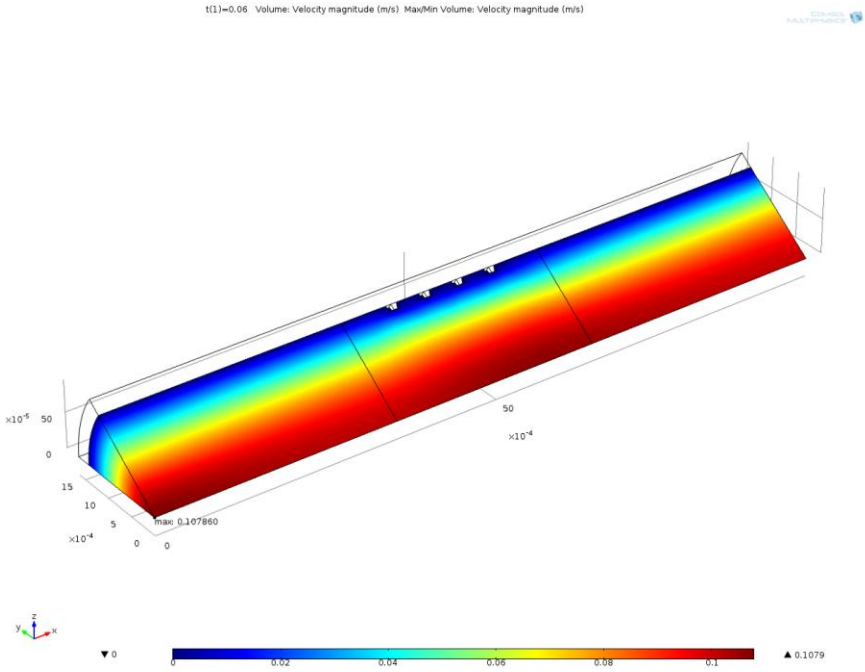

(b)Velocity distribution for no-FSI at t = 0.06 s

Figure 4.27: Volumetric plot, FSI and no-FSI, t = 0.06 s

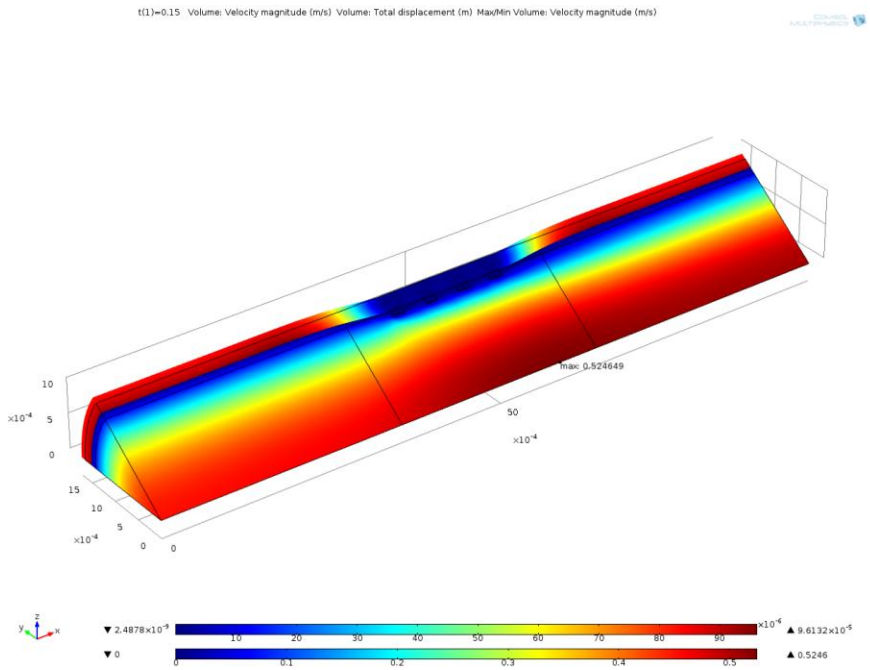

(a)Velocity distribution and total displacement of arterial wall for FSI at t = 0.15 s

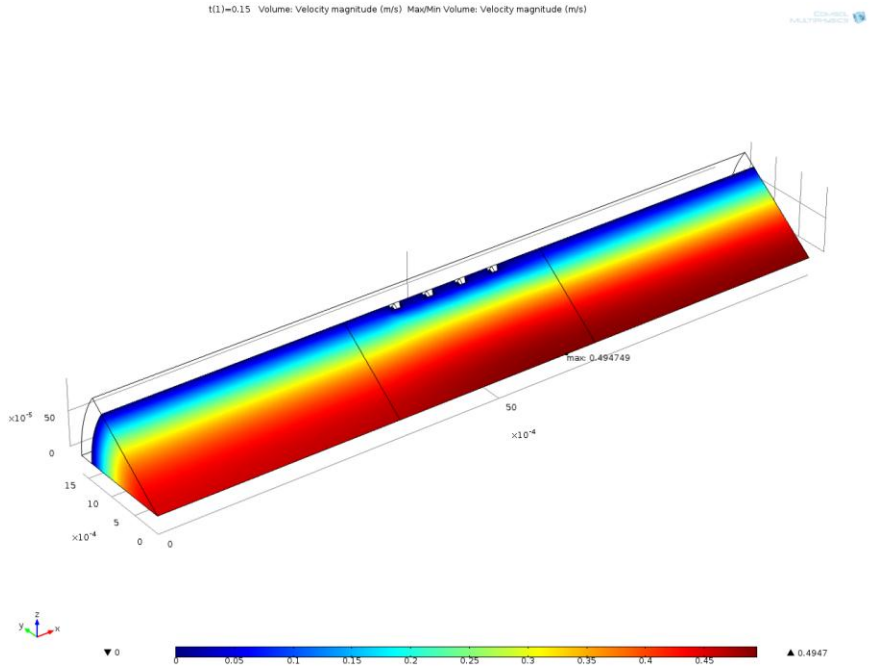

(b)Velocity distribution for no-FSI at t = 0.15 s

Figure 4.28: Volumetric plot, FSI and no-FSI, t = 0.15 s

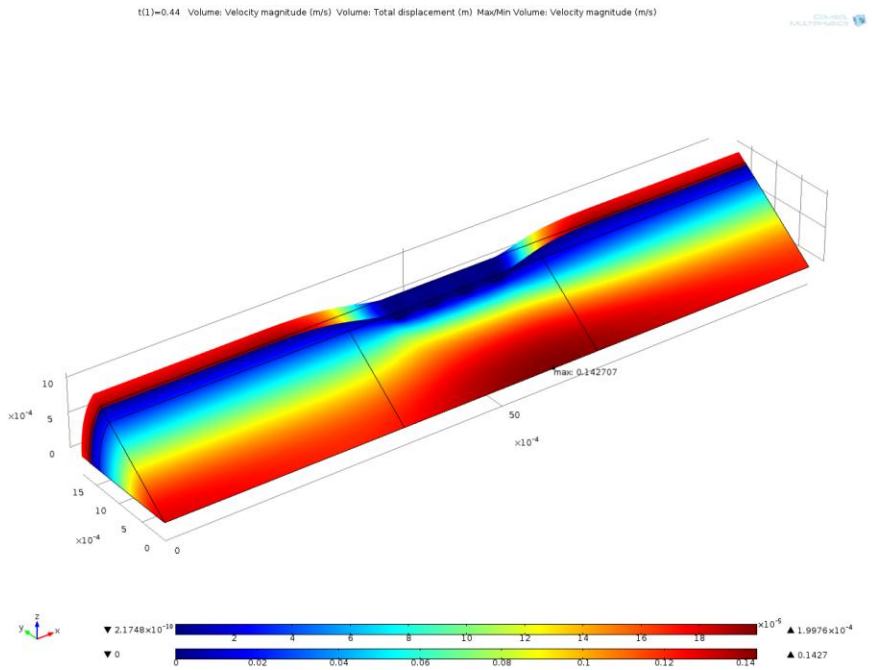

(b)Velocity distribution and total displacement of arterial wall for FSI at t = 0.44 s

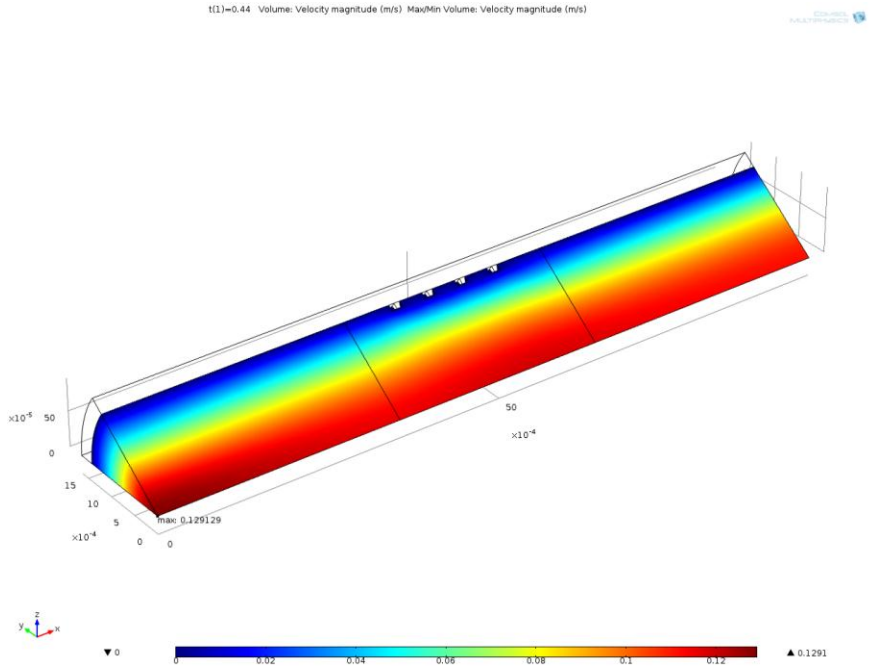

(b)Velocity distribution for no-FSI at t = 0.44 s

Figure 4.29: Volumetric plot, FSI and no-FSI, t = 0.44 s

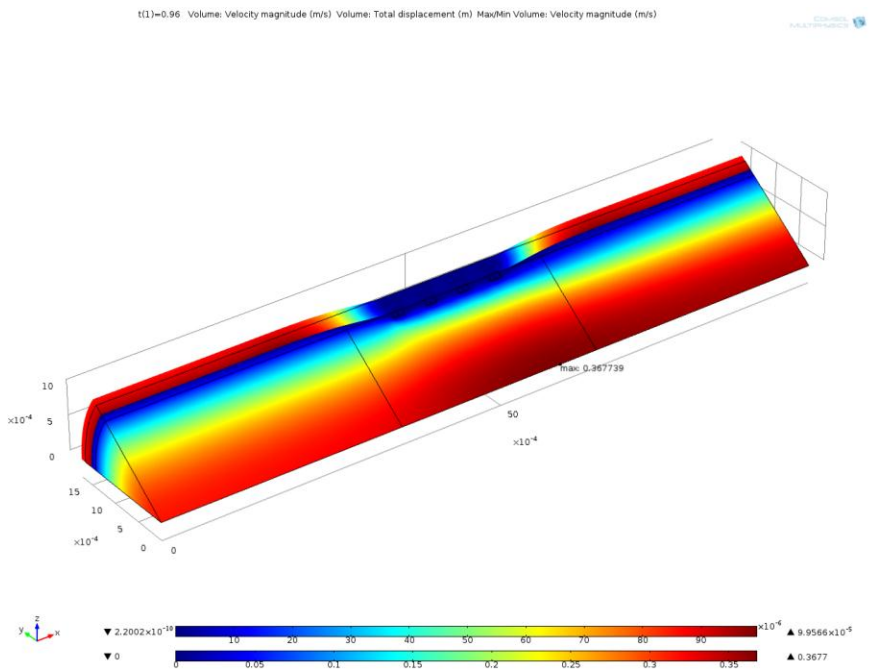

(a)Velocity distribution and total displacement of arterial wall for FSI at t = 0.96 s

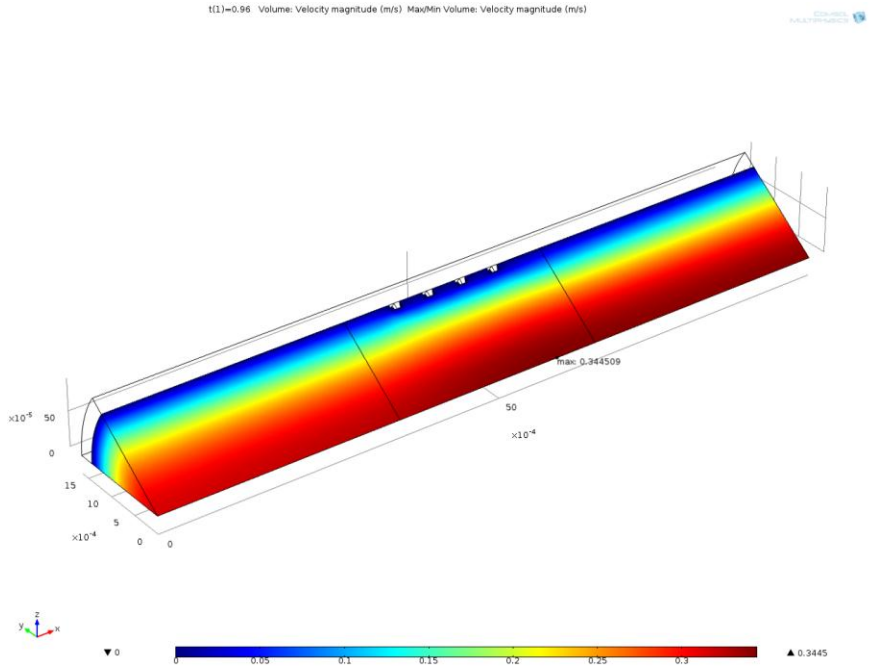

(b)Velocity distribution for no-FSI at t = 0.96 s

Figure 4.30: Volumetric plot, FSI and no-FSI, t = 0.96 s

4.8 FSI and no-FSI sub-studies: Recirculation regions

Figures 4.33 (a) and (b) show the streamlines on the surface circled in Figure (4.31) while Figure 4.34 (a) and (b) show the streamlines on the surface highlighted in Figure (4.32). All the streamline plots are evaluated at time, t = 0.44 s. The surface shown in Figure (4.32) is at an angle of 12° to the horizontal. All of these streamline plots are plotted using the data evaluated on mesh M8.The results shown in Figures 4.33 (a), 4.34(a) and 4.33(b), 4.34(b) correspond to the FSI and no-FSI sub-studies, respectively.

The streamline plots are shown to highlight the recirculation regions near the struts. These regions indicate flow reversal/change of direction in flow. This flow feature was not revealed in the preceding displays of simulation results. In a 1D flow, the WSS values are negative when the flow reverses (recirculation region). However, the flow in the current study is three dimensional (3D) and the magnitude of WSS (which is a tensor in 3D) is computed using Equation(4.1). The magnitude of shear stress in Equation (4.1) is always positive. In such a scenario, the recirculation regions can be located by plotting the streamlines of the velocity field or by computing the oscillatory shear index (OSI). The expression used to compute OSI is time-dependent (See Equation (4.5)). Hence, it can only be computed for time-dependent studies or for stationary studies that are carried out at different times (like the current study).

Figures (4.33) and (4.34) are plotted on two different surfaces. Hence the location of recirculation regions is different in these set of figures. Also, when compared to Figure 4.33(b), the region with high-velocity (represented by red color in the figures) extends to a region much closer to the stents in Figure 4.33(a). The same behavior is observed in Figures 4.34 (a) and (b). This implies that the velocity gradient in the stent region will be

higher in Figures 4.33(a) and 4.34(a) (both these figures correspond to the FSI sub-study). Consequently, the WSS in the stent region also will be high. This result agrees with the results obtained from WSS evaluation (See Figure 4.9). Figure (4.9) shows that the magnitude of WSS from the FSI sub-study is higher on the stents when compared to the WSS magnitude from the no-FSI sub-study.

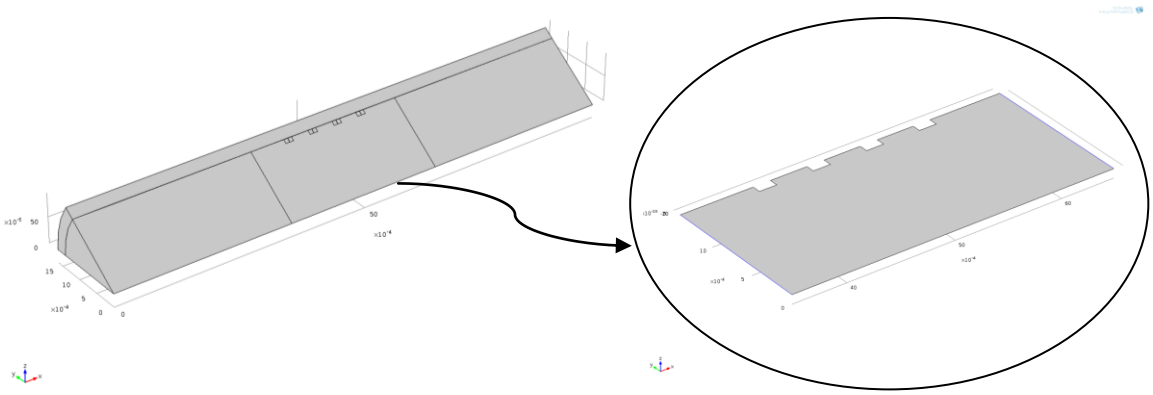

Figure 4.31: Surface used for the streamline plot

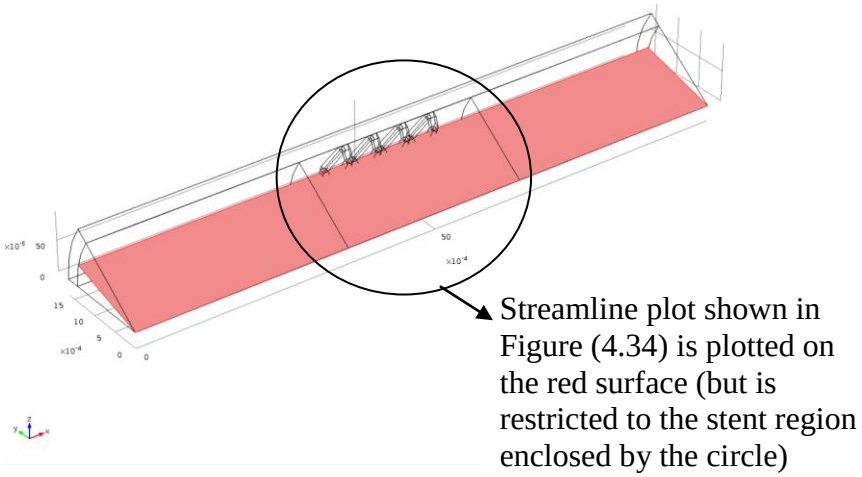

Figure 4.32: Inclined surface used for the streamline plot

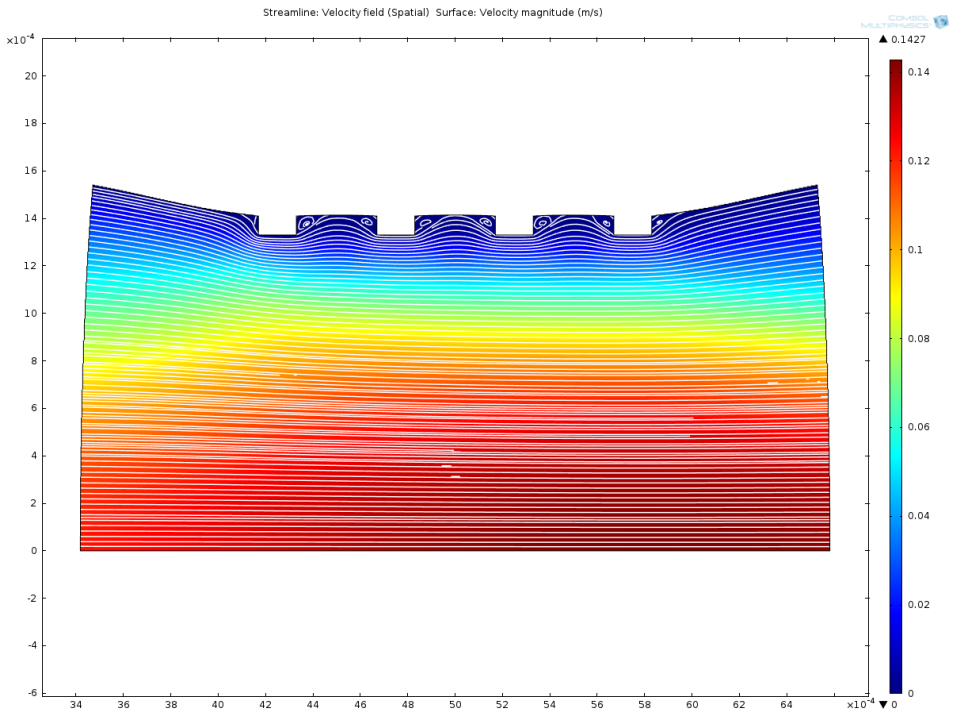

(a) FSI

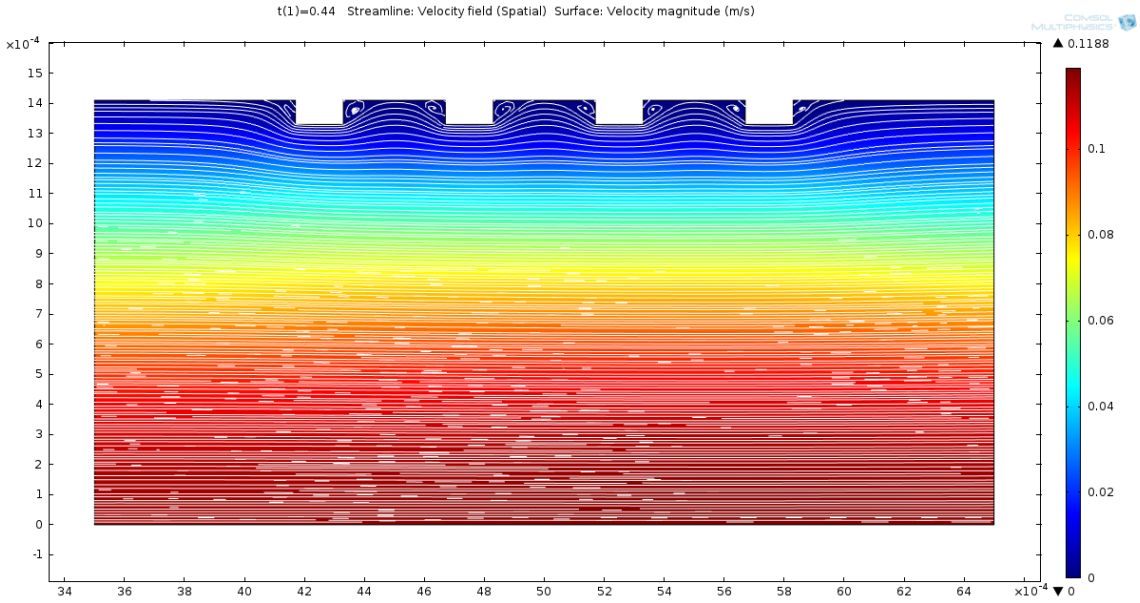

(b) no-FSI

Figure 4.33: Velocity field streamlines on surface shown in Figure (4.31), t = 0.44 s

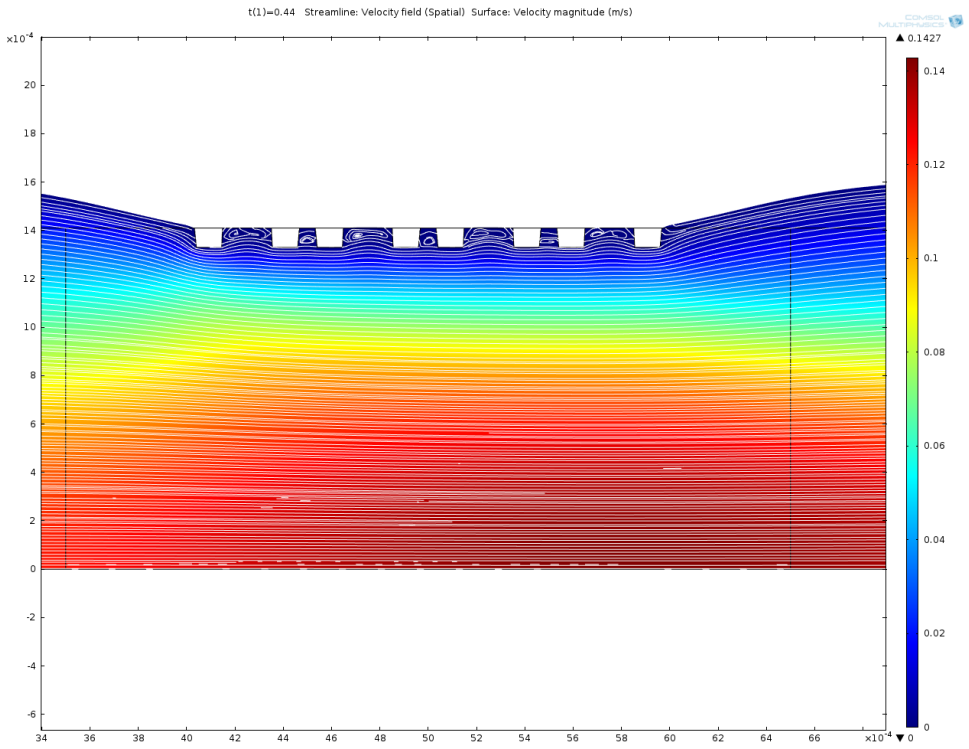

(a)FSI

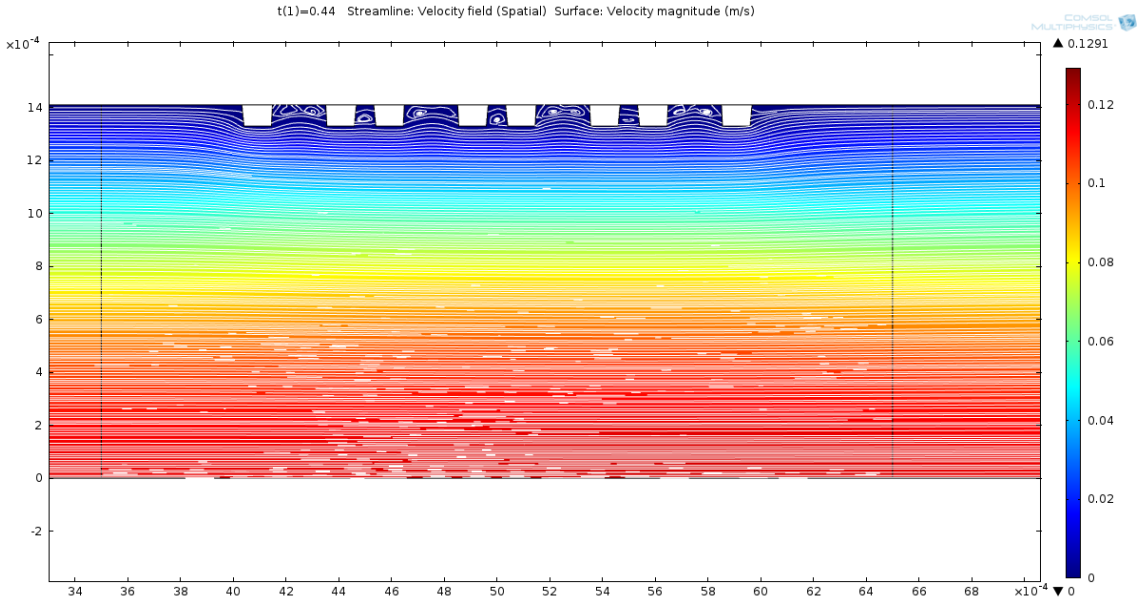

(b) no-FSI

Figure 4.34: Velocity field streamlines on surface shown in Figure (4.32), t = 0.44 s

4.9 FSI and no-FSI sub-studies: TAWSS and OSI

This section compares the magnitude and behavior of TAWSS and OSI for the FSI and no-FSI sub-studies. Figure 4.35(a) shows the TAWSS evaluated along the entire edge shown in Figure (4.1) and Figure 4.35(b) shows the TAWSS near the strut region. . Similarly, Figure 4.36(a) shows the OSI on the entire edge and the Figure 4.36(b) shows the OSI near the strut region. The TAWSS and the OSI plots are plotted using the data extracted at all the 15 times (on meshM8).

From the TAWSS distribution, it can be concluded that the influence of FSI is more prominent in the region of the stent and in the distal region of the geometric model. Torri et al [91] concluded that the influence of FSI on TAWSS and OSI are insignificant in a stenosed coronary artery. As mentioned in Chapter 2, Section 2.3, the OSI is high when the direction of WSS changes. The magnitude of OSI is about 0.1 in the stent region (See Figure (4.36)). This indicates that there is some change in the direction of WSS near the stent region but it is not significant enough to cause an unsteady and oscillatory flow. In the proximal and distal regions, the OSI is close to zero. Figure (4.36) shows that the magnitude of OSI for the FSI and no-FSI sub-studies is only minimally different.

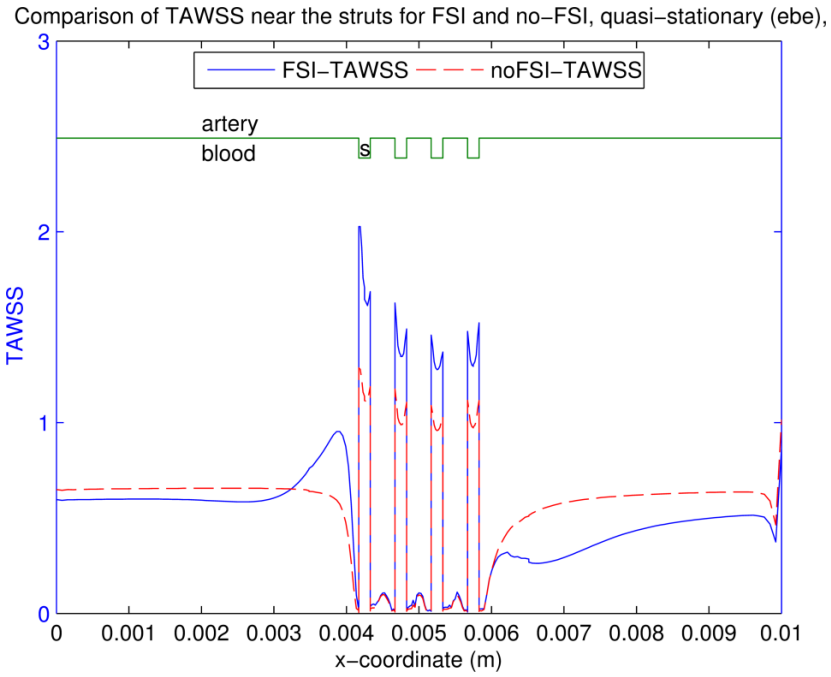

(a)TAWSS on the entire edge

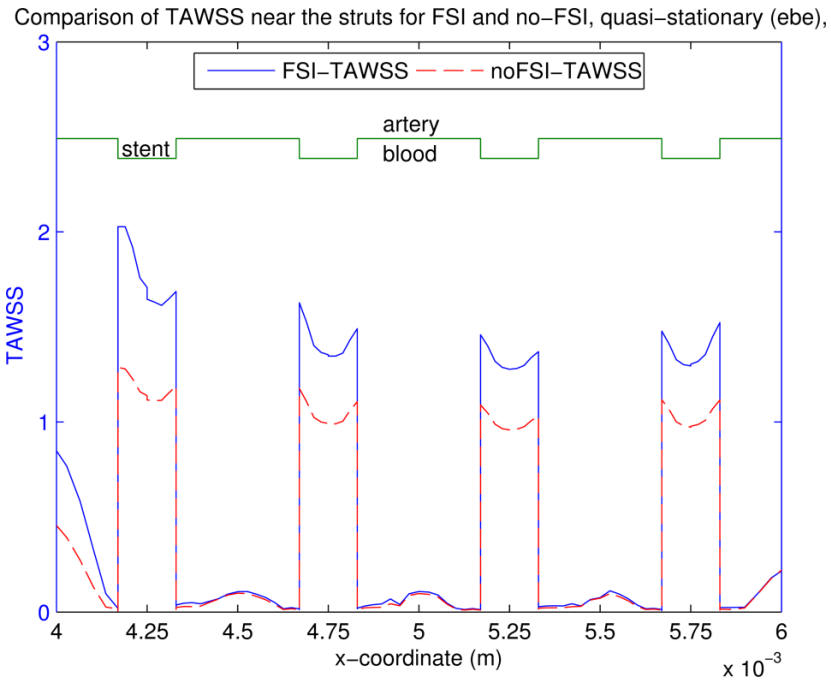

(b)TAWSS near the struts

Figure 4.35: Comparison of TAWSS for FSI vs no-FSI, quasi-stationary

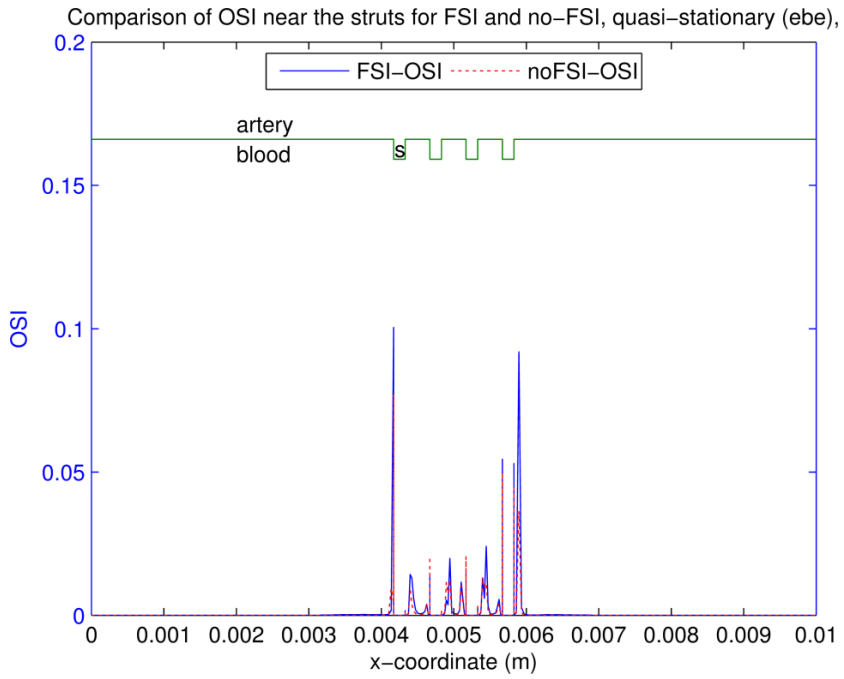

(a)OSI on the entire edge

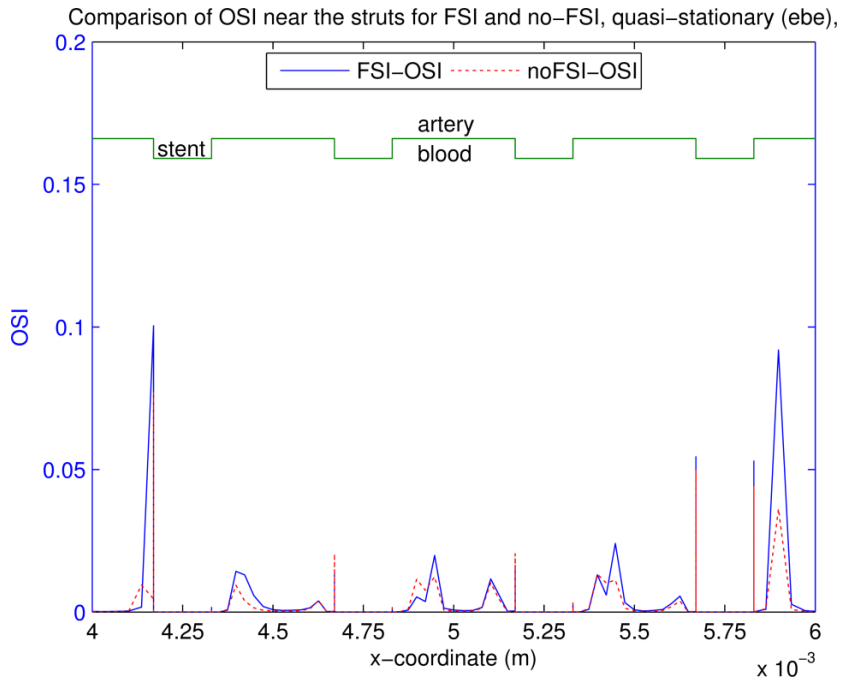

(b)OSI near the struts

Figure 4.36: Comparison of OSI for FSI and no-FSI, quasi-stationary

4.10 Comparison to other published results

In general, a finite element model is validated by building a physical model of the simulation, performing the necessary experiments, and then comparing the results of the finite element model with those obtained from the experiment. However, considering that the current study involves coronary arteries and the resources are not available for an experimental study, it is not possible to follow this process. In such situations, confidence in the results of the finite element model can still be obtained by comparing them with results from a published clinical study or by comparing them with results obtained from other finite element studies.

In the current study, the magnitude of WSS between the struts is always lower than 0.5 Pa. See Chapter 4, Sections 4.1, 4.2, 4.3, and 4.6 for these results. This indicates that the likelihood of restenosis is high in this region. The relationship between restenosis and magnitude of WSS is described in Chapter 1. Gay and Zhang [25] carried out a finite element study (2D rigid wall) using a similar stent design. The results from their study indicate that the stented region poses higher risk for restenosis. Also, the profile of WSS between the struts in the study carried out by Gay and Zhang [25] is similar to the profile of WSS between the struts in the current study. Hence, the current study is in agreement with the study carried out by Gay and Zhang

Figure(4.11) shows that the percentage error in the WSS magnitude between the FSI and no FSI sub-studies is higher within the stent and in the distal region of the geometric model when compared with the proximal region of the geometric model. This result partially agrees with the results of Torii et al [91] and Zeng et al [128]. Both these papers state that the influence of FSI is more pronounced in the distal region of the artery.

4.11 Limitations of the current study

The current study uses linear order elements due to limitations on the available computational resources. The mesh convergence studies (Chapter 4, Sections 4.1.1 and 4.1.2) show that the current solutions are mesh independent. However, reconfirming the mesh convergence by using second order elements would establish the accuracy of the current study in a definite manner.

The current study used a quasi-steady simulation: stationary equations solved with a sequence of time-dependent values for the boundary conditions to approximate a truly transient analysis. This assumption is to be verified by running a time-dependent analysis with the current model. Also, it is important to re-evaluate the OSI using the time-dependent analysis. See Chapter 2, Section 2.1.1 for a previous study carried out by Mates et al. that discusses quasi-steady analysis.

Coronary arteries undergo motion because they are attached to the myocardium and this motion may be related to the susceptibility to atherosclerosis [17]. The current study ignores this movement of the coronary artery. Wentzel et al [95] concludes that the shear rates are only minimally influenced due to the movement of coronary arteries provided the frequency of movement is ≤ 1 Hz. Torii et al [91] state that as long as the parameter of interest is TAWSS, this motion is not important but it may undervalue other hemodynamic parameters. Hence, the decision of whether to include the movement of the coronary artery is dependent on the objective of the study and the parameter of interest. Since the frequency of the current study is 1Hz, the movement of the artery may not be relevant to the current study. This, however, can only be confirmed by modeling the movement of coronary artery.

In Chapter 4, Section 4.5, it is acknowledged that the values of WSS obtained at the duplicate nodes are highly questionable. This is because COMSOL which is a finite element method, assumes continuity of dependent variables viz., velocity and pressure for the fluid domain. On the other hand, WSS is evaluated as the gradient of the velocity. Between any two elements (of the mesh), COMSOL does not enforce continuity on the gradient of a velocity.

It is assumed that the arterial wall is elastic. Chapter 1 lists some literature studies that discuss different non-linear material models that can be used to represent the arterial wall. In order to increase the accuracy of the arterial wall model, the representation should reflect that it is truly incompressible ($\upsilon = 0.5$), and it should consider tissue anisotropy, residual stresses, heterogeneity, and the layered structure of the artery. Including any of these features in the simulation will almost certainly increase the computational resources required for the simulation.

The artery is assumed to be straight with a circular cross-section. Literature shows that curvature plays an important role for RCA hemodynamics [70]. Myers et al [70] also show that it is important to use patient-specific data. The current study does not use patient-specific geometry as it was not available.

The current study is carried out in a healthy, stented, coronary artery and there is no material model representing the plaque or the cardiac muscle. Modeling the cardiac muscle may reduce the extent of arterial wall displacement and increase the chances of convergence when representing the artery with a hyperelastic material model. Unfortunately, this could not be evaluated due to restricted computational resources. Most of the literature suggests that the flow in coronary arteries is laminar but

considering the extent to which plaque blocks the artery (not necessarily coronary artery), it is possible for the flow to become turbulent [43].

The current study does not model the balloon expansion of the stent. Hence, it does not account for the change in arterial wall stresses induced by the vascular injury from the expansion of the stent-balloon assembly. Chapter 2, Section 2.5 lists some more parameters, which when included in a computational model of the coronary artery, are likely to increase the accuracy of the model. Depending on the objective of the study, however, including all of these parameters may or may not be essential.

Literature reports that there are some additional boundary conditions which, when not included, are likely to influence the results of an FSI study. Two of these are recovering zero-pressure-state arterial geometry and, accounting for wave propagation in flexible vessels.

Vavourakis et al. [93] modeled coupled FSI hemodynamics by recovering the zero-pressure-state corrected arterial geometry. Based on Bols et al. [5], recovering zero-pressure-state geometry means including initial stresses that are present in the arterial wall when the MRI/CT images are captured to record the patient-specific arterial geometry. Vavourakis et al. analyzed a patient-specific, healthy carotid bifurcation both by recovering and by not recovering the zero-pressure state. The outcome of the study indicates that using the image-based arterial geometry without recovering the zero-pressure geometry results in unrealistic wall deformation and underestimation of the WSS.

Formaggia et al. [20] accounts for the wave propagation phenomenon in flexible blood vessels by coupling the 2D or 3D fluid-structure flow problem with a reduced 1D

flow model. The coupling represents the interaction of a carotid bifurcation with the rest of the cardiovascular system.

5. CONCLUSIONS

The following conclusions are drawn by analyzing the data extracted from the computational simulations presented in the preceding chapters.

1. At each of the four times during the cycle of the prescribed periodic flow boundary conditions that were examined in detail, t = 0.06 s, t = 0.15 s, 0.44 s and 0.96 s, the average percentage error in WSS incurred by omission of the FSI model varies between :
    a. 10-20% in the proximal region of the geometric model
    b. 17-55% in the distal region of the geometric model
    c. 10-35% in the region between the struts
    d. 16-58% on the stent surface

    It is concluded that the influence of FSI is more significant on the stent surface and in the distal region of the geometric model. See Table 5.1 for a brief summary of the above conclusions.
2. If the overall objective of a study is to determine the range of the magnitude of WSS i.e., if the objective is to determine whether the WSS is < 0.5 Pa, then the results of the current study suggest that accounting for the FSI only minimally alters the magnitude of WSS. For example, in Figure (4.17), the magnitude of WSS in the region between the struts is < 0.5 Pa for both the sub-studies. Hence both the studies are pointing out that the chances of restenosis are high (restenosis occurs in regions of low and oscillatory shear stress. The oscillations also play an important role.). Given the boundary conditions of the current study, it can be concluded that the extent to

which FSI influences the magnitude of WSS is minimal when looking at the range of magnitude of WSS.

Table 5.1: Brief summary of conclusions

Parameter	Results
1. WSS at edge	
a. Proximal region of geometric model	$WSS_{noFSI} > WSS_{FSI}$
b. Distal region of geometric model	$WSS_{noFSI} > WSS_{FSI}$
c. On the stent surface	$WSS_{FSI} > WSS_{noFSI}$
d. Between the struts	$WSS_{FSI} \cong WSS_{noFSI}$
2. WSS at other locations	
a. Between the struts	$WSS_{FSI} > WSS_{noFSI}$ (except at a few locations)
3. Maximum centerline velocity	FSI > no-FSI
4. OSI at the edge	$OSI_{FSI} \cong OSI_{no\text{-}FSI}$
5. TAWSS at the edge	
a. Proximal region of geometric model	$TAWSS_{noFSI} > TAWSS_{FSI}$
b. Distal region of geometric model	$TAWSS_{noFSI} > TAWSS_{FSI}$
c. Between the struts	$TAWSS_{FSI} \cong TAWSS_{noFSI}$
d. On the stent surface	$TAWSS_{FSI} > TAWSS_{noFSI}$

3. It is doubtful that modeling a single instance of the repeated stent geometry is adequate for a reliable simulation of flow in a stented coronary artery.
4. Incorporation of physiological waveforms, actual stent geometry, a realistic, patient-specific artery geometry, a plaque model, and a layer-specific material model of the arterial wall would provide a more accurate evaluation of the performance of a specific stent placement in a patient.

5.1 Recommendations for future study

- Conduct full transient simulations to verify the validity of quasi-steady simulations
- If the objective of a study is to estimate the range of magnitude of WSS (< 0.5 Pa or > 0.5 Pa), then using a two-way FSI model may be too computationally intensive. For such situations, a one-way FSI model may be acceptable.
- Implement better arterial wall model by using a non-linear homogenous material model. Once this model converges, increase the accuracy of the model by using a multi-layer and or/anisotropic arterial material model.
- Perform non-Newtonian simulations to determine the influence of Newtonian assumption on parameters of interest.
- Reevaluate the current study with different stent geometry.
- Include the balloon expansion and plaque models.
- Implement other material models for stent like bilinear elasto-plastic material model.
- Incorporate a contact model between the stent and the artery to study the von-Mises stresses induced in the artery due to different stent materials like Nitinol and Cobalt-Chromium alloy.
- Validate the geometric model using experiments.
- Evolve the current geometry model into a patient specific pre-operative tool.
    - Create 3D patient-specific geometry and waveforms obtained by scanning the patient.
    - Incorporate most or all of the elements from the ideal finite element model (See Section 2.5).

- Run the 3D computational model and predict specific outcome for each patient.

REFERENCES

1. About.com: Biology, Cardiac Cycle, http://biology.about.com/od/anatomy/ss/cardiac_cycle.htm, Last Visited (March 5, 2012)

2. About.com: Composites/Plastics, Incompressible orthotropic materials, http://composite.about.com/library/weekly/aa990916.htm, Last Visited (March 5, 2012)

3. Balossino R, Gervaso F, Migliavacca F, Dubini G. Effects of different stent designs on local hemodynamics in stented arteries. *Journal of Biomechanics* 2008; **41**:1053-1061.

4. Bedoya J, Meyer CA, Timmins LH, Moreno MR, Moore JE. Effects of stent design parameters on normal artery wall mechanics. *Journal of Biomechanical Engineering* 2006; **128**:757-765.

5. Bols J, Degroote J, Trachet B, Verhegghe B, Segers P, Vierendeels J. A computational method to assess initial stresses and unloaded configuration of patient-specific blood vessels. Fifth International Conference on Advanced Computation Methods in Engineering ACOMEN 2011.

6. Briguori C, Sarias C, Pagnotta P, Liistro F, Montorfano M, Chieffo A, Sgura F, Corvaja N, Albiero R, Stankovic G, Toutoutzas C, Bonizzoni E, Mario CD, Colombo A. In-stent restenosis in small coronary arteries. *Journal of the American College of Cardiology* 2002; **40**:403-409.

7. Carew TE, Vaishnav RN, Patel DJ. Compressibility of the arterial wall. *Circulation Research* 1968; **23**:61-68.

8. Carlier SG, van Damme LCA, Blommerde CP, Wentzel JJ, van Langehove G, Verheye S, Kockx MM, Knaapen MWM, Cheng C, Gijsen F, Duncker DJ, Stergiopulos N, Slager CJ, Serruys PW, Krams R. Augmentation of wall shear stress inhibits neointimal hyperplasia after stent implantation: Inhibition through reduction of inflammation. *Circulation* 2003; **107**:2741-2746.

9. Computational Fluid Dynamics Laboratory, https://engineering.purdue.edu/CFDLAB/projects/blood.html, Last Visited (March 5, 2012)

10. COMSOL. CFD Module User's Guide: Version 4.2a 1998-2011.

11. COMSOL. COMSOL Multiphysics Reference Guide: Version 4.2a 1998-2011.

12. COMSOL. COMSOL Multiphysics User's Guide: Version 4.2a 1998-2011.

13. COMSOL. Structural Mechanics Module User's Guide: Version 4.2a 1998-2011.

14. Dehlaghi V, Shadpoor MT, Najarian S. Analysis of wall shear stress in stented coronary artery using 3D computational fluid dynamics modeling. *Journal of Material Processing Technology* 2008; **197**:174-181

15. DeVane MS. *Heart Smart: A Cardiologist's 5-Step Plan for Detecting, Preventing, and Even Reversing Heart Disease*. John Wiley & Sons Inc: New Jersey, 2006

16. Dictionary.com, http://dictionary.reference.com/browse/pulse, Last Visited (March 5, 2012)

17. Ding Z, Friedman MH. Dynamics of human coronary arterial motion and its potential role in coronary atherogenesis. *Journal of Biomechanical Engineering* 2000; **122**:488-492.

18. Duraiswamy N, Schoephoerster RT, Moore JE Jr. Comparison of near-wall hemodynamic parameters in stented artery models. *Journal of Biomechanical Engineering* 2009; **131**: 061006

19. Engauge digitizing software, http://digitizer.sourceforge.net/

20. Formaggia L, Gerbeau JF, Nobile F, Quarteroni A. On the coupling of 3D and 1D Navier-Stokes equations for flow problems in complaint vessels. *Computer Methods in Applied Mechanics and Engineering* 2001; **191**:561-582.

21. Fung YC. *Biomechanics: Mechanical Properties of Living Tissues*. Springer-Verlag: New York, 1981

22. Garasic JM, Edelman ER, Squire JC, Seifert P, Williams MS, Rogers C. Stent and artery geometry determine intimal thickening independent of arterial injury. *Circulation* 2000; **101**: 812-188.

23. Gasser TC, Ogden RW, Holzapfel GA. Hyperelastic modeling of arterial layers with distributed collagen fibre orientations. *Journal of the Royal Society Interface* 2006; **3**:15-35.

24. Gay M, Zhang L, Liu WK. Stent modeling using immersed finite element method. *Computer Methods in Applied Mechanics and Engineering* 2006; **195**:4358-4370.

25. Gay M, Zhang LT. Numerical studies on fluid-structure interactions of stent deployment and stented arteries. *Engineering with Computers* 2009; **25**:61-72.

26. Germann WJ, Stanfield CL. *Principles of human physiology*. Benjamin Cummins: California, 2002.

27. Hale JF, McDonald DA, Womersley JR. Velocity profiles of oscillating arterial flow, with some calculations of viscous drag and the Reynolds number. *The Journal of Physiology* 1955; **128**:629-640.

28. Heart and Education in Heart, http://heart.bmj.com/content/86/1/26.full, Last Visited (May 22, 2012)

29. History of Angioplasty, http://www.ptca.org/history_timeline.html, Last visited: (May 22, 2012)

30. Hoffmann R, Mintz GS, Hagger PK, Bozoglu T, Grube E, Gross M, Beythien C, Mudra H, Dahl JV, Hanrath P. Relation of stent design and stent surface material to subsequent in-stent intimal hyperplasia in coronary arteries determined by intravascular ultrasound. *The American Journal of Cardiology* 2002; **89**:1360-1364.

31. Holzapfel GA, Gasser TC, Ogden RW. A new constitutive framework for arterial wall mechanics and a comparative study of material models. *Journal of Elasticity* 2000; **61**:1-48.

32. Holzapfel GA, Stadler M, Gasser TC. Changes in the mechanical environment of stenotic arteries during interaction with stents: Computational assessment of parametric stent designs. *Journal of Biomechanical Engineering* 2005; **127**:166-180.

33. Hsiao H, Chiu Y, Lee K, Lin C. Computational modeling of effects of intravascular stent design on key mechanical and hemodynamic behavior. *Computer-Aided Design* 2012; **44**:757-765.

34. http://media.web.britannica.com/eb-media/71/91871-034-DA6BA042.jpg, Last Visited (March 5, 2012)

35. http://my.clevelandclinic.org/heart/heart-blood-vessels/coronary-arteries.aspx, Last Visited (March 5, 2012)

36. http://upload.wikimedia.org/wikipedia/commons/3/39/PTCA_stent_NIH.gif , Last Visited (March 5, 2012)

37. http://www.mayoclinic.com, Last Visited (March 5, 2012)

38. Humphrey JD. Mechanics of arterial wall; review and directions. *Critical Reviews in Biomedical Engineering* 1995; **23**:1-162.

39. Interventional and Surgery, http://www.theheart.org/article/1170291.do , Last Visited (May 22, 2012)

40. Kalita P, Schaefer R. Mechanical model of artery walls. *Archives of Computational Methods in Engineering* 2008; **15**:1-36.

41. Kalita P. Shell models of the artery wall. *Schedae Informaticae* 2004; **13**:103-122.

42. Kastrati A, Schomig A, Elezi S, Schuhlen H, Dirschinger J, Hadamitzky M, Wehinger A, Hausleiter J, Walter H, Neumann F. Predictive factors of restenosis after coronary stent placement. *Journal of Ameriacn College of Cardiology* 1997; **30**:1428-1436

43. Khurana I. *Essentials of Medical Physiology*. Elsevier: India, 2008.

44. Kleinstreuer C. *Biofluid Dynamics: Principles and Selected Applications*. CRC Press: Florida, 2006.

45. Koshiba N, Ando J, Chen X, Hisada T. Multiphysics simulation of blood flow and LDL transport in a porohyperelastic arterial wall mode. *Journal of Biomechanical Engineering* 2007; **129**:374-385.

46. Kreyszig E. *Advanced Engineering Mathematics* (9th edn). John Wiley and Sons: New Jersey, 2006.

47. Ku DN, Giddens DP, Zarins CK, Glagov S. Pulsatile flow and atherosclerosis in human carotid bifurcation. Positive correlation between plaque location and low and oscillating shear stress. *Atherosclerosis, Thrombosis, and Vascular Biology* 1985; **5**:293-302.

48. Ku DN. Blood flow in arteries. *Annual Review of Fluid Mechanics* 1997; **29**:399-434.

49. LaDisa JF Jr, Olson LE, Guler I, Hettrick DA, Audi SH, Kersten JR, Warltier DC, Pagel PS. Stent design properties and deployment ratio influence indexes of wall shear stress: a three-dimensional computational fluid dynamics investigation within normal artery. *Journal of Applied Physiology* 2004; **97**:424-430

50. LaDisa JF Jr, Olson LE, Hettrick DA, Warltier DC, Kersten JR, Pagel PS. Axial stent strut angle influences wall shear stress after stent implantation: analysis using 3D computational fluid dynamic models of stent foreshortening. *BioMedical Engineering Online* 2005; **4**:59.

51. LaDisa JF Jr., Olson LE, Molthen RC, Hettrick DA, Pratt PE, Hardel MD, Kersten JR, Warltier DC, Pagel PS. Alterations in wall shear stress predict sites of neointimal hyperplasia after stent implantation in rabbit iliac arteries. *American Journal of Physiology: Heart and Circulatory Physiology* 2005; **288**:2465-2475.

52. LaDisa JF, Jr Guler I, Olson LE, Hettrick DA, Kersten JR, Warltier DC, Pagel PS. Three-dimensional computational fluid dynamics modeling of alterations in coronary wall shear stress produced by stent implantation. *Annals of Biomedical Engineering* 2003; **31**:972-980

53. Lally C, Dolan F, Prendergast PJ. Cardiovascular stent design and vessel stresses: a finite element analysis. *Journal of Biomechanics* 2005; **38**:1574-1581

54. Lepore MR, Yoselevitz M, Sternbergh III WC, Money SR. Minimally Invasive Vascular Techniques. *The Ochsner Journal* 2000; **2**(3):145-152

55. Lewis G. Review materials, fluid dynamics, and solid mechanics aspects of coronary artery stents: A state-of-the-art review. *Journal of Biomedical Materials Research Part B: Applied Biomaterials* 2008; **86B**(2):569-590

56. Li MX, Beech-Brandt JJ, John LR, Hoskins PR, Easson WJ. Numerical analysis of pulsatile blood flow and vessel wall mechanics in different degrees of stenoses. *Journal of Biomechanics* 2007; **40**:3715-3724.

57. Lüdinghausen MV. *The Clinical Anatomy of the Coronary Arteries*. Springer-Verlag Berlin: Heidelberg, 2003

58. Mates RE, Gupta RL, Bell AC, Klocke FJ. Fluid dynamics of coronary artery stenosis. *Circulation Research* 1978; **42**:152-162.

59. Mauri L, O'Malley AJ, Cutlip DE, Ho KKL, Popma JJ, Chauhan MS, Baim DS, Cohen DJ, Kuntz RE. Effects of stent length and lesion length on coronary restenosis. *The American Journal of Cardiology* 2004; **93**:1340-1346.

60. McDonald DA. The relation of pulsatile pressure to flow in arteries. *The Journal of Physiology* 1955; **127**: 533-552.

61. Medline Plus, Coronary Heart Disease, http://www.nlm.nih.gov/medlineplus/ency/article/007115.htm, Last Visited (March 5, 2012)

62. Medpedia: Cardiac Stent, http://wiki.medpedia.com/Cardiac_Stent#Types, Last Visited (May 22, 2012)

63. Medscape Today, http://www.medscape.com/viewarticle/523241_2, Last Visited (May 22, 2012)

64. Medtronic, http://wwwp.medtronic.com/Newsroom/LinkedItemDetails.do?itemId=1199741324094&itemType=glossary&lang=en_US (March 17, 2012)

65. Merriam-Webster, http://www.merriam-webster.com/medical/neointima, Last Visited (March 5, 2012)

66. Mills CJ, Gabe IT, Gault JH, Mason DT, Ross J Jr. Pressure-flow relationships and vascular impedance in man. *Cardiovascular Research* 1970; **4**:405-417.

67. Milnor WR. *Hemodynamics* (1st edn).Williams & Wilkins: Maryland, 1989.

68. Morton AC, Crossman D, Gunn J. The influence of physical stent parameters upon restenosis. *Pathologie Biologie* 2004; **52**:196-205

69. Murphy J, Boyle F. Predicting neointimal hyperplasia in stented arteries using time-dependent computation fluid dynamics: A review. *Computers in Biology and Medicine* 2010

70. Myers JG, Moore JA, Ojha M, Johnston KW, Ethier CR. Factors influencing blood flow patterns in the human right coronary artery. *Annals of Biomedical Engineering* 2001; **29**:109-120.

71. Nichols WW, O'Rourke MF. *McDonald's Blood Flow in Arteries: Theoretical, Experimental and Clinical Principles* (5th edn). Hodder Arnold: London, 2005.

72. Niemann AK, Udesen J, Thrysoe S, Nygaard JV, Frund E, Petersen SE, Hasenkam JM. Can sites prone to flow induced vascular complications in a-v fistulas be assessed using computational fluid dynamics? *Journal of Biomechanics* 2010; **43**:2002-2009.

73. Nordgaard H, Swillens A, Nordhaug D, Kirkeby-Garstad I, Loo DV, Vitale N, Segers P, Haaverstad R, Lovstakken L. Impact of competitive flow on wall shear stress in coronary surgery: computational fluid dynamics of a LIMA-LAD model. *Cardiovascular Research* 2010; **88**:512-519.

74. Patel DJ, Vaishnav RN. *Basic Hemodynamics and Its Role in Disease Processes*. University Park Press: Maryland, 1980

75. Percutaneous Transluminal Coronary Angioplasty, http://www.cardiocentercy.com/index.php/articles/66-percutaneous-transluminal-coronary-angioplasty

76. Perktold K, Hofer M, Rappitsch G, Loew M, Kuban BD, Friedman MH. Validated computation of physiologic flow in a realistic coronary artery branch. *Journal of Biomechanics* 1998; **31**:217-228.

77. Perktold K, Rappitsch G. Computer simulations of local blood flow and vessel mechanics in a compliant carotid artery bifurcation model. *Journal of Biomechanics* 1995; **28**:845-856.

78. Prati F, Di Mario C, Moussa I, Reimers B, Mallus MT, Parma A, Lioy E, Colombo A. In-stent neointimal proliferation correlates with the amount of residual plaque burden outside the stent: An intravascular ultrasound study. *Circulation* 1999; **99**:1011-1014.

79. Prendergast PJ, Lally C, Daly S, Reid AJ, Lee TC, Quinn D, Dolan F. Analysis of prolapse in cardiovascular stents: A constitutive equation for vascular tissue and finite-element modeling. *Journal of Biomechanical Engineering* 2003; **125**:692-699.

80. Reddy JN. *An Introduction to the Finite Element Method* (3rd edn). McGraw Hill: NewYork, 2006.

81. Rogers C, Edelman ER. Endovascular stent design dictates experimental restenosis and thrombosis. *Circulation* 1995; **91**:2995–3001

82. Schwartz RS. Pathophysiology of restenosis: Interaction of thrombosis, hyperplasia, and/or remodeling. *The American Journal of Cardiology* 1998; **81**:14E-17E.

83. Serruys PW, Daemen J. Late stent thrombosis: A nuisance in both bare metal and drug-eluting stents. *Circulation* 2007; **115**:1433-1439.

84. Serruys PW, Kutryk MJB, Ong ATL. Coronary-artery stents. *The New England Journal of Medicine* 2006; **354**:483-495

85. Stoeckel D, Bonsignore C, Duda S. A survey of stent designs. *Minimally invasive therapy & allied technologies* 2002; **11**:137–147

86. Tang D, Yang C, Huang Y, Ku DN. Wall stress and strain analysis using a three-dimensional thick-wall model with fluid-structure interactions for blood flow in carotid arteries with stenoses. *Computers and Structures* 1999; **72**:341-356.

87. Tang D, Yang C, Kobayashi S, Ku DN. Steady flow and wall compression in stenotic arteries: A three-dimensional thick-wall model with fluid-wall interactions. *Journal of Biomechanical Engineering* 2001; **123**:548-557.

88. Tang D, Yang C, Ku DN. A 3-D thin wall model with fluid-structure interactions for blood flow in carotid arteries with symmetric and asymmetric stenoses. *Computers and Structures* 1999; **72**:357-377.

89. Taylor CA, Hughes TJR, Zarins CK. Finite element modeling of blood flow in arteries. *Computer Methods in Applied Mechanics and Engineering* 1998; **158**:155-196.

90. Torii R, Oshima M, Kobayashi T, Takagi K, Tezduyar TE. Computer modeling of cardiovascular fluid-structure interactions with the deforming-spatial-domain/stabilized space-time formulation. *Computer Methods in Applied Mechanics and Engineering* 2006; **195**:1885-1895

91. Torii R, Wood NB, Hadjiloizou N, Dowsey AW, Wright AR, Hughes AD, Davies J, Francis DP, Mayet J, Yang G, Thom SAM, Xu XY. Fluid–structure interaction analysis of a patient-specific right coronary artery with physiological velocity and pressure waveforms. *Communications in Numerical Methods in Engineering* 2009; **25**(5):565-580

92. Uchida S. The pulsating viscous flow superposed on the steady laminar motion of incompressible fluid in a circular pipe. *Zeitschrift für Angewandte Mathematik und Physik (ZAMP)* 1956; **7**(5):403-422

93. Vavourakis V, Papaharilaou Y, Ekaterinaris JA. Coupled fluid-structure interaction hemodynamics in a zero-pressure state corrected arterial geometry. *Journal of Biomechanics* 2011; **44**:2453-2460.

94. Vector and Tensor Mathematics, http://www.polymerprocessing.com/notes/root92a.pdf

95. Wentzel JJ, Whelan DM, van der Giessen WJ, van Beusekom HMM, Andhyiswara I, Serruys PW, Slager CJ, Krams R. Coronary stent implantation changes 3-D vessel geometry and 3-D shear stress distribution. *Journal of Biomechanics* 2000; **33**:1287-1295.

96. Wikipedia: Andreas_Gruentzig, http://en.wikipedia.org/wiki/Andreas_Gruentzig, Last Visited (March 5, 2012)

97. Wikipedia: Angioplasty#Coronary_angioplasty, http://en.wikipedia.org/wiki/Angioplasty#Coronary_angioplasty, Last Visited (March 5, 2012)

98. Wikipedia: Angioplasty, http://en.wikipedia.org/wiki/Angioplasty, Last Visited (March 5, 2012)

99. Wikipedia: Artery, http://en.wikipedia.org/wiki/Artery, Last Visited (March 5, 2012)

100. Wikipedia: Atheroma, http://en.wikipedia.org/wiki/Atheroma, Last Visited (March 5, 2012)

101. Wikipedia: Atherosclerosis, http://en.wikipedia.org/wiki/Atherosclerosis, Last Visited (March 5, 2012)

102. Wikipedia: Bare-metal_stent, http://en.wikipedia.org/wiki/Bare-metal_stent, Last Visited (March 5, 2012)

103. Wikipedia: Blood_vessel, http://en.wikipedia.org/wiki/Blood_vessel, Last Visited (March 5, 2012)

104. Wikipedia: Cardiac_cycle, http://en.wikipedia.org/wiki/Cardiac_cycle, Last Visited (March 5, 2012)

105. Wikipedia: Coronary_artery_bypass_surgery, http://en.wikipedia.org/wiki/Coronary_artery_bypass_surgery, Last Visited (March 5, 2012)

106. Wikipedia: Drug-eluting stent, http://en.wikipedia.org/wiki/Drug-eluting_stent, Last Visited (May 22, 2012)

107. Wikipedia: Embolism, http://en.wikipedia.org/wiki/Embolism, Last Visited (March 5, 2012)

108. Wikipedia: Endothelium, http://en.wikipedia.org/wiki/Endothelium, Last Visited (March 5, 2012)

109. Wikipedia: fibrous cap, http://en.wikipedia.org/wiki/Fibrous_cap, Last Visited (March 5, 2012)

110. Wikipedia: Fluid-structure_interaction, http://en.wikipedia.org/wiki/Fluid-structure_interaction, Last visited (May 22, 2012)

111. Wikipedia: Fourier series, http://en.wikipedia.org/wiki/Fourier_series

112. Wikipedia: Heart_disease, http://en.wikipedia.org/wiki/Heart_disease, Last Visited (March 5, 2012)

113. Wikipedia: Percutaneous_coronary_intervention, http://en.wikipedia.org/wiki/Percutaneous_coronary_intervention, Last Visited (March 5, 2012)

114. Wikipedia: Restenosis, http://en.wikipedia.org/wiki/Restenosis, Last Visited (March 5, 2012)

115. Wikipedia: Stenosis, http://en.wikipedia.org/wiki/Stenosis, Last Visited (March 5, 2012)

116. Wikipedia: Systemic_circulation, http://en.wikipedia.org/wiki/Systemic_circulation, Last Visited (March 5, 2012)

117. Wikipedia: Thromboembolism, http://en.wikipedia.org/wiki/Thromboembolism, Last Visited (March 5, 2012)

118. Wikipedia: Vulnerable_plaque, http://en.wikipedia.org/wiki/Vulnerable_plaque, Last Visited (March 5, 2012)

119. Wikipedia: Womersley_number, http://en.wikipedia.org/wiki/Womersley_number, Last Visited (March 5, 2012)

120. Wikiversity: Introduction to Elasticity/Tensors, http://en.wikiversity.org/wiki/Introduction_to_Elasticity/Tensors#Magnitude_of_a_tensor

121. Womersley JR. Method for the calculation of velocity, rate of flow and viscous drag in arteries when the pressure gradient is known. *The Journal of Physiology* 1955; **127**:553-563.

122. World Health Organization, http://www.who.int/mediacentre/factsheets/fs317/en/index.html, Last Visited (March 5, 2012)

123. Wu W, Wang W, Yang D, Qi M. Stent expansion in curved vessel and their interactions: A finite element analysis. *Journal of Biomechanics* 2007; **40**:2580-2585.

124. Zahenmanesh H, Lally C. Determination of the influence of stent strut thickness using the finite element method: implications for vascular injury and in-stent restenosis. *Medical and Biological Engineering and Computing* 2009; **47**:385-393.

125. Zamir M. *The Physics of Pulsatile Flow*. Springer-Verlag: New York, 2000.

126. Zarandi MM, Mongrain R, Bertrand OF. Non-Newtonian hemodynamics and shear stress distribution in three dimensional model of healthy and stented coronary artery bifurcation. Proceeding of the COMSOL Conference 2010; Boston.

127. Zarins CK, Giddens DP, Bharadvaj BK, Sottiurai VS, Mabon RF, Glagov S. Carotid bifurcation atherosclerosis Quantitative correlation of plaque localization with flow velocity profiles and wall shear stress. *Circulation Research* 1983; **53**:502-514.

128. Zeng D, Boutsianis E, Ammann M, Boomsma K, Wildermuth S, Poulikakos D. A study on the compliance of a right coronary artery and its impact on wall shear stress. *Journal of Biomechanical Engineering* 2008; **130**:1-11.

129. Zhou R, Lee T, Tsou T, Rannou F, Li Y, Chien S, Shyy JYJ. Stent implant activates akt in vessel wall: Role of mechanical stretch in vascular smooth muscle cells. *Arteriosclerosis, Thrombosis, and Vascular Biology* 2003; **23**:2015-2020.

APPENDIX A. FOURIER SERIES REPRESENTATION OF A GENERIC FUNCTION f(t)

Based on Fourier series theorem, any periodic function $\left(f\left(t+T\right)=f\left(t\right)\right)$, can be approximated by a Fourier series [46], [111] given by

$$f(t)=\sum_{-M}^{M}C_n e^{\mathrm{i}n\omega t}=\begin{cases}C_{-M}e^{-\mathrm{i}M\omega t}+C_{-(M-1)}e^{-\mathrm{i}(M-1)\omega t}+....+C_{-1}e^{-\mathrm{i}\omega t}+C_0+C_1e^{\mathrm{i}\omega t}+....\\ ....+C_{(M-1)}e^{\mathrm{i}(M-1)\omega t}+C_N e^{\mathrm{i}M\omega t}\end{cases} \quad (A.1)$$

C_n is the Fourier coefficient given by $C_n=A_n-iB_n$ $\left(\text{for } n\geq 0\right)$ and $\omega=\dfrac{2\pi}{T}$

If $C_{-n}=\overline{C_n}$, then $C_0=\overline{C_0}\Rightarrow A_0-iB_0=A_0+iB_0\Rightarrow B_0=0\Rightarrow C_0=A_0$:

Also if $C_{-n}=\overline{C_n}$, then

$$\begin{aligned}f(t)&=\begin{cases}C_{-M}e^{-\mathrm{i}M\omega t}+C_{-(M-1)}e^{-\mathrm{i}(M-1)\omega t}+....+C_{-1}e^{-\mathrm{i}\omega t}+C_0+C_1e^{\mathrm{i}\omega t}+....\\ ....+C_{(M-1)}e^{\mathrm{i}(M-1)\omega t}+C_N e^{\mathrm{i}M\omega t}\end{cases}\\ &=\begin{cases}\overline{C_M}e^{-\mathrm{i}M\omega t}+\overline{C_{(M-1)}}e^{-\mathrm{i}(M-1)\omega t}+....+\overline{C_1}e^{-\mathrm{i}\omega t}+C_0+C_1e^{\mathrm{i}\omega t}+....\\ ....+C_{(M-1)}e^{\mathrm{i}(M-1)\omega t}+C_M e^{\mathrm{i}M\omega t}\end{cases}\\ &=\begin{cases}\overline{C_M e^{\mathrm{i}M\omega t}}+\overline{C_{(M-1)}e^{\mathrm{i}(M-1)\omega t}}+....+\overline{C_1e^{\mathrm{i}\omega t}}+C_0+C_1e^{\mathrm{i}\omega t}+....\\ ....+C_{(M-1)}e^{\mathrm{i}(M-1)\omega t}+C_M e^{\mathrm{i}M\omega t}\end{cases}\end{aligned}$$

But $\overline{C_M e^{\mathrm{i}M\omega t}}+C_M e^{\mathrm{i}M\omega t}=2\,\mathrm{Re}\left[C_M e^{\mathrm{i}M\omega t}\right]$

Note: $\overline{C_M e^{\mathrm{i}M\omega t}}+C_M e^{\mathrm{i}M\omega t}=\overline{C_M}e^{-\mathrm{i}M\omega t}+C_M e^{\mathrm{i}M\omega t}$

$$\begin{aligned}&=\begin{cases}\left(A_M+iB_M\right)\left(\cos M\omega t-i\sin M\omega t\right)+\\ \left(A_M-iB_M\right)\left(\cos M\omega t+i\sin M\omega t\right)\end{cases}\\ &=2\left(A_M\cos M\omega t+B_M s\sin M\omega t\right)\\ &=2\,\mathrm{Re}\left[C_M e^{\mathrm{i}M\omega t}\right]\end{aligned}$$

Therefore,

$$
\begin{aligned}
f(t) &= C_0 + 2\left(C_1 e^{\mathrm{i}\omega t} + ... + C_{(M-1)} e^{\mathrm{i}(M-1)\omega t} + C_M e^{\mathrm{i}M\omega t}\right) \\
&= C_0 + 2\sum_{n=1}^{M} \mathrm{Re}\left[C_n e^{in\omega t}\right] \\
&= A_0 + 2\sum_{n=1}^{M} \mathrm{Re}\left[C_n e^{in\omega t}\right] \quad \left(\because C_0 = A_0\right)
\end{aligned}
$$

Using $C_n = A_n - iB_n$ $\left(\text{for } n \geq 0\right)$ and Euler formula, $e^{\mathrm{i}M\omega \mathrm{t}} = \cos M\omega t + i \sin M\omega t$ obtains

$$
\begin{aligned}
f(t) &= A_0 + 2\sum_{n=1}^{M} \mathrm{Re}\left[\left(A_n - iB_n\right)\left(\cos n\omega t + i \sin n\omega t\right)\right] \\
&= A_0 + 2\sum_{n=1}^{M} \left(A_n \cos n\omega t + B_n \sin n\omega t\right)
\end{aligned}
\tag{A.2}
$$

The above derivation proves that if $C_{-n} = \overline{C_n}$, then $f(t)$ is real and vice versa.

Note:

- C_n can be replaced by p_n, ψ_n, u_n, q_n etc
- $f(t)$ can be replaced by any periodic function $\frac{\partial p}{\partial x}$, $p(x,t), u(r,t), Q(t)$

APPENDIX B. FOURIER COEFFICIENTS a_{pn} AND b_{pn} OF A PERIODIC PRESSURE WAVEFORM

Consider a straight pipe whose centerline axis coincides with the x-axis of the cylindrical coordinate system. Let the pressure along the centerline (or axis) of the pipe be periodic with a period T given by $\left(T = \frac{2\pi}{\omega}\right)$. If this periodic pressure is represented as $p(t)$, then, using Fourier series theorem, the pressure can be expressed as:

$$p(x,t) = \sum_{n=-M}^{M} p_n(x) e^{in\omega t} \tag{B.1}$$

where $p_n(x) = a_{pn}(x) - ib_{pn}(x)$ $(\text{for } n \geq 0)$

Pressure is a function of x and t only ([92], See Appendix C also for details).

For $p(x,t)$ to be real, impose $p_{-n}(x) = \overline{p_n(x)}$, then Equation (B.1) becomes

$$p(t) = \sum_{n=-M}^{M} p_n(x) e^{in\omega t} = a_{p0} + 2\sum_{n=1}^{M}\left(a_{pn}(x)\cos n\omega t + b_{pn}(x)\sin n\omega t\right) \tag{B.2}$$

and a_{p0}, a_{pn} and b_{pn} are evaluated by using the following expressions:

$$a_{p0} = \frac{1}{2\pi}\int_{-\pi}^{\pi} p(t)dt \tag{B.3}$$

$$a_{pn}(x) = \frac{1}{2\pi}\int_{-\pi}^{\pi} p(t)\cos(nt)\,dt \tag{B.4}$$

$$b_{pn}(x) = \frac{1}{2\pi}\int_{-\pi}^{\pi} p(t)\sin(nt)\,dt \tag{B.5}$$

In Equation (B.2), the details on how $\sum_{n=-M}^{M} p_n(x)e^{in\omega t}$ reduces to

$a_{p0} + 2\sum_{n=1}^{M}\left(a_{pn}(x)\cos n\omega t + b_{pn}(x)\sin n\omega t\right)$ is shown in Appendix A.

If an analytic expression for the periodic pressure is not available, then it is determined from experimental measurements by using a Fourier series approximation as described below.

From the experimental measurements, the periodic pressure values are known at N equally spaced points. Considering that the period of the pressure gradient is T, then the length of each interval is given by $\frac{T}{N}$. If Δt_{int} represents the length of each interval, then

$$\Delta t_{\text{int}} = \frac{T}{N} \tag{B.6}$$

If t_k and p_k represent the time and the experimental measurements of the pressure gradient at the end of each interval, then the value of t_k at the end of each interval is given by

$$t_k = k\Delta t_{\text{int}} = k\frac{T}{N},\ k=0,1,2....N\text{-}1 \tag{B.7}$$

From Equation (B.2), $p(x,t) = a_{p0} + 2\sum_{n=1}^{M} a_{pn}(x)\cos(n\omega t) + 2\sum_{n=1}^{M} b_{pn}(x)\sin(n\omega t)$, (B.8)

where $\omega = \frac{2\pi}{T}$ (B.9)

and M=N/2

If the analytic function of the periodic pressure $p(x,t)$ is not available, then the following approximation can be used to find the Fourier coefficients:

$$a_{p0} = \frac{1}{N}\sum_{k=0}^{N-1} p_k \tag{B.10}$$

$$a_{pn}(x) = \frac{1}{N}\sum_{k=0}^{N-1} p_k \cos(n\omega t_k) \tag{B.11}$$

$$b_{pn}(x) = \frac{1}{N}\sum_{k=0}^{N-1} p_k \sin(n\omega t_k) \tag{B.12}$$

If T is the period of the function $f(t)$ and there are N points in this period where the pressure is known, then, N coefficients can be determined. These N coefficients are given by $a_{p0}, a_{p1}, ...a_{pN/2}, b_{p1}, b_{p2}, ...b_{p(N/2-1)}$. b_0 *and* $b_{N/2}$ are zero. The above procedure can be used to compute the Fourier coefficients of the periodic pressure waveform shown in Figure (B.1)

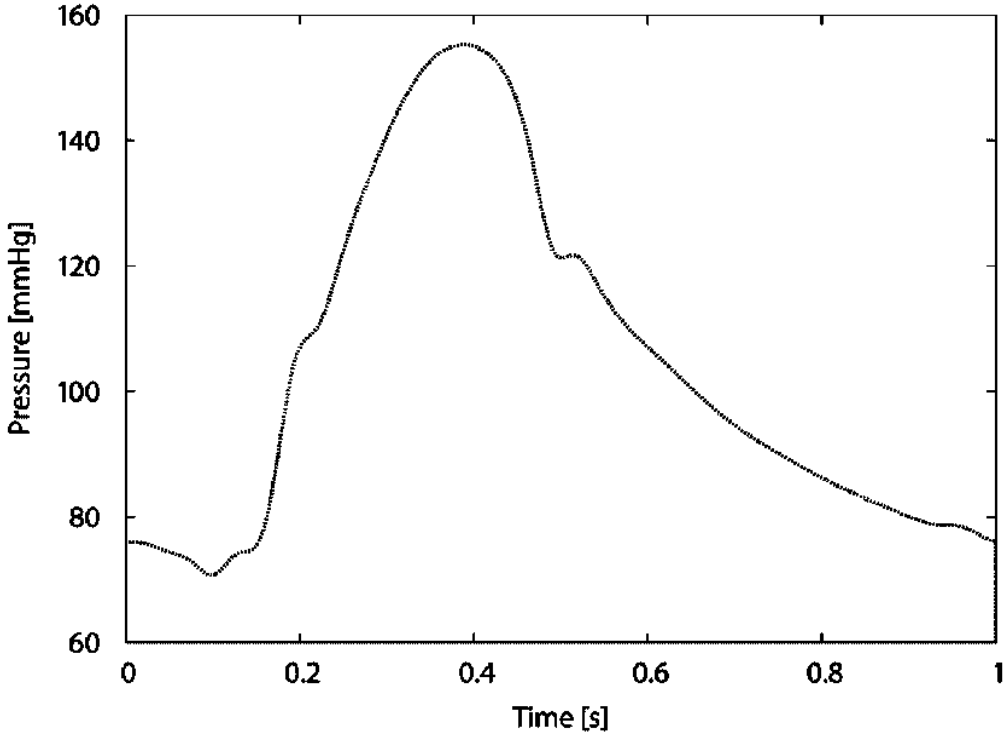

Figure B.1 – Periodic pressure waveform obtained from experimental results

Let p(x,t) be the pressure waveform shown in Figure (B.1). The data corresponding to this waveform was extracted using a digitizing software, Engauge Digitizer [19]. The period of the above waveform, T = 1 s [91], was divided into 48 intervals i.e., N equally spaced ordinates.

$$T = 1\ [\mathrm{s}] \tag{B.13}$$

$$f = \frac{1}{T}\ [Hz] \tag{B.14}$$

$$\omega = 2\pi f\ [rad/s] = 2\pi \times 1 = 6.2832\ [rad/s] \tag{B.15}$$

$$N = 48 \tag{B.16}$$

$$\Delta t_{\mathrm{int}} = \frac{T}{N} = \frac{1}{48} = 0.0208\,[s] \tag{B.17}$$

$$t_k = k\Delta t_{\text{int}} = k\frac{T}{N},\ k = 0,1,2,3.....47 \tag{B.18}$$

t_k is the time coordinate at k = 0,1,2,….47. The data that were extracted from Figure (B.1) with the help of the digitizing software were linearly interpolated to obtain the pressure (p_k) values corresponding to the time (t_k) values. Using Equations (B.10), (B.11) and (B.12), Fourier coefficients for p(x,t) were computed. These are shown in Table (B.1).

Table (B.1): Fourier coefficients for the pressure waveform shown in Figure (B.1)

n	ap0	ap	bp
0	104.1708		
1		-15.3580	8.0815
2		-1.1588	-7.1872
3		2.4370	0.1338
4		0.0246	-0.2356
5		0.9446	0.5125
6		-0.4836	0.4411
7		0.0173	0.0861
8		-0.5482	-0.0478
9		0.2699	-0.4775
10		0.0124	0.1269
11		0.2565	-0.0011
12		-0.2930	0.3539
13		-0.1317	-0.2071
14		-0.1204	-0.0478
15		0.1590	-0.2412
16		0.0952	0.1642
17		0.0495	0.0229
18		-0.0897	0.1449
19		-0.0754	-0.0783
20		-0.0014	-0.0286
21		-0.0089	-0.0192
22		-0.0074	0.0135
23		-0.0258	-0.0396
24		0.0673	0.0000

Equation (B.8) and the Fourier coefficients from Table (B.1) were used to obtain an expression for p(t).

Figure (B.2) shows a comparison of the pressure waveform p(x,t) that was recreated using the digitized data obtained from Figure (B.1) to the pressure waveform that was obtained using the Fourier series. It can be observed that the:

- Plot of the digitized pressure data is similar to the waveform shown in Figure (B.1)
- Pressure expression obtained from the Fourier series yields a waveform that closely resembles the one obtained from the digitized data.

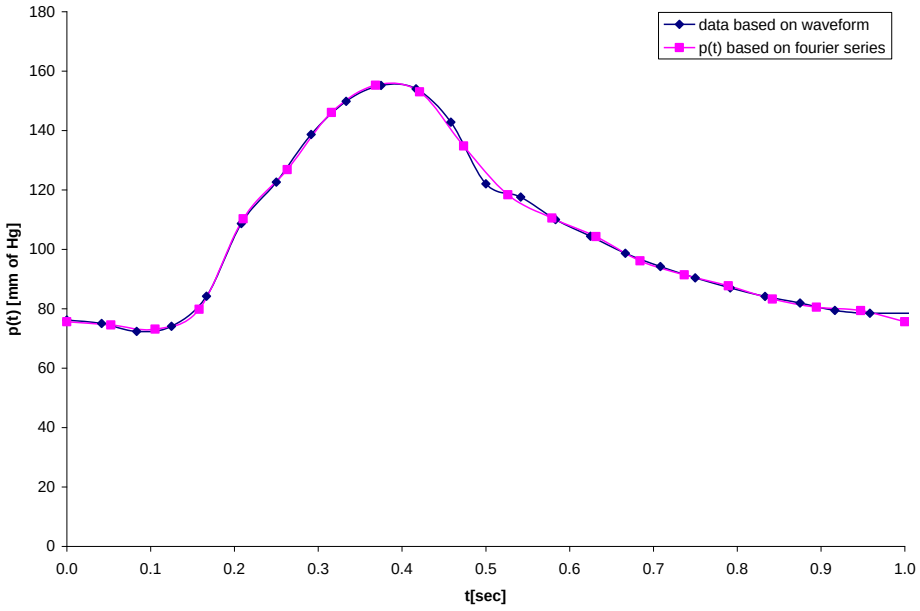

Figure B.2 – Comparison of the pressure waveform p(x,t) that was recreated using the digitized data obtained from Figure (B.1) to the pressure waveform that was obtained using the Fourier series

The Fourier coefficients a_{vn} and b_{vn} of a periodic velocity waveform

A periodic velocity waveform can be approximated by a Fourier series as:

$$v(r,t) = \sum_{n=-M}^{M} u_n(r) e^{in\omega t}, \tag{B.19}$$

where $\omega = \frac{2\pi}{T}$ (B.20)

and M = N/2

$u_n(r) = a_{vn}(r) - ib_{vn}(r)$ (for $n \geq 0$) and for $v(r,t)$ to be real, impose $u_{-n}(r) = \overline{u_n(r)}$.

Appendix C explains why the above velocity is a function of r and t only.

Then Equation (B.19) becomes

$$v(r,t) = \sum_{n=-M}^{M} u_n(r) e^{in\omega t} = a_{v0} + 2\sum_{n=1}^{M} a_{vn}(r)\cos(n\omega t) + 2\sum_{n=1}^{M} b_{vn}(r)\sin(n\omega t) \tag{B.21}$$

In Equation (B.21), the details on how $\sum_{n=-M}^{M} u_n(r) e^{in\omega t}$ reduces to

$a_{v0} + 2\sum_{n=1}^{M} a_{vn}(r)\cos(n\omega t) + 2\sum_{n=1}^{M} b_{vn}(r)\sin(n\omega t)$ is shown in Appendix A.

If the analytic function of the periodic velocity $v(r,t)$ is not available, then the following approximation can be used to find the Fourier coefficients:

$$a_{v0} = \frac{1}{N}\sum_{k=0}^{N-1} v_k \tag{B.22}$$

$$a_{vn}(r) = \frac{1}{N}\sum_{k=0}^{N-1} v_k \cos(n\omega t_k) \tag{B.23}$$

$$b_{vn}(r) = \frac{1}{N}\sum_{k=0}^{N-1} v_k \sin(n\omega t_k) \tag{B.24}$$

The values of T, f, ω, N, Δt_{int}, and t_k are the same as the ones that are used for computing Fourier coefficients a_{pn} and b_{pn} of the periodic pressure waveform. The data that were extracted from Figure (B.3) with the help of the digitizing software were linearly interpolated to obtain the velocity (v_k) values corresponding to the time (t_k) values. Equations (B.22), (B.23) and (B.24) were used to compute the Fourier coefficients of the periodic velocity waveform shown in Figure (B.3). The coefficients are shown in Table (B.2)

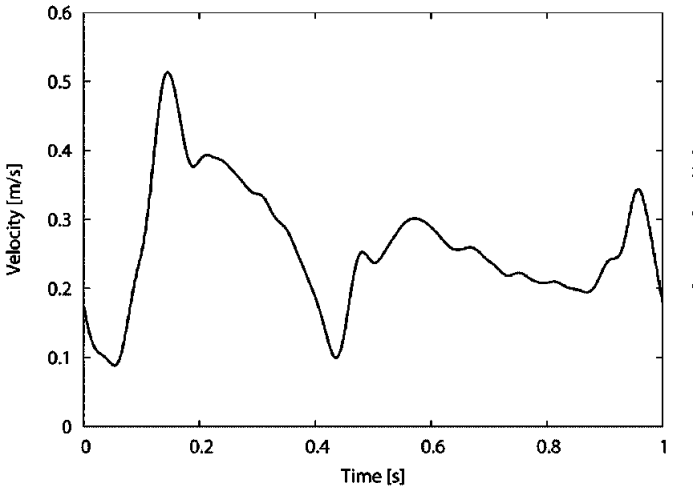

Figure B.3 – Periodic maximum velocity waveform obtained from experimental results

Table (B.2): Fourier coefficients for the velocity waveform shown in Figure (B.3)

n	av0	av	bv
0	0.2610		
1		0.0005	0.0254
2		-0.0253	0.0189
3		-0.0114	-0.0292
4		-0.0049	-0.0110
5		-0.0033	-0.0249
6		0.0083	-0.0128
7		0.0029	-0.0069
8		0.0049	-0.0028
9		-0.0023	0.0049
10		-0.0035	-0.0028
11		-0.0042	0.0002
12		-0.0022	-0.0050
13		0.0011	-0.0003
14		-0.0013	-0.0004
15		0.0002	0.0028
16		-0.0029	0.0013
17		-0.0007	0.0007
18		-0.0018	0.0002
19		0.0006	-0.0007
20		0.0006	0.0003
21		0.0009	-0.0001
22		0.0007	0.0004
23		0.0004	0.0002
24		0.0000	0.0000

Equation (B.21) and the Fourier coefficients from Table (B.2) were used to obtain an expression for v(t). Figure (B.4) shows a comparison of the velocity waveform v(r,t) that was recreated using the digitized data obtained from Figure (B.3) to the velocity waveform that was obtained using the Fourier series. It can be observed that the:

- Plot of the digitized velocity data is similar to the waveform shown in Figure (B.3)
- Velocity expression obtained from the Fourier series yields a waveform that closely resembles the one obtained from the digitized data.

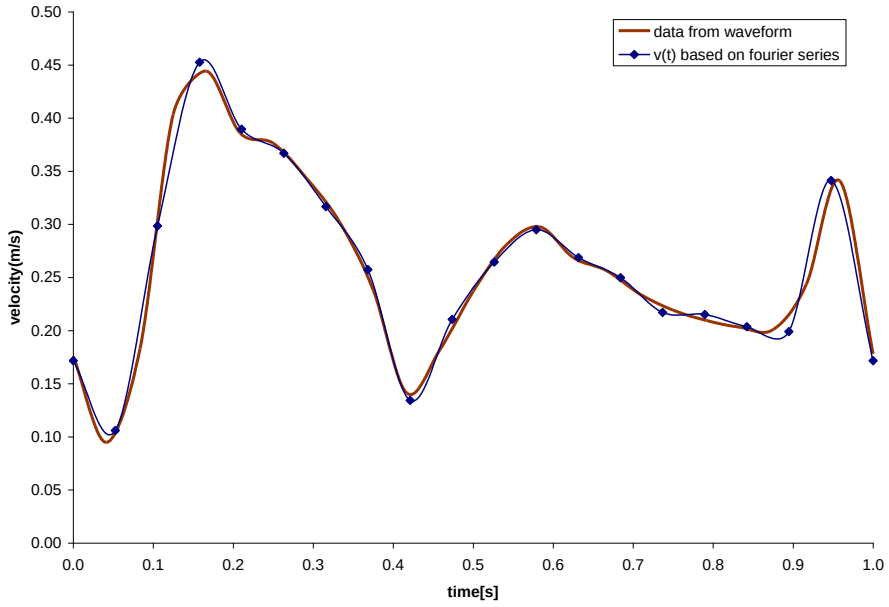

Figure B.4 – Comparison of the velocity waveform v(r,t) that was recreated using the digitized data obtained from Figure (B.3) to the velocity waveform that was obtained using the Fourier series

Velocity shown in Figure (B.4) is the spatial maximum velocity. Assuming that velocity profile is parabolic, the flow rate can be estimated. Even though this assumption contradicts the Womersley velocity profile, previous studies in this area suggest that this is the best approximation available. Hence

$$Q(r,t) = \frac{1}{2} u_{\max}(r,t) A \tag{B.25}$$

$$\sum_{n=-N}^{N} q_n(r) e^{in\omega t} = \frac{1}{2} \sum_{n=-N}^{N} u_n(r) e^{in\omega t} A$$

Comparing coefficients of $e^{in\omega t}$ on both sides of the above equation gives

$$q_n(r) = \frac{1}{2} u_n(r) A$$

$$a_{qn}(r) - ib_{qn}(r) = \frac{1}{2}\left(a_{vn}(r) - ib_{vn}(r)\right)A$$

Hence $a_{qn}(r) = \frac{A}{2}a_{vn}(r)$ and $b_{qn}(r) = \frac{A}{2}b_{vn}(r)$

The Fourier coefficients computed using these expressions are shown in Table (B.3)

Table (B.3): Fourier coefficients for the flow rate computed from velocity waveform shown in Figure (B.4)

n	aq0	aq	bq
0	8.15E-07		
1		1.40E-09	7.92E-08
2		-7.91E-08	5.91E-08
3		-3.56E-08	-9.12E-08
4		-1.52E-08	-3.45E-08
5		-1.03E-08	-7.78E-08
6		2.60E-08	-3.99E-08
7		8.92E-09	-2.15E-08
8		1.54E-08	-8.81E-09
9		-7.02E-09	1.53E-08
10		-1.09E-08	-8.76E-09
11		-1.32E-08	5.29E-10
12		-6.72E-09	-1.57E-08
13		3.53E-09	-9.39E-10
14		-4.06E-09	-1.12E-09
15		6.14E-10	8.80E-09
16		-9.17E-09	4.17E-09
17		-2.10E-09	2.05E-09
18		-5.52E-09	7.30E-10
19		1.89E-09	-2.29E-09
20		1.86E-09	1.09E-09
21		2.85E-09	-3.00E-10
22		2.22E-09	1.12E-09
23		1.28E-09	5.04E-10
24		-1.95E-11	-1.34E-22

APPENDIX C. VELOCITY PROFILE FOR A PULSATILE WAVE IN A STRAIGHT PIPE OF CIRCULAR SECTION

Consider a Newtonian, viscous, and incompressible fluid having density ρ, and dynamic viscosity μ, flowing in a straight pipe of circular section of length *l*, and radius R. Assume that the centerline of the pipe coincides with the x-axis of the cylindrical coordinates. For a steady flow, if p_1 and p_2 are the pressures at the inlet and outlet of the pipe, then the pressure gradient driving the fluid is given by $\frac{p_1 - p_2}{l} = -\frac{dp}{dx}$.

In this case, the continuity equation and the Navier-Stokes equation are given by:

$$\frac{1}{r}\frac{\partial(rv)}{\partial r} + \frac{1}{r}\frac{\partial w}{\partial \theta} + \frac{\partial u}{\partial x} = 0 \tag{C.1}$$

$$\rho\frac{\partial u}{\partial t} + \rho\left(u\frac{\partial u}{\partial x} + v\frac{\partial u}{\partial r} + \frac{w}{r}\frac{\partial u}{\partial \theta}\right) = \rho f_x - \frac{\partial p}{\partial x} + \mu\left(\frac{\partial^2 u}{\partial x^2} + \frac{\partial^2 u}{\partial r^2} + \frac{1}{r}\frac{\partial u}{\partial r} + \frac{1}{r^2}\frac{\partial^2 u}{\partial \theta^2}\right) \tag{C.2}$$

$$\begin{aligned}\rho\frac{\partial v}{\partial t} + \rho\left(u\frac{\partial v}{\partial x} + v\frac{\partial v}{\partial r} + \frac{w}{r}\frac{\partial v}{\partial \theta} - \frac{w^2}{r}\right) = \\ \rho f_r - \frac{\partial p}{\partial r} + \mu\left(\frac{\partial^2 v}{\partial x^2} + \frac{\partial^2 v}{\partial r^2} + \frac{1}{r}\frac{\partial v}{\partial r} + \frac{1}{r^2}\frac{\partial^2 v}{\partial \theta^2} - \frac{v}{r^2} - \frac{2}{r^2}\frac{\partial w}{\partial \theta}\right),\end{aligned} \tag{C.3}$$

where

- u, v, and w are the velocities along the x, r, and θ directions, respectively,
- u, v, and w are functions of x, r, t
- f_x and f_r are the body forces (gravitational forces) in the x and r-directions.
- $\frac{\partial p}{\partial x}$ and $\frac{\partial p}{\partial r}$ are the components of the pressure gradient in the x- and r-directions, respectively.

Assuming:

- No external forces are acting on the pipe ($f_x = 0$ and $f_r = 0$)
- Flow is fully developed i.e., no change of velocity in the axial direction,

  $\frac{\partial u}{\partial x} = 0 \Rightarrow u(r,t)$,
- Flow is axisymmetric i.e., $\frac{\partial u}{\partial \theta} = 0$
- No swirling of flow $(w = 0)$

From the above assumptions, Equation(C.1) which is the continuity equation, becomes

$$\frac{\partial (rv)}{\partial r} = 0 \Rightarrow v = 0 \tag{C.4}$$

Considering the assumptions and Equation (C.4), Equation (C.3) reduces to:

$$-\frac{\partial p}{\partial r} = 0 \tag{C.5}$$

Equation (C.5) shows that pressure is constant across a section of the pipe. Hence, pressure varies only with the x-direction and time.

Considering the above assumptions and equations, Equation (C.2) becomes

$$\frac{\partial u}{\partial t} = -\frac{1}{\rho}\frac{\partial p}{\partial x} + \frac{\mu}{\rho}\left(\frac{\partial^2 u}{\partial r^2} + \frac{1}{r}\frac{\partial u}{\partial r}\right) \tag{C.6}$$

For an unsteady flow, with a periodic pulsatile pressure gradient waveform, the gradient can be expressed as a sum of sine and cosine functions (Fourier series. See Appendix A for more details). Let T be the period of the pressure wave given by $\left(T = \frac{2\pi}{\omega}\right)$.

Then,

$$-\frac{\partial p}{\partial x} = \sum_{n=-M}^{M} \psi_n(x) e^{in\omega t}, \tag{C.7}$$

where $\Psi_n(x) = a_{\Psi n}(x) - ib_{\Psi n}(x)$, $(\text{for } n \geq 0)$

$\psi_n(x)$ is the Fourier coefficient representing the pressure differential across the pipe.

From Equation (C.5), it was determined that pressure differential varies only with the x-direction and time. Hence $\psi_n(x)$ is independent of r but is dependent on x.

For $\frac{\partial p}{\partial x}$ to be real, impose $\psi_{-n}(x) = \overline{\psi_n(x)}$ (See Appendix A for proof)

Since the pressure is periodic, the velocity waveform is also periodic. Hence the solution to Equation (C.6) can be of the form

$$u(r,t) = \sum_{n=-M}^{M} u_n(r) e^{in\omega t} \tag{C.8}$$

where $u_n(r) = a_{vn}(r) - ib_{vn}(r)$, $(\text{for } n \geq 0)$

For $u(r,t)$ to be real, impose $u_{-n}(r) = \overline{u_n(r)}$ (See Appendix A for proof)

Differentiating Equation (C.8) w.r.t r, $\frac{\partial u}{\partial r} = \sum_{n=-M}^{M} \frac{\partial u_n(r)}{\partial r} e^{in\omega t}$ (C.9)

Differentiating Equation (C.9) w.r.t r, $\frac{\partial^2 u}{\partial r^2} = \sum_{n=-M}^{M} \frac{\partial^2 u_n(r)}{\partial r^2} e^{in\omega t}$ (C.10)

From Equation (C.8), $\frac{\partial u}{\partial t} = \sum_{n=-M}^{M} u_n(r) in\omega e^{in\omega t}$ (C.11)

Substituting Equations (C.7), (C.9), (C.10) and (C.11) in Equation (C.6) which is:

$$\frac{\partial u}{\partial t} = -\frac{1}{\rho}\frac{\partial p}{\partial x} + \frac{\mu}{\rho}\left(\frac{\partial^2 u}{\partial r^2} + \frac{1}{r}\frac{\partial u}{\partial r}\right), \text{ leads to}$$

$$\sum_{n=-M}^{M} u_n(r)\, in\omega e^{in\omega t} = \begin{cases} \frac{1}{\rho}\sum_{n=-M}^{M} \psi_n(x) e^{in\omega t} + \frac{\mu}{\rho}\sum_{n=-M}^{M} \frac{\partial^2 u_n(r)}{\partial r^2} e^{in\omega t} + \\ + \frac{\mu}{r\rho}\sum_{n=-M}^{M} \frac{\partial u_n(r)}{\partial r} e^{in\omega t} \end{cases}$$

If $\nu = \frac{\mu}{\rho}$, then the above equation becomes

$$\sum_{n=-M}^{M} u_n(r)\, in\omega e^{in\omega t} = \begin{cases} \frac{1}{\rho}\sum_{n=-M}^{M} \psi_n(x) e^{in\omega t} + \nu\sum_{n=-M}^{M} \frac{\partial^2 u_n(r)}{\partial r^2} e^{in\omega t} + \\ + \frac{\nu}{r}\sum_{n=-M}^{M} \frac{\partial u_n(r)}{\partial r} e^{in\omega t} \end{cases}$$

Comparing Fourier coefficients corresponding to $e^{in\omega t}$, leads to

$$u_n(r)\, in\omega = \frac{\psi_n(x)}{\rho} + \nu\frac{\partial^2 u_n(r)}{\partial r^2} + \frac{\nu}{r}\frac{\partial u_n(r)}{\partial r}$$

$$\frac{\partial^2 u_n(r)}{\partial r^2} + \frac{1}{r}\frac{\partial u_n(r)}{\partial r} - \frac{in\omega}{\nu} u_n(r) + \frac{\psi_n(x)}{\mu} = 0 \qquad \text{(C.12)}$$

When n = 0, Equation (C.12) becomes

$$\frac{\partial^2 u_0(r)}{\partial r^2} + \frac{1}{r}\frac{\partial u_0(r)}{\partial r} + \frac{\psi_0}{\mu} = 0 \qquad \text{(C.13)}$$

Equation (C.13) is the classic Poiseuille flow equation.

Solving Equation (C.13) which is,

$$\frac{1}{r}\frac{\partial}{\partial r}\left(r\frac{\partial u_0(r)}{\partial r}\right)+\frac{\psi_0}{\mu}=0$$

$$\frac{\partial}{\partial r}\left(r\frac{\partial u_0(r)}{\partial r}\right)=-\frac{\psi_0}{\mu}r$$

Integrating w.r.t r gives

$$\left(r\frac{\partial u_0(r)}{\partial r}\right)=-\frac{\psi_0}{\mu}\frac{r^2}{2}+\mathrm{K}_1$$

$$\frac{\partial u_0(r)}{\partial r}=-\frac{\psi_0}{\mu}\frac{r}{2}+\frac{K_1}{r}$$

Integrating again w.r.t r leads to

$$u_0(r)=-\frac{\psi_0}{4\mu}r^2+K_1\ln r+K_2, \qquad \text{(C.14)}$$

where K_1 and K_2 are constants.

When $n\neq 0$, from Equation (C.12)

$$\frac{\partial^2 u_n(r)}{\partial r^2}+\frac{1}{r}\frac{\partial u_n(r)}{\partial r}-\frac{in\omega}{\nu}u_n(r)+\frac{\psi_n(x)}{\mu}=0$$

$$\frac{\partial^2 u_n(r)}{\partial r^2}+\frac{1}{r}\frac{\partial u_n(r)}{\partial r}+\frac{i^3 n\omega}{\nu}u_n(r)=-\frac{\psi_n(x)}{\mu} \qquad \text{(C.15)}$$

Considering the homogenous part of the above equation,

$$\frac{\partial^2 u_n(r)}{\partial r^2}+\frac{1}{r}\frac{\partial u_n(r)}{\partial r}+\frac{i^3 n\omega}{\nu}u_n(r)=0$$

$$r^2\frac{\partial^2 u_n(r)}{\partial r^2}+r\frac{\partial u_n(r)}{\partial r}+\frac{i^3 n\omega}{\nu}r^2 u_n(r)=0$$

$$r^2\frac{\partial^2 u_n(r)}{\partial r^2}+r\frac{\partial u_n(r)}{\partial r}+(\lambda_n r)^2 u_n(r)=0, \tag{C.16}$$

where $\lambda_n \in \mathbb{C}$ such that $\lambda_n^2=\frac{i^3 n\omega}{\nu}$

Equation (C.16) is similar to a Bessel equation of order zero.

Bessel equation of order γ is given by $x^2\frac{d^2y}{dx^2}+x\frac{dy}{dx}+(x^2-\gamma^2)y=0$. The solution of this equation is given by $y(x)=K_3J_\gamma(x)+K_4Y_\gamma(x)$. The solution of Equation (C.16) which is $u_n(r)\big|_h=K_3J_0(\lambda_n r)+K_4Y_0(\lambda_n r),$ is obtained by comparing Equation (C.16) with the Bessel equation. K_3 and K_4 are constants and $u_n(r)\big|_h$ denotes the homogenous solution of the equation.

Let the particular solution of Equation (C.15) be a constant, K_5. Substituting this in Equation (C.15) gives

$$\frac{i^3 n\omega}{\nu}K_5=-\frac{\psi_n(x)}{\mu}$$

$$K_5=-\frac{\psi_n(x)}{i^3 n\omega\rho}$$

The complete solution of Equation (C.15) is obtained by combining the homogenous and the particular solution and it is given by

$$u_n(r)=K_3J_0(\lambda_n r)+K_4Y_0(\lambda_n r)-\frac{\psi_n(x)}{i^3 n\omega\rho} \tag{C.17}$$

Combining Equations (C.14) and particular solution, K, the expression for $u_n(r) \forall n$ is given by

$$u_n(r) = -\frac{\psi_0(x)}{4\mu} r^2 + K_1 \ln r + K_2 + K_3 J_0(\lambda_n r) + K_4 Y_0(\lambda_n r) - \frac{\psi_n(x)}{i^3 n\omega\rho} \tag{C.18}$$

Equation (C.8) can also be written as

$$u(r,t) = \sum_{n=-M}^{M} u_n(r) e^{in\omega t} = u_0(r) + \sum_{\substack{n=-M \\ n\neq 0}}^{M} u_n(r) e^{in\omega t}$$

Substituting Equations (C.14) and (C.17) in the above equation gives

$$u(r,t) = -\frac{\psi_0}{4\mu} r^2 + K_1 \ln r + K_2 + \sum_{\substack{n=-M \\ n\neq 0}}^{M} \left(K_3 J_0(\lambda_n r) + K_4 Y_0(\lambda_n r) - \frac{\psi_n(x)}{i^3 n\omega\rho} \right) e^{in\omega t},$$

where K_1, K_2, K_3 and K_4 are constants determined by the boundary conditions. One such boundary condition is that the velocity at the centerline must be finite:

$$u(r) < \infty \quad \Rightarrow \quad \begin{cases} K_1 = 0 \text{ because } \lim_{r\to 0} \ln(r) \to \infty \\ K_4 = 0 \text{ because } \lim_{r\to 0} Y_o(\lambda_n r) \to \infty \end{cases}$$

Hence $u(r,t) = -\frac{\psi_0}{4\mu} r^2 + K_2 + \sum_{\substack{n=-M \\ n\neq 0}}^{M} \left(K_3 J_0(\lambda_n r) - \frac{\psi_n(x)}{i^3 n\omega\rho} \right) e^{in\omega t}$ (C.19)

The boundary condition at the wall, $(r = R)$ known as the no-slip condition requires that the velocity be zero. When r = R, Equation (C.19) becomes

$$u(r = R, t) = 0 = -\frac{\psi_0}{4\mu} R^2 + K_2 + \sum_{\substack{n=-M \\ n\neq 0}}^{M} \left(K_3 J_0(\lambda_n R) - \frac{\psi_n(x)}{i^3 n\omega\rho} \right) e^{in\omega t}$$

Comparing constant terms and coefficients of $e^{in\omega t}$ gives

$$-\frac{\psi_0}{4\mu}R^2 + K_2 = 0 \text{ and } K_3 J_0(\lambda_n R) - \frac{\psi_n(x)}{i^3 n\omega\rho} = 0$$

Hence $K_2 = \frac{\psi_0}{4\mu}R^2$ and $K_3 = \frac{\psi_n(x)}{i^3 n\omega\rho}\frac{1}{J_0(\lambda_n R)}$

Substituting K_2 and K_3 into Equation (C.19) obtains

$$u(r,t) = -\frac{\psi_0}{4\mu}r^2 + \frac{\psi_0(x)}{4\mu}R^2 + \sum_{\substack{n=-M \\ n\neq 0}}^{M}\left(\frac{\psi_n(x)}{i^3 n\omega\rho}\frac{J_0(\lambda_n r)}{J_0(\lambda_n R)} - \frac{\psi_n(x)}{i^3 n\omega\rho}\right)e^{in\omega t}$$

$$u(r,t) = \frac{\psi_0}{4\mu}R^2\left(1-\frac{r^2}{R^2}\right) + \sum_{\substack{n=-M \\ n\neq 0}}^{M} -\frac{\psi_n(x)}{i^3 n\omega\rho}\left(1-\frac{J_0(\lambda_n r)}{J_0(\lambda_n R)}\right)e^{in\omega t}$$

$$u(r,t) = \frac{\psi_0}{4\mu}R^2(1-h^2) + \sum_{\substack{n=-M \\ n\neq 0}}^{M}\frac{\psi_n(x)}{in\omega\rho}\left(1-\frac{J_0(\lambda_n r)}{J_0(\lambda_n R)}\right)e^{in\omega t}, \qquad \text{(C.20)}$$

where

$$h = r/R$$

$$\psi_n(x) = a_{\psi n}(x) - ib_{\psi n}(x)$$

$$\lambda_n^2 = \frac{i^3 n\omega}{\nu}$$

For simplicity, let $\alpha_n = R\sqrt{\frac{n\omega}{\nu}} \Rightarrow \lambda^2 = i^3\frac{\alpha_n^2}{R^2}$

Suppose that the flow rate, Q, is given in terms of Fourier series, then

$$Q(r,t)=\sum_{n=-M}^{M} q_n(r)e^{in\omega t}, \tag{C.21}$$

where $q_n(r)=a_{qn}(r)-ib_{qn}(r)$, $(\text{for } n\geq 0)$

For $Q(r,t)$ to be real, impose $q_{-n}(r)=\overline{q_n(r)}$ (See Appendix A for proof)

By definition,

$$Q(r,t)=\int_0^R u(r,t)\,2\pi r\,dr$$

$$Q(r,t)=\int_0^R\left(\frac{\psi_0}{4\mu}R^2\left(1-h^2\right)+\sum_{\substack{n=-M\\ n\neq 0}}^{M}\frac{\psi_n(x)}{in\omega\rho}\left(1-\frac{J_0(\lambda_n r)}{J_0(\lambda_n R)}\right)e^{in\omega t}\right)2\pi r\,dr$$

$$=\int_0^R\frac{\psi_0}{4\mu}\left(R^2-r^2\right)2\pi r\,dr+\sum_{\substack{n=-M\\ n\neq 0}}^{M}\frac{\psi_n(x)}{in\omega\rho}\left(1-\frac{J_0(\lambda_n r)}{J_0(\lambda_n R)}\right)e^{in\omega t}\,2\pi r\,dr$$

$$=\frac{\psi_0}{4\mu}\left(R^2\pi r^2-\frac{\pi r^4}{2}\right)\Bigg|_0^R+\sum_{\substack{n=-M\\ n\neq 0}}^{M}\frac{\psi_n(x)}{in\omega\rho}e^{in\omega t}\int_0^R\left(1-\frac{J_0(\lambda_n r)}{J_0(\lambda_n R)}\right)2\pi r\,dr$$

$$=\frac{\psi_0}{4\mu}\left(R^4\pi-\frac{\pi R^4}{2}\right)+\sum_{\substack{n=-M\\ n\neq 0}}^{M}\frac{\psi_n(x)}{in\omega\rho}e^{in\omega t}\int_0^R\left(1-\frac{J_0(\lambda_n r)}{J_0(\lambda_n R)}\right)2\pi r\,dr$$

From properties of Bessel functions

$$\int rJ_0(r)\,dr=rJ_1(r)\quad and\quad J_1(0)=0$$

$$\int rJ_0(\lambda r)\,dr=\frac{rJ_1(\lambda r)}{\lambda}$$

Hence $Q(r,t) = \frac{\psi_0}{4\mu}\left(\frac{\pi R^4}{2}\right) + \sum_{\substack{n=-M \\ n\neq 0}}^{M} \frac{\psi_n(x)}{in\omega\rho} e^{in\omega t}\left(\pi r^2 - \frac{2\pi}{J_0(\lambda_n R)}\frac{rJ_1(\lambda_n r)}{\lambda_n}\right)\Bigg|_0^R$

$= \frac{\psi_0}{4\mu}\left(\frac{\pi R^4}{2}\right) + \sum_{\substack{n=-M \\ n\neq 0}}^{M} \frac{\psi_n(x)}{in\omega\rho} e^{in\omega t}\left(\pi R^2 - \frac{2\pi}{J_0(\lambda_n R)}\frac{RJ_1(\lambda_n R)}{\lambda_n}\right)$

$= \frac{\psi_0}{4\mu}\left(\frac{\pi R^4}{2}\right) + \sum_{\substack{n=-M \\ n\neq 0}}^{M} \frac{\psi_n(x)}{in\omega\rho} e^{in\omega t}\pi R^2\left(1 - \frac{2J_1(\lambda_n R)}{R\lambda_n J_0(\lambda_n R)}\right)$

But, from Fourier series expansion, $Q(r,t) = \sum_{n=-M}^{M} q_n(r) e^{in\omega t}$

Hence $Q(r,t) = \sum_{n=-M}^{M} q_n(r) e^{in\omega t} = \frac{\psi_0}{4\mu}\left(\frac{\pi R^4}{2}\right) + \sum_{\substack{n=-M \\ n\neq 0}}^{M} \frac{\psi_n(x)}{in\omega\rho} e^{in\omega t}\pi R^2\left(1 - \frac{2J_1(\lambda_n R)}{R\lambda_n J_0(\lambda_n R)}\right)$

Comparing constants and coefficients of $e^{in\omega t}$ leads to

$Q(r,t) = q_0 + \sum_{\substack{n=-M \\ n\neq 0}}^{M} q_n(r) e^{in\omega t} = \frac{\psi_0}{4\mu}\left(\frac{\pi R^4}{2}\right) + \sum_{\substack{n=-M \\ n\neq 0}}^{M} \frac{\psi_n(x)}{in\omega\rho} e^{in\omega t}\pi R^2\left(1 - \frac{2J_1(\lambda_n R)}{R\lambda_n J_0(\lambda_n R)}\right)$

$q_0 = \frac{\psi_0}{8\mu}\pi R^4$ and $q_n(r) = \frac{\psi_n(x)}{in\omega\rho}\pi R^2\left(1 - \frac{2J_1(\lambda_n R)}{R\lambda_n J_0(\lambda_n R)}\right)$

Hence

$\psi_0 = \frac{8\mu q_0}{\pi R^4}$ and $\psi_n(x) = \frac{q_n(r)}{\pi R^2}\frac{in\omega\rho}{\left(1 - \frac{2J_1(\lambda_n R)}{R\lambda_n J_0(\lambda_n R)}\right)}$

Using these expressions in Equation (C.20), which is

$u(r,t) = \frac{\psi_0}{4\mu}R^2\left(1-h^2\right) + \sum_{\substack{n=-M \\ n\neq 0}}^{M} \frac{\psi_n(x)}{in\omega\rho}\left(1 - \frac{J_0(\lambda_n r)}{J_0(\lambda_n R)}\right)e^{in\omega t}$,

results in

$$u(r,t)=\frac{2q_0}{\pi R^2}\left(1-h^2\right)+\sum_{\substack{n=-M\\ n\neq 0}}^{M}\left[\frac{q_n(r)}{\pi R^2}\frac{\left(1-\dfrac{J_0(\lambda_n r)}{J_0(\lambda_n R)}\right)}{\left(1-\dfrac{2J_1(\lambda_n R)}{R\lambda_n J_0(\lambda_n R)}\right)}\right]e^{in\omega t}, \qquad \text{(C.22)}$$

where $q_n(r)=a_{qn}(r)-ib_{qn}(r)$ and $\overline{q_n(r)}=a_{qn}(r)+ib_{qn}(r)$.

Equation (C.22) can be re-written as $u(r,t)=\frac{2q_0}{\pi R^2}\left(1-h^2\right)+\sum_{\substack{n=-M\\ n\neq 0}}^{M}U_n(r)e^{in\omega t}$, (C.23)

where $U_n(r)=\frac{q_n(r)}{\pi R^2}\frac{\left(1-\dfrac{J_0(\lambda_n r)}{J_0(\lambda_n R)}\right)}{\left(1-\dfrac{2J_1(\lambda_n R)}{R\lambda_n J_0(\lambda_n R)}\right)}$

Hence from Equations (C.8) and (C.23),

$$u(r,t)=\sum_{n=-M}^{M}u_n(r)e^{in\omega t}=\frac{2q_0}{\pi R^2}\left(1-h^2\right)+\sum_{\substack{n=-M\\ n\neq 0}}^{M}U_n(r)e^{in\omega t}$$

For $u(r,t)$ to be real, it was imposed that $u_{-n}(r)=\overline{u_n(r)}$. This will be the case if $U_{-n}(r)=\overline{U_n(r)}$. For this to be true, the following conditions are to be satisfied:

i. $q_{-n}(r)=\overline{q_n(r)}$,

ii. $\overline{J_0(\lambda_n r)}=J_0(\lambda_{-n}r)$, $\overline{J_1(\lambda_n r)}=J_1(\lambda_{-n}r)$ and $\overline{\lambda_n J_0(\lambda_n R)}=\lambda_{-n}J_0(\lambda_{-n}R)$.

For $Q(r,t)$ to be real, it was imposed that $q_{-n}(r)=\overline{q_n(r)}$. Note that

$J_\alpha(z)=\sum_{m=0}^{\infty}\frac{(-1)^m}{m!\Gamma(m+\alpha+1)}\left(\frac{z}{2}\right)^{2m+\alpha}$. Hence, J_0 and J_1 have real power series in powers

of their arguments. Also, both $J_0(\lambda_n r)$ and $\lambda_n J_1(\lambda_n R)$ have series expansions in even powers of $\lambda_n r$ *and* $\lambda_n R$, respectively. Hence $\overline{J_0(\lambda_n r)} = J_0\left(\overline{\lambda_n} r\right)$ and $\overline{J_1(\lambda_n r)} = J_1\left(\overline{\lambda_n} r\right)$.

Therefore, for (ii) to be true, it is sufficient to show that $\left(\overline{\lambda_n}\right)^2 = \left(\lambda_{-n}\right)^2$.

From the definition of $\lambda_n{}^2$,

$$\lambda_n{}^2 = \frac{i^3 n\omega}{\nu} = \frac{n\omega}{\nu}\exp\left(\frac{3}{2}\pi i\right)$$

Hence

$$\left(\overline{\lambda_n}\right)^2 = \frac{n\omega}{\nu}\exp\left(\frac{-3}{2}\pi i\right) = \frac{in\omega}{\nu} = \frac{i^3(-n)\omega}{\nu} = \left(\lambda_{-n}\right)^2.$$

Since both the conditions (i) and (ii) are satisfied, $U_{-n}(r) = \overline{U_n(r)}$ and $u(r,t)$ given by Equation (C.23) is real.

Hence, Equation (C.23) becomes,

$$u(r,t) = \frac{2q_0}{\pi R^2}\left(1-h^2\right) + 2\,\mathrm{Re}\left[\sum_{n=1}^{M} U_n(r) e^{in\omega t}\right], \tag{C.24}$$

where $U_n(r) = \dfrac{q_n(r)}{\pi R^2} \dfrac{\left(1 - \dfrac{J_0(\lambda_n r)}{J_0(\lambda_n R)}\right)}{\left(1 - \dfrac{2J_1(\lambda_n R)}{R\lambda_n J_0(\lambda_n R)}\right)}$

Assume $U_n(r) = A_{vn}(r) - iB_{vn}(r)$ $(\text{for } n \geq 0)$. Then,

$$U_n(r) = \frac{q_n(r)}{\pi R^2} \frac{\left(1 - \dfrac{J_0(\lambda_n r)}{J_0(\lambda_n R)}\right)}{\left(1 - \dfrac{2J_1(\lambda_n R)}{R\lambda_n J_0(\lambda_n R)}\right)} = A_{vn}(r) - iB_{vn}(r)$$

Substituting above expression in Equation (C.24) leads to

$$u(r,t)=\frac{2q_0}{\pi R^2}\left(1-h^2\right)+2\,\mathrm{Re}\left[\sum_{n=1}^{M}\left(A_{vn}(r)-iB_{vn}(r)\right)e^{in\omega t}\right]\text{(See Appendix A for proof)}$$

$$=\frac{2q_0}{\pi R^2}\left(1-h^2\right)+2\sum_{n=1}^{M}A_{vn}(r)\cos(n\omega t)+B_{vn}(r)\sin(n\omega t),$$

where

$$A_{vn}(r)=\mathrm{Re}\left[\frac{q_n}{\pi R^2}\frac{\left(1-\frac{J_0(\lambda_n r)}{J_0(\lambda_n R)}\right)}{\left(1-\frac{2J_1(\lambda_n R)}{R\lambda_n J_0(\lambda_n R)}\right)}\right],\quad B_{vn}(r)=-\mathrm{Imag}\left[\frac{q_n(r)}{\pi R^2}\frac{\left(1-\frac{J_0(\lambda_n r)}{J_0(\lambda_n R)}\right)}{\left(1-\frac{2J_1(\lambda_n R)}{R\lambda_n J_0(\lambda_n R)}\right)}\right],$$

$h=r/R,$

and $\lambda_n^2=\dfrac{i^3n\omega}{\nu}$

Note that:

i α is known as the Womersley number and is given by $\alpha=R\sqrt{\dfrac{\omega}{\nu}}$

ii For low frequencies, $\omega=0\Rightarrow\alpha=0$ .Also, when $n=0\Rightarrow\alpha=0$. Hence for low frequencies, the solution to Equation (C.12) is given by Equation (C.14). After using the boundary conditions to evaluate the constants, this equation reduces to $u_0(r)=\dfrac{\psi_0(x)}{4\mu}R^2\left(1-q^2\right),$ which is a parabola. Hence, the pipe flow problem with a pulsatile pressure waveform behaves as a pipe flow with steady flow (i.e., Poiseuille flow problem) for low frequencies.